THE STUDY OF ULTRA-FAST RELAXATION PHENOMENA WITHIN ND:YAG AND HOPG CRYSTALS.

A Dissertation

Presented to the Faculty of the Graduate School

of Cornell University

in Partial Fulfillment of the Requirements for the Degree of

Doctor of Philosophy

by

Bryant T. Wysocki

May 2011

THE STUDY OF ULTRA-FAST RELAXATION PHENOMENA WITHIN ND:YAG AND HOPG CRYSTALS.

Bryant T. Wysocki, Ph.D.

Cornell University 2011

A monolithic two-section quantum dot semiconductor laser is differentially pumped to form non-uniform current injection in the gain region. It is shown that the nature of the pulse spectral content can be manipulated through differential gain. This provided a simple and inexpensive method of optimizing the semiconductor laser performance and also demonstrated that mode locked operation can be achieved with a much larger set of injection current/absorber bias voltage pairs than was previously possible with single-pad current injection. Significantly greater absorber bias voltages were available during differential pumping; thereby reducing absorber recovery time as well as the inferred pulse length. The enhanced spectral bandwidth provided by differential pumping provided an electronic method of pulse length reduction. The capacity for wavelength tuning was also demonstrated by differential pumping with a center wavelength shift of approximately 12nm. Additionally, the design and configuration of a femtosecond IR optical parametric oscillator demonstrating continuous pulsed tunability from 1040 to 1150 nm is presented along with the examination of relaxation rates for optically excited electrons from the pumping level ($^4F\frac{5}{2}$) to the metastable upper lasing level ($^4F\frac{3}{2}$) in neodymium doped Yttrium aluminum garnet (Nd:YAG) laser crystals. The $^4F\frac{5}{2}$ lifetime was theoretically predicted to be approximately 12 picoseconds using the Energy Gap Law. Finally, the ultrafast relaxations of photoexcited carriers in thin films of

exfoliated highly ordered pyrolytic graphite (HOPG) were examined using the equal-pulse correlation technique which provides the means to efficiently extract a relatively fast relaxation process obscured by a significantly slower one. In addition, it allows for measurements on the order of one tenth the laser pulse width, extending the temporal range of existing pump probe systems without the need for customized femtosecond lasers or complicated pulse compression systems. The HOPG samples exhibited an extremely fast relaxation due to intraband carrier-carrier thermalization observed at 15 ± 10 fs followed by intraband carrier-phonon interaction on the order of 175 ± 30 fs. A modulation in the absorption depth of 1.4 percent was observed in the samples from partial saturation due to Pauli blocking.

BIOGRAPHICAL SKETCH

Bryant Wysocki was born in a small town in Pennsylvania where he developed a curiosity for the world around him. He never got over his inquisitive nature and found himself as a PhD student at Cornell University many years later. He plans to spend the rest of his days enjoying life, family and friends, and the fascinating ways of the universe.

I dedicate this dissertation to my loving family; April, Skyler, Summer, and Rowan, and to my parents; Stanely and Margaret, and finally to all the graduate students at Cornell University, past, present, and future.

ACKNOWLEDGEMENTS

First and foremost, I give thanks to the Lord; through him all things are possible.

It has been an honor and a pleasure working with Professor Clif Pollock as my advisor and mentor during my time at Cornell and I wish to extend my deepest thanks for his skilled guidance and constant encouragement. His flexibility to accommodate my lengthy commute and unpredictable work schedule at the Air Force Research Laboratory is a testament to his dedication. He is truly a legend and cowboy experimentalist extraordinaire. I thank Professor Michal Lipson for serving on my thesis committee and for her powerful enthusiasm for learning and her dedication in the classroom. I owe a great deal of thanks to Professor Frank Wayno as my minor advisor for his incredibly insightful and enjoyable instruction and for exposing me to the leadership traits that make individuals of his caliber so influential. I cannot imagine a thesis committee more capable, supportive, or dedicated as they.

I send thanks to Dr. Michael Marciniak of the Air Force Institute of Technology for his support during my masters thesis and for introducing me to the excitement of experimental research. His confidence in my abilities fueled my desire to pursue a lifestyle of continued education. I am grateful to all my colleagues and friends at the Air Force Research Laboratory who consistently guide and support my efforts. Dr. Michael Hayduk cannot be thanked enough since he is the man that suggested studying at Cornell and the one who helped make it happen. He is a true friend that has earned my highest respect and admiration. I have been fortunate to learn from outstanding scientist like Dr. Joseph Van Nostrand, Dr. Robinson Pino, Dr. Joseph Osman, Dr. Reinhard Erdmann, Michael Fanto, John Malowicki, and with special thanks; Thomas

McEwen, who is a mentor, confidant, and friend. The nearly constant discussions of theoretical and experimental physics in the lab and at the whiteboard were invaluable and one hell of a good time, especially with the occasional wine, cheese, and single malt scotch.

I am privileged to have worked with Bryan Hicks and Victor Bucklew, two outstanding colleagues and fellow graduate students. They transformed my previously solitary nights in the lab into a most rewarding experience. There is no substitute for the education received while working with friends of such ability and character. I simply could not have survived without them, plus they are ok guys.

This would not have been possible without the undiminished support and encouragement from my family. I thank my wife April for her patience and understanding as she absorbed my responsibilities in addition to her already unfair share, as I spent countless nights away from home. She is the most giving and selfless person I have ever known. I thank my children, Skyler, Summer, and Rowan for just being awesome and bringing a depth to my life that only they could bestow. I am also grateful to my parents, Stanley and Margaret who gave me the freedom to find my own road and the discipline to follow it.

I am grateful to the Air Force Research Laboratory for fellowship support and a culture that fosters education and growth.

TABLE OF CONTENTS

LIST OF TABLES

LIST OF FIGURES

CHAPTER 1

INTRODUCTION

1.1 The Field of Ultrafast Optics

The temporal measurement of any event requires that it be compared to some shorter event or action in time. Thus two capabilities are required to describe the duration of an event: the generation of a shorter or equal temporal occurrence and a method of comparing the two. When probing events at the molecular and atomic scales truly fast phenomenons are necessary to act as the temporal rulers with durations ranging from 10^{-6} to less than 10^{-15} seconds. Today the generation of 80 femtosecond (1fs = $1x10^{-15}$ s) optical pulses is common in the laboratory. Sytems designed to generate, utilize, and measure such short occurences fall into the field of Ultrafast Optics.

The field of ultrafast optics has reached such a high level of maturity that all branches of science now have access to ultrafast optical systems, and the need for reliable and easy to operate commercial products has fueled an industry. Ultrafast optical technologies continue to mature and they will continue to drive innovations in research while growing their influence in industrial markets, further adding to the demand for such products. Thus from a fledgling science in the mid 1960's, ultrafast optics has quickly developed into a mature field with far reaching impacts.

The first real workhorse of the field was the dye laser, initially demonstrated in 1966 [1] and continually refined over the next 25 years. Dye lasers were eventually cable of generating pulses from a few ps down to tens of fs. The most successful being rhodamine dye lasers, which have produced pulses as short as 27

fs at 630 nm with average powers of 10 mW [2], and have reached durations as short as 6 fs with external compression [3]. But the dyes suffer from degradation during operation and are carcinogenic, making them difficult to handle. The development of the Titanium sapphire (Ti:sapphire, Ti:Al_2O_3) laser brought increased stability, reliability, and ease of use to the field and thus quickly moved to the forefront as the new standard in tunable pulsed lasers. The Ti:sapphire laser was first demonstrated in 1982 [4] and was available in commercial models by the late 1980s. With a bandwidth extending from 650-1100 nm, the Ti:sapphire laser holds the record for the shortest directly produced pulses, being measured at 5 fs [5], which are only two optical cycles. In addition, pulses as short as 3.8 fs have been produced using external compression techniques [6]. Similar to the once dominate dye lasers, Ti sapphire remains unsurpassed as the modern workhorse of ultrafast optics. Of course, other well established solid state gain mediums have been developed, which have extended the spectral regions of available pulsed sources, such as chromium forsterite (Cr4+:Mg_2SiO_4) and chromium doped yttrium aluminum garnet Cr:YAG (Cr4+:$Y_3Al_5O_{12}$). The optical properties of Ti:sapphire along with the other notable lasers are summarized in Table 1.1.

Nonlinear optical processes expanded the reach of these pulsed laser systems to wavelength regions outside their bandwidth. The laser itself provided the means to generate previously unattainable optical intensities which led to the field of nonlinear optics that began in the early 1960s. Second harmonic generation was demonstrated in 1961 [9] and expanded the useful wavelength range of lasing mediums. It was not long until other nonlinear effects were demonstrated to include sum and difference frequency generation [10], third harmonic generation [11], and optical parametric amplification [12, 13].

Laser	$\Delta\lambda$ (nm)	τ (μs)	σ (cm^2)	τ_{pulse} (fs)	n
Ti:Sapphire	700-1100	3.2	4.90 x 10^{-20}	5, [5]	1.76
Cr:Forsterite	1130-1348	3.0	4.45 x 10^{-19}	14, [7]	1.67
Cr:YAG	1350-1650	3.4	2.82 x 10^{-19}	20, [8]	1.82

Table 1.1: Typical optical properties of three popular solid state laser gain mediums used in ultrashort pulse generation. Tuning range ($\Delta\lambda$), Lifetime (τ), Emission cross section (σ), Pulse Width (τ_{pulse}), and index of refraction (n) at the most common wavelength.

Today, nonlinear processes play a growing role in modern optical systems. Optical parametric oscillators produce femtosecond pulses through second order parametric down conversion in wavelength ranges outside of conventionally achieved laser bands that extend into the near, mid, and far infrared regions. Commercial models are now available that are continuously tunable from 1.1 to 2.5 microns, have output powers greater than 200 mW, and are computer controlled, making the technology accessible to researchers without optical backgrounds. With applications in semiconductor research, optical communications development, time resolved spectroscopy, and pump probe experimentation, optical parametric oscillators are becoming more prevalent in chemical, biological, and physical research institutions.

The tools and techniques used to measure ultrashort pulses and physical phenomenon have progressed concurrently with the development of the laser. As laser pulses became the shortest temporal events ever generated by man, scientists had to devise a way to measure them. This task turns out to be a difficult problem, so that the ability to accurately measure the pulses tends to lag behind our ability to generate them. Knowledge of a pulse's spectrum, in-

tensity, and phase are needed to completely describe a pulse and increasingly precise techniques have been developed to measure these pulse characteristics. The best electronic optical detectors can measure pulses with an accuracy of nearly one picosecond, but this falls far short of being a viable method for many applications. Since the pulses can't be directly measured, and there is nothing shorter on which to compare, the pulses are often gauged against themselves. The intensity autocorrelation compares an optical pulse with itself to determine the rms pulsewidth through the use of intensity dependent nonlinear interactions, but provides no information on either the spectral content or the phase. This lack of phase data results in ambiguities of the pulse measurement which has pressured the development of more sophisticated methods such as frequency resolved optical gating (FROG) [14, 15, 16], spectral interferometry (SI) [17, 18, 19], spectral phase interferometry for direct electric-field reconstruction (SPIDER) [20], and grating-eliminated no-nonsense observation of ultrafast incident laser light e-fields (GRENOUILLE) [21, 15]. Accurate characterization of optical pulses is important for time resolved optical measurements (pump-probe), optimization of laser systems, and to the understanding of ultrashort phenomenon, where many of these techniques have been employed for systems that measure physical events in nature on molecular and atomic time scales.

Many common technical issues that were addressed in the early years of the field remain at the forefront of research today, such as gain medium bandwidth, dispersion compensation, thermal management, and ultrafast measurement techniques. As new technologies are developed that reduce pulse widths, increase power, and expand the available wavelength range, new and exciting opportunities will emerge for applications of these capabilities. There is little doubt that ultrafast optical systems will continue to play an increasingly impor-

tant role in research, industry, and commercial applications.

1.2 The Scope of this Dissertaion

The task of utilizing ultrafast optical techniques to generate mode-locked laser pulses and to investigate the physical properties of materials for use in laser systems is explored in this dissertation. Specifically, we investigate the effects of differential pumping on model-locked laser performance and the use of time resolved pump probe experimentation to measure relaxation times in optically excited media. The research outlined in this work can be broken down into three main sections. The first examines the effects of differential pumping of a monolithic quantum dot laser on the mode-locking stability and spectral content. The second attempts to measure the multiphonon relaxation of photoexcited electrons between the ${}^4F_2^5$ and the ${}^4F_2^3$ manifold levels in Nd:YAG while the third examines the ultrafast carrier dynamics in thin films of exfoliated highly ordered pyrolytic graphite.

1.2.1 Overview of Quantum Dot Laser Testing

A unique recently developed quantum-dot (QD) laser that offers reconfigurable current injection profiles was used to test the effects of differential pumping (nonuniform injection current) on mode-locked laser performance. The monolithic two-section QD laser operating near 1245 nm was subjected to a wide range of pumping scenarios while monitoring the mode-locked stability and spectral content.

The lasers tested are all based on dots-in-a-well (DWELLTM) technology originally developed by the Center for High Technology Materials (CHTM) at UNM. The $In_xGa_{1-x}As$ QD lasers have two sections; an electrically isolated saturable absorber fitted with one electrode accepting 0-6.5 V reverse bias, and a gain section with four current injection pads each allowing 0-450 mA of pumping. The 8.6 mm devices had a pulse repetition rate of 5 GHz when in mode-locked operation.

The lasers are evaluated over a large range of injector currents passed through individual pads and multiple pad combinations. The experiment is controlled through a LabView script and run under multiple absorber bias voltages. Laser performance was appraised by monitoring the output spectrum, power, and mode-locking quality.

The results show that regions of mode-locked operation with respect to injection current and absorber bias have a strong dependence on the location of the injected current within the gain medium and on the differential pumping scheme implemented. Maximum output power was increased through careful control of pumping and ranged between 14-25 mW, while the reverse bias voltage was held constant at 5V. The capacity for wavelength tuning was also demonstrated by differential pumping with a center wavelength shift of approximately 12nm.

1.2.2 Overview of pump probe measurements on Nd:YAG

One of the initial goals of this effort was to establish a tunable femtosecond, dual wavelength, time resolved spectroscopy capability in the lab. The system consists of a pump laser, a frequency stabilized femtosecond infrared OPO, a

pulse selection system, and data acquisition components. The second section of this dissertation looks at pump probe system design and examines our attempt to measure the nonradiative relaxation rate of optically excited electrons from the pumping level ($^4F_2^5$) to the metastable upper lasing level ($^4F_2^3$) in neodymium doped Yttrium aluminum garnet (Nd:YAG) laser crystals.

The premise of the technique was based on optically exciting electrons into the pump manifold and measuring the time it takes for them to relax to the top of the lasing level. Optical gain was the mechanism we employed to monitor when the excited states had decayed and reached the metastable level. This was done by probing the sample with optical pulses of photon energies equal to the lasing energy. As the excited electrons decay, they become available to the probe pulses as signal gain. An optical delay line was used to slowly increment the arrival time of the probe relative to the pump as the probe energy was monitored for gain. The decay time can then be retrieved from the recorded gain verses delay data. Variable lengths of Nd:YAG rods ranging from 1 to 6 mm were cut and polished as test samples, each with a Nd^{3+} ion density at 1 %. An 80 fs Titanium Sapphire laser served to pump the samples and as the source for a femtosecond optical parametric oscillator (OPO) [22, 23] that supplied the probe pulses.

The OPO typically produced pulse durations near 100 fs and was continuously tunable over a range of 1050 to 1150 nm. The synchronously pumped ring configured OPO utilized a periodically polled lithium niobate (PPLN) crystal and quasi-phase matching to generate the resonated signal, and was also configured with intracavity dispersion compensation and a frequency stabilization system that are covered in detail in later sections.

Two pulse selection systems utilizing high voltage Pockels cells were incorporated into pump probe configuration. The picking rate of each cell could be

independently controlled from 0 to 5 KHz, one for the 808 nm pump and the other for the 1064 nm probe. The two systems were synchronized with each other and to the pulse repetition rate of the titanium sapphire laser by means of a photodiode that monitors the laser output. The combined pulse selection systems enables variable pump and probe rates to be optimized for a given material's relaxation rates.

The last component of the Nd:YAG decay measurements delt with sample orientation and data acquisition. The pump beam was focused down through the sample and optimized for mode overlap with the probe. Each pulse contained approximately 1.75 x 10^{-8} J providing less then 1/4 a percent change in saturation. A mechanical scanning mirror supplied the variable delay and a monochromator spectrally removed the pump signal prior to detection. The detected signals were processed utilizing gated detection, a lock-in amplifier, and computer averaging. No definitive data was recorded suggesting that a more energetic pump pulse was required to lift the probe gain from the noise. Possible future improvements to the experimental design are considered including the construction of a regenerative amplifier and simplified signal processing.

1.2.3 Overview of Equal Pulse Correlation measurments on Exfoliated Graphite

The third portion of the dissertation examines ultrafast relaxations of optically excited carriers in highly ordered pyrolytic graphite films. Mechanically cleaved samples with approximately 16% optical absorption were pumped and probed for changes in transparency using the equal-pulse correlation technique

(EPC). The ECP method uses two identical pulses; the first optically excites carriers in the material, and the second, slightly delayed, probes for changes in transmission due to absorption saturation.

A mode-locked Ti:Sapphire laser centered at 808nm (1.55 eV) was used to degenerately excite and probe the samples. A four (SF-14) prism sequence configured external to the pump laser cavity was used to compensate for dispersion and provided variable pulse widths between 80-150 fs. The total transmission of the sample was recorded as the delay between pump and a probe pulses was swept. The resulting intensity versus delay data was analyzed and the relaxation lifetimes were extracted.

The EPC technique was able to detect ultrafast relaxations that were much shorter than the laser pulse width. A least squares fit algorithm extracted two time constants in the saturation broadened TCP signals. An initial extremely fast relaxation was observed at 11 +/- 5 fs and was attributed to carrier-carrier collisions. A slightly slower relaxation due to carrier-phonon interaction was measured at 150 +/- 30.

1.3 Organization

This dissertation is organized into 6 chapters, including Chapter 1, this introduction. Each chapter includes a brief background of the technical methods and theories on which the dissertation is built. Chapter 2 presents a short introduction to quantum dot lasers and our research into differentially pumped modelocking performance which includes an overview of potential applications for multi-section, differentially pumped devices. Chapter 3 and 4 look at the design and set-up of the non-degenerate time resolved pump-probe system, with

emphasis on the OPO design, stabilization, pulse timing, and data acquisition. Chapter 5 examines the methodology and execution of nonradiative lifetime measurements in Nd:YAG crystals to include, relaxation theory, rate equation analysis, experimental configuration, and results. Chapter 6 is the final chapter and covers the use of the equal pulse correlation technique to measure femtosecond carrier dynamics in photoexcited highly ordered pyrolytic graphite films. The results are reviewed and compared to theory at the end of chapter.

BIBLIOGRAPHY

[1] P. P. Sorokin and J. R. Lankard. Stimulated emission observed from an organic dye, chloro-aluminum phthalocyanine. *IBM J. Res. Dev.*, 10:162–163, March 1966.

[2] J. Valdmanis and R. Fork. Design considerations for a femtosecond pulse laser balancing self phase modulation, group velocity dispersion, saturable absorption, and saturable gain. *IEEE Journal of Quantum Electronics*, 22(1):112–118, 1986.

[3] Cruz C. H. B. Becker P. C. 2. Fork, R. L. and C. V. Shank. Compression of optical pulses to six femtoseconds by using cubic phase compensation. *Opt. Lett.*, 12:483–485, 1987.

[4] Moulton. Spectroscopic and laser characteristics of ti:a$1_2 0_3$. *J. Opt. Soc. Am. B.*, 3(1), 1986.

[5] R. Ell, U. Morgner, F. X. K AÂrtner, J. G. Fujimoto, E. P. Ippen, V. Scheuer, G. Angelow, T. Tschudi, M. J. Lederer, A. Boiko, and B. Luther-Davies. Generation of 5-fs pulses and octave-spanning spectra directly from a ti:sapphire laser. *Opt. Lett.*, 26(6):373–375, Mar 2001.

[6] B. Schenkel, J. Biegert, U. Keller, C. Vozzi, M. Nisoli, G. Sansone, S. Stagira, S. De Silvestri, and O. Svelto. Generation of 3.8-fs pulses from adaptive compression of a cascaded hollow fiber supercontinuum. *Opt. Lett.*, 28(20):1987–1989, Oct 2003.

[7] C. Chudoba, J. G. Fujimoto, E. P. Ippen, H. A. Haus, U. Morgner, F. X. Kärtner, V. Scheuer, G. Angelow, and T. Tschudi. All-solid-state cr:forsterite laser generating 14-fs pulses at 1.3 μm. *Opt. Lett.*, 26(5):292–294, Mar 2001.

[8] D. J. Ripin, C. Chudoba, J. T. Gopinath, J. G. Fujimoto, E. P. Ippen, U. Morgner, F. X. Kärtner, V. Scheuer, G. Angelow, and T. Tschudi. Generation of 20-fs pulses by a prismless cr4+:yag laser. *Opt. Lett.*, 27(1):61–63, Jan 2002.

[9] P. A. Franken, A. E. Hill, C. W. Peters, and G. Weinreich. Generation of optical harmonics. *Phys. Rev. Lett.*, 7(4):118–119, Aug 1961.

[10] M. Bass, P. A. Franken, A. E. Hill, C. W. Peters, and G. Weinreich. Optical mixing. *Phys. Rev. Lett.*, 8(1):18, Jan 1962.

[11] J. A. Armstrong, N. Bloembergen, J. Ducuing, and P. S. Pershan. Interactions between light waves in a nonlinear dielectric. *Phys. Rev.*, 127(6):1918–1939, Sep 1962.

[12] Er'el Granot, Shaul Pearl, and Michael M. Tilleman. Analytical solution for a lossy singly resonant optical parametric oscillator. *J. Opt. Soc. Am. B*, 17(3):381–386, Mar 2000.

[13] J. A. Giordmaine and Robert C. Miller. Tunable coherent parametric oscillation in linbo_3 at optical frequencies. *Phys. Rev. Lett.*, 14(24):973–976, Jun 1965.

[14] Y. Mairesse and F. Quéré. Frequency-resolved optical gating for complete reconstruction of attosecond bursts. *Phys. Rev. A*, 71(1):011401, Jan 2005.

[15] R. Trebino. *Frequency-Resolved Optical Gating: The Measurement of Ultrashort Laser Pulses*. Kluwer Academic Publishers, Norwell Massachesetts, 2002.

[16] Masaaki Tsubouchi and Takamasa Momose. Cross-correlation frequency-resolved optical gating for mid-infrared femtosecond laser pulses by an aggages4 crystal. *Opt. Lett.*, 34(16):2447–2449, Aug 2009.

[17] Victor Wong and Ian A. Walmsley. Analysis of ultrashort pulse-shape measurement using linear interferometers. *Opt. Lett.*, 19(4):287–289, Feb 1994.

[18] Christophe Dorrer and Inuk Kang. Highly sensitive direct characterization of femtosecond pulses by electro-optic spectral shearing interferometry. *Opt. Lett.*, 28(6):477–479, Mar 2003.

[19] Inuk Kang, Christophe Dorrer, and Francesco Quochi. Implementation of electro-optic spectral shearing interferometry for ultrashort pulse characterization. *Opt. Lett.*, 28(22):2264–2266, Nov 2003.

[20] C. Iaconis and I.A. Walmsley. Spectral phase interferometry for direct electric-field reconstruction of ultrashort optical pulses. *Opt. Lett.*, 23(10):792–794, May 1998.

[21] Xuan Liu, Rick Trebino, and Arlee V. Smith. Numerical simulations of the ultrasimple ultrashort-laser-pulse measurement technique, grenouille. In *Conference on Lasers and Electro-Optics/Quantum Electronics and Laser Science Conference and Photonic Applications Systems Technologies*, page JThD8. Optical Society of America, 2007.

[22] Kent C. Burr, C. L. Tang, Mark A. Arbore, and Martin M. Fejer. Broadly tunable mid-infrared femtosecond optical parametric oscillator using all-solid-state-pumped periodically poled lithium niobate. *Opt. Lett.*, 22(19):1458–1460, Oct 1997.

[23] K. C. Burr. *Mid-Infrared Femtosecond Optical Parametric Oscillators and Their Application to the Study of Ultrafast Hole Dynamics in GaAs*. PhD thesis, Cornell University, Ithaca, NY, 1999.

CHAPTER 2

DIFFERENTIAL PUMPING OF QUANTUM DOT LASERS

This chapter examines the effects of differential pumping (nonuniform current injection) on mode-locked quantum-dot laser performance. A reconfigurable quantum-dot (QD) laser recently developed by the Center for High Technology Materials (CHTM) at the University of New Mexico provided an exceptional platform for pumping scheme evaluation. The lasers tested are all based on dots-in-a-well (DWELL) technology and are evaluated over a large range of injector currents. This work was partially funded under support of the Air Force Office of Scientific Research in collaboration with the Air Force Research Laboratory and the University of New Mexico.

2.1 The Increasing Role of Electro-Optic Systems in Military and Global Security Operations

Electro-optic systems play a crucial role in providing information to today's war fighters, security forces, and rescue personnel. These systems are used by all branches of service to perceive and control the battlespace. They protect military personnel and equipment by allowing the battle to be fought at standoff distances away from the enemy. Their high precision of weapons delivery protects civilians and reduces collateral damage, resulting in higher munitions-to-target ratios while fostering the military's public image. They provide real time data to security forces and rescue personnel reducing the potential of mishap while allowing fast and efficient response in times of emergency. With applica-

tions in national defense, homeland security, boarder control, law enforcement and rescue operations, it is clear that our reliance on Electro-optic sensing systems is extensive and vital to our nation's security.

The generation of stable mode-locked pulses is critical for further development of high speed optical clocks, optical A-D converters, and optical interconnects, with applications in arbitrary waveform generation (AWG) and imaging laser radar. Semiconductor lasers are compact, low power consuming sources with proven reliability and performance. Their direct electrical pumping scheme allows for straightforward implementation into an astonishingly wide range of applications and products. First demonstrated by Robert Hall, Gunther Fenner, and researchers at General Electric in 1962 [1], semiconductor lasers offered the promise to revolutionize home and industry. Since then semiconductor lasers have undergone continual improvement. In order to realize the predicted potential of semiconductor lasers, parallel advancements in enabling disciplines were needed. Developments in material science, crystal growth, and fabrication, along with breakthroughs in device design, provided the means allowing semiconductor lasers to mature [2]. A major step towards the commercial utilization of semiconductor lasers was taken in 1970 when Zhores Alferov from Russia demonstrated continuous room temperature operation of a double heterostructure GaAs laser [3, 4, 5]. This work formed the foundation of research that would later earn Alferov the Nobel Prize in Physics for the year 2000. The accomplishment of continuous wave lasing at room temperature sparked intense interest in semiconductor physics research around the world leading to rapid advancement in laser design. By the late 1970s, distributed feedback lasers and distributed Bragg reflector lasers allowed for improved wavelength selection and single mode operation through the use of periodic cavity struc-

tures [6, 7]. At this time the performance and power of semiconductor lasers were limited in part by the nonuniform results of fabrication using liquid phase epitaxy (LPE).

Two modern epitaxial growth process were being developed during this period which would provide precise control over crystal composition and deposition far surpassing that of LPE. Known as metallorganic chemical vapor deposition (MOCVD) and molecular beam epitaxy (MBE), these two new tools permitted increased laser output and the eventual development of active quantum structures. Quantum well lasers which were a direct progression from the DHS sources made their appearance in 1975 [8], but did not reach competitive performance until 1978 [9]. With increased electron confinement (1-D), quantum well lasers soon outperformed conventional bulk lasers in many respects [9]. They offered improved wavelength selectability, increased efficiency, higher power output, lower threshold currents, and reduced linewidth enhancement factors [10]. The merits of quantization with respect to semiconductor lasers became apparent as researchers began to examine the possibilities of multidimensional confinement.

The effects of two and three dimensional quantum confinement (quantum wires and quantum dots respectively) were theoretically explored in a paper written by Arakawa and Sakai in 1982 [11], but the progress of quantum dot lasers development was slow until the advent of self-assembly techniques which resulted in the first quantum dot laser demonstration in 1993 [12]. Today, quantum dot lasers have many advantages over quantum well and bulk semiconductor lasers. Quantum dot lasers offer reduced threshold current density, reduced sensitivity to temperature fluctuations, high power operation, and expanded wavelength ranges when compared to other types of semiconductor

lasers.

Low power compact laser pulse sources are ideal for applications in clock signal generation, high speed optical communications, electro-optic sampling, and photonic quantum computing. Semiconductor mode-locked laser diodes offer a reliable, compact, low power source for such applications, but they traditionally have not possessed the required stability. The broad gain spectrum and temperature tolerant operation available in quantum dot lasers makes them an excellent candidate for applications that require stable pulse sources. In this chapter, a monolithic two-section quantum dot semiconductor laser is subjected to various nonuniform current injection profiles while mode-locking stability is examined. The reconfigurable design of the quantum dot lasers tested in this work was ideal for rapid evaluation of experimental mode-locking techniques.

2.2 Why Quantum Dots

Semiconductor lasers utilizing quantum dot (QD) active regions have recently been used to generate stable optical pulses and provide an exceptional platform for the development of compact agile emitters at optical frequencies. QD semiconductor lasers offer low threshold current densities, reduced linewidth enhancement factors, reduced timing jitter, and high modulation bandwidth as compared with bulk or quantum well devices [13]. They show great potential for the generation of short pico-second pulses due to the wide bandwidth of the inhomogeneously broadened gain spectrum. A unique recently developed QD laser was used here that enabled exploitation of these strengths through a reconfigurable multisection device [3]. This allowed for rapid testing of design concepts while minimizing the required fabrication.

Such a device was used in this work to explore the effects of differential gain pumping. Since the temporal features of a pulse are related to its spectral properties through the Fourier transform, an alteration of a signal's frequency content will affect the temporal pulse shape. In this work differential pumping (nonuniform injection currents into the gain medium) was shown to provide a degree of control over the spectral content and bandwidth of the mode-locked laser output. This technique can be used to optimize a particular device's pulse characteristics, such as pulse length or frequency chirp content by appropriate tailoring of the pumping schemes.

2.3 Experiment

A monolithic two-section quantum dot semiconductor laser was differentially pumped in order to explore the effects on spectral content and mode-locking stability. The device tested operates near 1245 nm and is passively mode- locked at a repetition rate of approximately 5 GHz through the use of a reverse biased saturable absorber as depicted in figure 2.1.

The gain region is electrically isolated from the absorber section during fabrication by proton implantation, providing a highly resistive barrier greater than 10 MΩ [14]. The cleaved mirror on the absorber side of the device was coated for high reflection while the mirror adjacent to the gain section was low reflection coated for high output power. The gain region can be probed directly through any or all of the four contact pads located on the device. Although the four regions of the gain section corresponding to each pad were not electrically isolated, they provided the means to pump the gain medium with nonuniform current densities by virtue of the finite resistance of the metal anode between

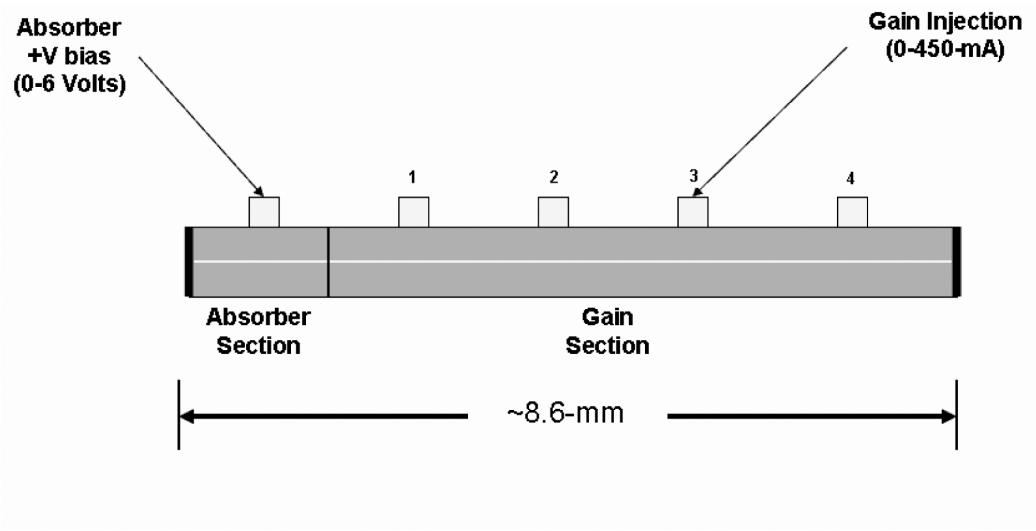

Figure 2.1: A graphic depicting the device design used during differential pumping. The absorber section is electronically isolated from the gain medium. The tabs on the top of the device represent probe pads.

them. Figure 2.2 shows the experimental configuration used during all testing.

Each chip (containing up to 18 devices) was mounted to a TE cooler and maintained at a constant temperature of 25 degrees Celsius. An ILX LDC-3900 4-channel current source controlled both the TE cooler and the injection currents. An Amrel PPS-1202 programmable DC power supply controlled the absorber bias voltage. Both the voltage ramp profile and the current ramp profile are controlled via a LabView script. The laser output was coupled into a single-mode polarization maintaining lensed-tip fiber and an isolator was used to minimize feedback into the cavity of the device. The output of the isolator could be connected to a Femtochrome FR-103XL autocorrelator, an Ando AQ6317B optical spectrum analyzer, or a 50 GHz HP 8565E electronic spectrum analyzer via a New Focus 45 GHz IR optical detector and amplifier. All equipment but the autocorrelator was remotely operated through a LabView script. To measure the average power, an Oriel 70451 four-inch integrating sphere and Newport

883 IR detector were used. The integrating sphere was chosen over complicated coupling optics to ensure the highest possible accuracy when measuring the average output power during experimentation. The integrating sphere and detector were calibrated from a reference source.

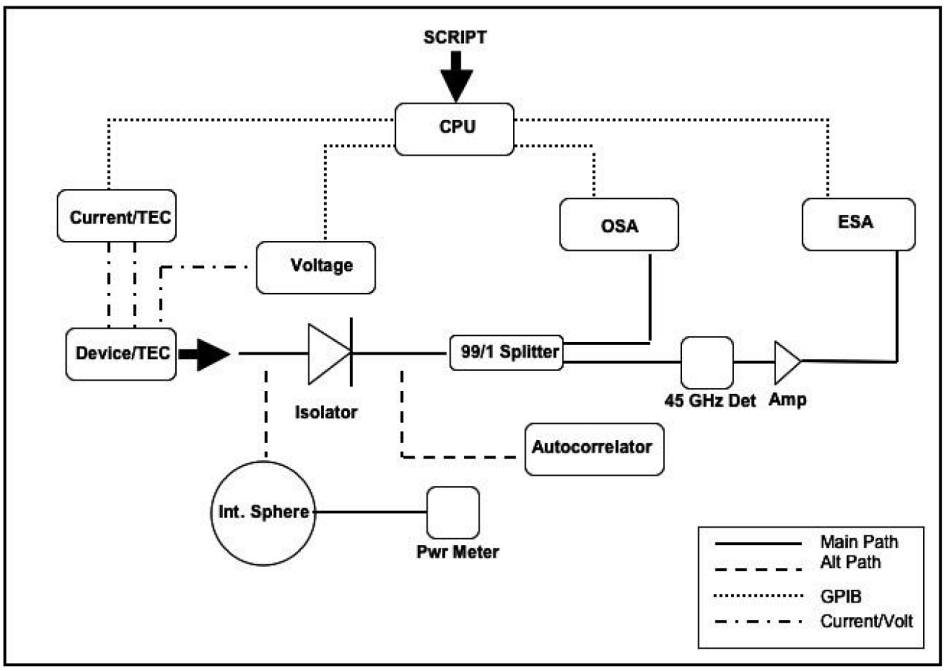

Figure 2.2: Experiment layout. Device output is coupled into polarization maintaining fiber or directly into an integrating sphere. OSA is optical spectrum analyzer, ESA is electronic spectrum analyzer, and TEC is temperature controller.

The LabView script that controlled data collection was executed via a graphical user interface. The current and voltage ramp profiles used for device testing were sequentially repeated to take multiple characterizations which required runtimes between 30 to 90 minutes that depended on measurement resolution and number of ramps. Typical voltage and current resolutions were respectively set at 0.1 V and 10 μA. The data was recorded in text files and examined in MATLAB.

2.3.1 The Laser Devices

The quantum dot lasers were composed of a single-mode ridge waveguide divided into two electrically isolated sections as is covered in detain in Yongchun Xins PhD dissertstion [15]. One section serves as a saturable absorber while the other is used for gain. Both the gain and absorber sections were made from the same material but have separate electronic contacts for customized biasing. The absorber was located adjacent to the high reflector to ensure mode-locking at the round-trip frequency. Control of the reverse bias voltage provided the means of regulating the absorbtion depth and recovery time and thus influenced the mode-locked pulse width. The second section served as the gain region with four electronic contacts for pumping. The optical properties of this section were regulated through control of the current density sent through each pad. Low bias voltages were used to achieve optical transparency or low gain while large biases provided strong population inversion and high gain. In this manner, the devices were reconfigured through systematic changes in absorber bias voltages and gain section injection currents.

2.3.2 Single Pad Pumping

The first part of the experiment explores the effects of separately pumping each of the four pads. Each pad was individually injected with 150 mA of current while holding the absorber reverse bias voltage constant at 3 volts. The spectral content of the output was recorded as shown in figure 2.3. It was demonstrated that pad selection alone has a relevant impact on the optical spectrum. Locking across a continuous spectrum of modes tended to occur at the pad 1 and 2

locations that are closer to the absorber section. However, two sets of locked modes were observed when the pumping was located towards the output facet. The explanation for this behavior is not exactly known at this time but could be related to photon density variation in the cavity and optical non-linearities induced by this phenomenon.

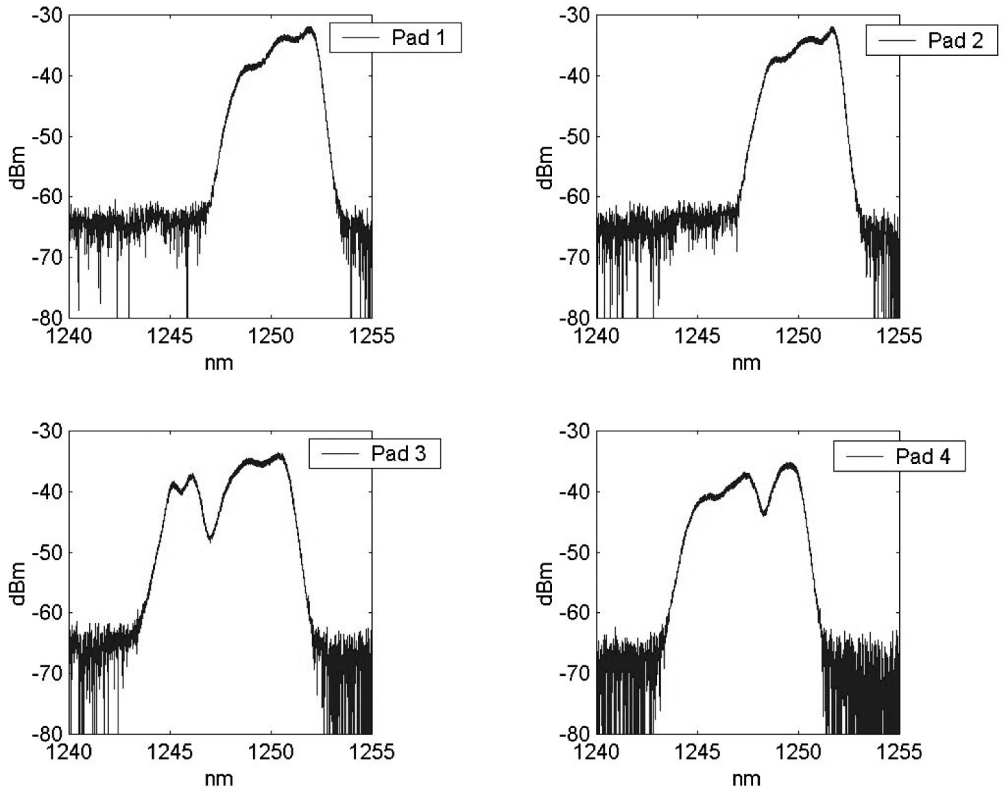

Figure 2.3: Plots showing the spectral content of the laser's output during single pad current injection of 150 mA at each of the corresponding probe pads. The bias voltage on the absorber was held constant at 3 V. The modulation on the optical spectrum is most likely due to optical modes induced by the transparent GaAs substrater.

In addition to the spectral content, maps showing the stable mode-locking combinations of injection current and bias voltages were generated for each pad. The presence of a strong fourth harmonic in the electronic spectrum was used

as the indication of good mode-locking [16]. The map data was recorded as the current and reverse voltages were varied over their respective ranges of 0-200 mA in 10 mA increments and 0 to 6 volts in increments of 0.25. The results are shown in figure 2.4. Pads one and four show comparable regions of mode-locked operation and are similarly limited to a bias voltage of around 4 volts. Pads two and three which are located towards the inner region of the gain section allow for addition pulse shaping possibilities by providing mode-locked output at reverse bias voltages reaching nearly six volts. Utilization of this available increase in absorber bias allows for a reduced minimum recovery time and thus, a minimized pulse width. The threshold current was not found to vary significantly based on pad selection.

2.3.3 Multiple Pad Pumping

The spectral effects of differentially pumping two pads simultaneously were also of interest. Figure 2.5 shows how the shape of the optical spectrum can be controlled and broadened in an attempt to influence the pulse characteristics. In this experiment both the injection currents (pads 1 and 4) and the bias voltage were altered in order to produce symmetric spectrums of differing breadth. During experimentation, both positive and negative spectral chirps were observed. Future experimentation can expand on this research to include the effects of differential pumping on pulse shape through the use of frequency resolved optical gating with the hope that the broader spectrums achieved through differential pumping will allow for shorter pulse generation. Whether or not this technique can be used as a tool to manipulate pulse shape is the focus of further investigation.

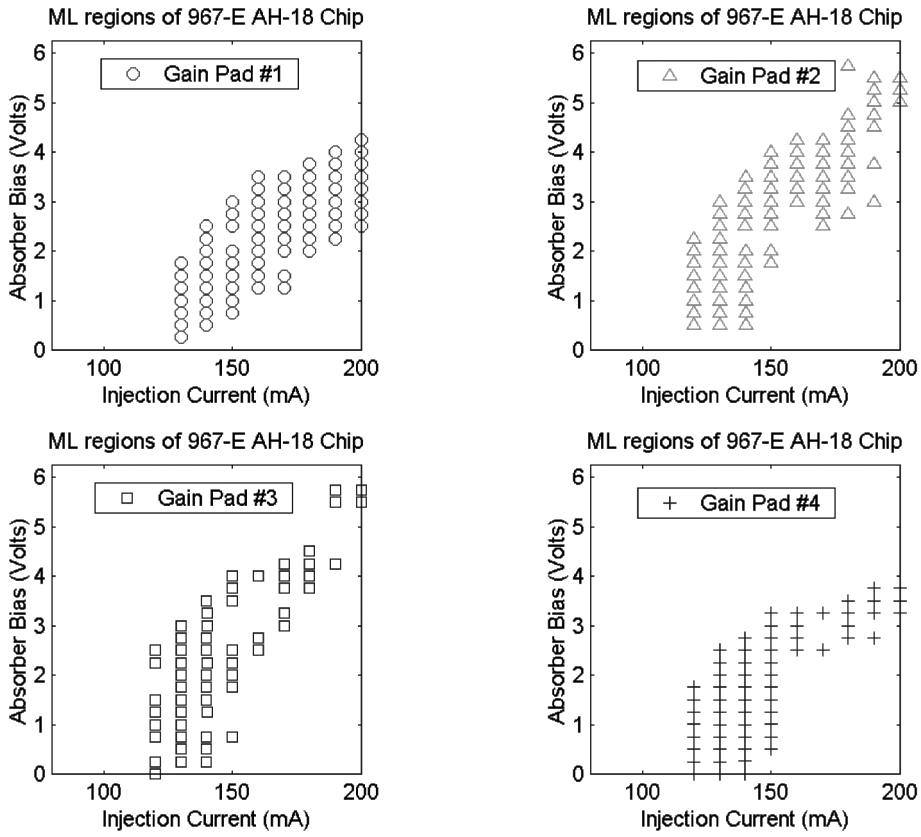

Figure 2.4: The mode-locked regions of operation for the device as a function of injection current and absorber bias voltage. Note how the available range of bias voltages that allow mode-locking is expanded for the inner pads (2 and 3) when compared to the pads on the outer regions of the gain section (1 and 4).

Differentially pumping pads 1 and 4 not only altered the spectrum but had a large impact on average power. The integrating sphere was used to capture the emitted power and was placed directly at the output facet. Figure 2.6 shows the relationship between differential current injection and average output power. It can be seen that maximum average power was obtained when the current was evenly divided between the pads. This does not necessarily correspond to the highest quality mode-locking and trade offs between high average power and short pulse lengths are necessary.

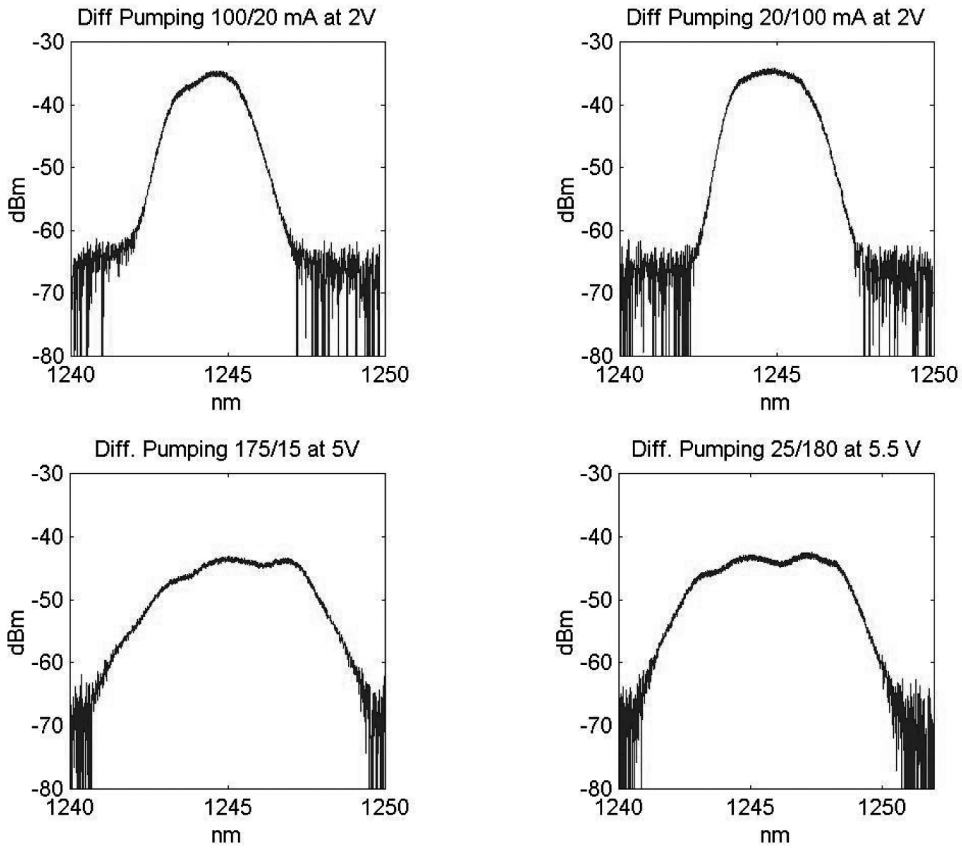

Figure 2.5: Plots of the optical spectrum from a single device under separate differential pumping schemes. The injection currents correspond to pads 1 and 4 respectively. Note how the symmetry and width of the spectrums were improved when compared to single pad injection method as shown in figure 3. The modulation on the spectra is most likely due to optical modes induced by the transparent GaAs substrate.

Good mode-locking was also observed with reverse bias voltages as high as 6.5 volts when pad 1 was pumped with 165- 175 mA and pad 4 was simultaneously pumped with 35-25 mA, further expanding on the quality mode-locking region when compared to single pad pumping.

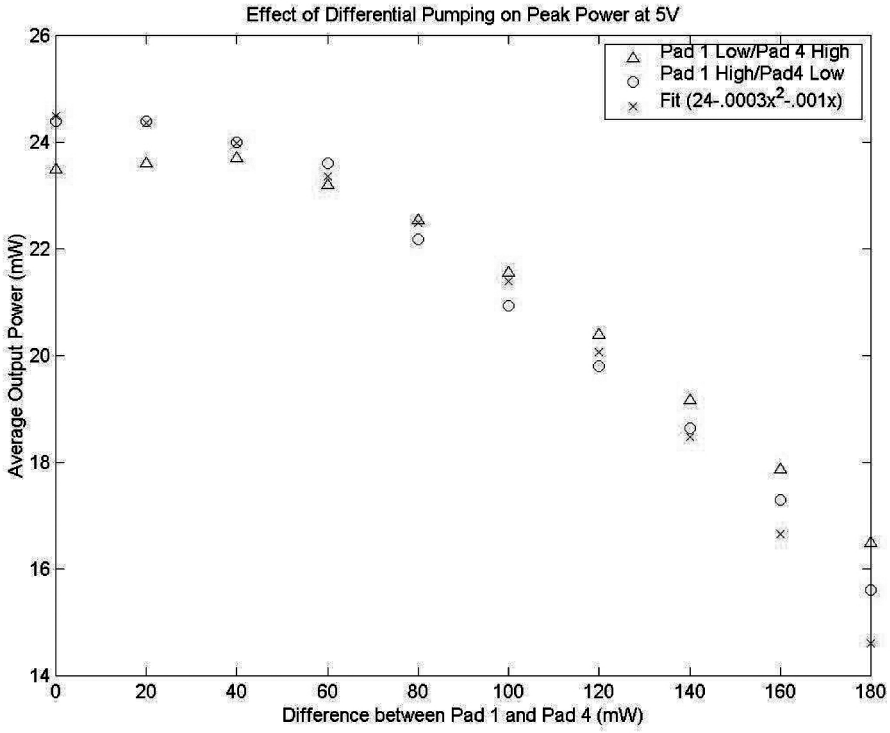

Figure 2.6: This graph shows the relationship between the differential pumping of pads 1 and 4 with the corresponding average output power. The absorber bias voltage was held constant at 5 V.

2.3.4 Wavelength Tuning

The possibility of wavelength tuning through the use of differential pumping was briefly explored. The center wavelength of operation was successfully shifted from 1246 nm to 1257 nm as can be seen in figure 2.7. Mode-locked operation was maintained during the transition but the quality of the mode-locked output was not verified at the time of this writing. It would be of great interest to demonstrate tunable continuous wave and mode-locked operation over this band by controlling the injection currents into the gain section and reverse bias voltage on the absorber. This would provide the possibility of a wavelength

modulated output directly from the source without the need for external beam manipulation.

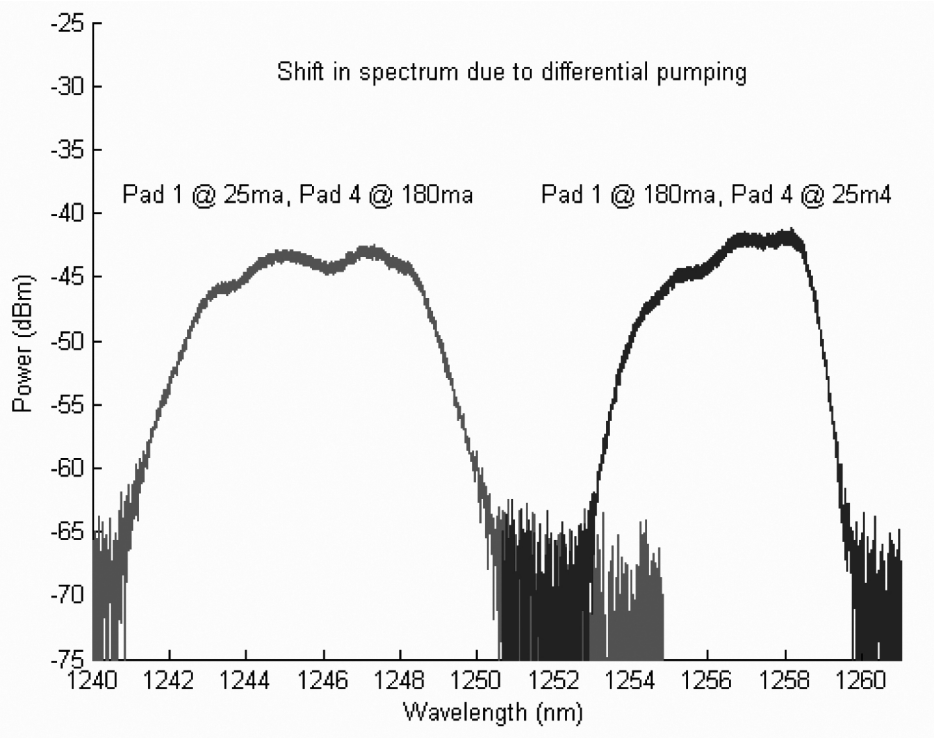

Figure 2.7: This plot shows the optical spectrums for two separate differential pumping schemes as applied to a single device. The total current was held constant while the amount entering pads 1 and 4 were reversed. The reverse bias was held at 3 V. The center frequency shifted nearly 12 nm.

2.4 Results and Conclusion

It has been shown that the symmetry and breadth of a QD MLL's spectrum can be manipulated through differential gain pumping even though the pumped partitions were not electrically isolated. This provides a simple and inexpensive method of optimizing the semiconductor laser performance. The re-

gions of mode-mocked operation with respect to injection current and absorber bias were shown to have a strong dependence on the location of the injected current within the gain medium and on the differential pumping scheme implemented. Significantly greater absorber bias voltages were available during differential pumping as compared to single pad current injection; thereby reducing absorber recovery time as well as the inferred pulse length. The enhanced spectral bandwidth provided by differential pumping offers still further pulse length reduction. The capacity for wavelength tuning was also demonstrated by differential pumping with a center wavelength shift of approximately 12nm.

The techniques for spectral broadening and control, paired with the wavelength tunability demonstrated in this effort have many potential applications which include signal processing and waveform generation. The rest of this section looks at the utility of multi-section semiconductor based lasers and how the results presented in earlier parts of this chapter suggest a great potential for such devices. There relevance in harmonic and hybrid mode-locking schemes is examined as is the concepts potential applications in free space frequency modulated communications and as stable pulsed timing sources.

2.4.1 Absorption Recovery in Reverse Biased Saturable Absorbers

The attributes of these passively mode-locked lasers are influenced by the interaction of the intracavity pulses with the gain and the absorber sections of the device. It is well known that in lasers that utilize saturable absorption for mode-locking that the pulse characteristics are highly dependent on absorber

strength, recovery times, and input pulse energies. Multi-section semiconductor lasers similar to those examined in this work provide a degree of control over such parameters.

Simplified rate equations for a semiconductor saturable absorber can be written as [17, 18]:

$$\left(\frac{dN}{dt}\right) = g_o \frac{(N - n_{th})S}{1 + \epsilon S} - \frac{N}{\tau_a} \tag{2.1}$$

and also

$$\left(\frac{dS}{dt}\right) = -g_o \Gamma \frac{(N - n_{th})S}{1 + \epsilon S} - \alpha S \tag{2.2}$$

where N is the carrier density, S is the photon density, g_o is differential absorption or the absorption as a function of wavelength, N_{th} is the threshold current density, ϵ is the nonlinear absorption coefficient, τ_a is the absorption recovery time, Γ is the confinement factor of the waveguide, and α is waveguide loss.

Management of the reverse bias voltage on the saturable absorber directly influences the overall differential absorption (g_o) and recovery time (τ_a) of the material, such that increased reverse bias voltages result in increased absorption and reduced recovery times. The resultant variations of absorption and recovery affect the pulse shaping characteristics of the device. Short pulse absorption has been shown to systematically scale nearly 20 dB in waveguide saturable absorbers over a 0 to 10 V sweep in the reverse bias voltage and fast recovery times were reduced by two orders of magnitude [19] which can be used for pulse shaping.

Pulse energies also play a significant role in absorber pulse shaping. Saturable absorption in semiconductor materials can often be broken down into three pulse energy behaviors. At low pulse energies that are much less than saturation energy of the absorber ($E_p < E_{sat)}$), the percent transmitted is independent of pulse energy. But at higher energies ($E_p \approx E_{sat)}$) the leading edge

of the pulse begins to saturate the absorber allowing a greater percentage of the pulse energy to pass unabsorbed. This trend continues until two-photon-absorption becomes prevalent resulting in increased absorption. Thus two photon absorption could be a limiting factor for the use of these materials in high power systems or for ultrashort pulse generation.

Purely passive mode-locking often suffers from instabilities and timing jitter. Hybrid mode-locking schemes that rely on the ability to modulate gain and absorption in multisession devises can help stabilize laser operation with reduced timing jitter [20]. Active modulation of the gain and/or absorber regions is easily accomplished with voltage supplies synchronized to the pulse repetition rate of the device. Our earlier work in the active stabilization of erbium doped waveguide lasers found the limiting factor of laser performance to be the timing jitter of the modulated voltage supplies [21]. Hybrid mode-locking has proved useful for pulsed stabilization and may also play a role in the operation of devices with selectable harmonic mode-locked pulse repetition rates.

2.4.2 Harmonic mode-locking of multi-section lasers

Pulse repetition rates greater than that generated by the fundamental frequency of the laser cavity can be realized through harmonic mode-locking. In harmonic mode-locking multiple pulses circulate in the cavity at equal temporal intervals. Multi-section devises where absorber regions can be placed at harmonic locations within the cavity, provide a novel way to reach THz rate optical pulse generation or to reconfigure a lasers pulse repetition rate on the fly through control of bias voltages. THz rate optical pulse generation (1.54 THz) was recently demonstrated by a harmonically mode-locked distributed Bragg

reflector laser [22]. Devices similar to those examined here could provide the means to change pulse repetition rates simply by reconfiguring the pumping geometry. Careful choice of absorber location at harmonic periods within the cavity can result in selective harmonic mode-locking.

2.4.3 Frequency Modulation of Laser Sources for Free-Space Communications

Laser beams can carry information through optical modulation. Currently most optical communications systems use amplitude modulation (AM) or on-off-keying (OOK) with direct detection [23]. Amplitude modulation as a form of data transmission is susceptible to distortion and loss caused by atmospheric elements like dust and fog limiting its applications in free space communications. Direct information transfer through line-of-site laser communications systems offers greater mobility than fiber optic systems with increased security over wide area broadcasts. The military and other government agencies can benefit from line-of-site laser communications for satellite to space and satellite to ground systems as well as intratheater communications between air and ground platforms. All optical networks offer extremely high data transmission rates which could alleviate much of the bandwidth problems seen in today's data intensive sensor platforms. Additionally, the interception of transmitted signals by unwanted parties becomes much more difficult with line-of-site systems which can also provide notifications of these unauthorized interceptions.

Differentially pumped lasers may offer a direct method of frequency modulation (FM) that is much more robust against environmental factors when com-

pared to amplitude modulation. Frequency modulation uses excess bandwidth to enhance signal to noise ratios in data transmissions, reducing transmitter power requirements [24], which is vital to the size weight and power limitations of mobile air platforms. The fundamental tuning mechanisms used in semiconductor lasers include cavity length control though modulated mirrors and mode selection through variable index or grating angle [25]. The lasers outlined here have shown that frequency tuning is possible with differential pumping giving a demonstrated tuning range 12 nm. An estimate of the achievable bandwidth that comes from this level of tuning is given by

$$\Delta\nu = \frac{c}{\lambda^2} \cdot \Delta\lambda \tag{2.3}$$

where c is the speed of light, λ is the center wavelength which is 1250 nm in this case, and $\Delta\lambda$ is the tunable bandwidth of 12 nm. This gives a frequency range of $\Delta\nu$=2000 GHz or a single-channel bandwidth of near 700 GHz. To utilize the advantages of frequency modulation the signal bandwidth is constrained by the following relationships [24].

$$f_s << \Delta\nu << f_o \tag{2.4}$$

and

$$\Delta f_o << \Delta\nu \tag{2.5}$$

where f_s is the single channel signal bandwidth, Δf is the frequency tuning range, f_o is center laser line, and Δf_o is the laser linewidth, as depicted in figure 2.8. Quantum dot lasers are certainly capable of meeting these requirements and they have the additional ability to be engineered for general wavelength regions and bandwidths by controlling the geometry of the dots.

Wavelength tuning is only one factor in a long list of requirements for a high quality tunable laser, and much more testing is required to quantify differential

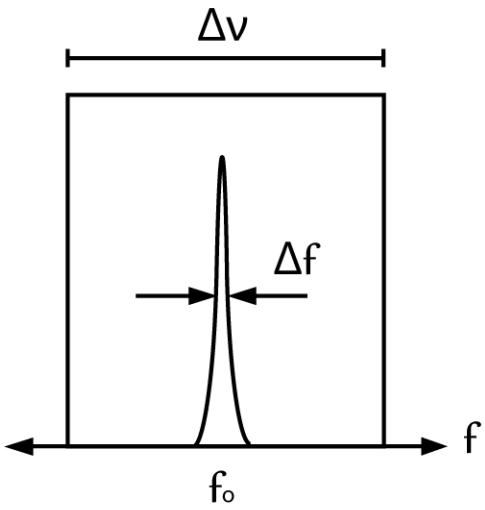

Figure 2.8: The relationship of the frequencies involved with FM communications.

pumping as a viable tuning method. Tuning speed, spectral purity, side mode suppression, output power, stability, and reliability must all be considered [26]. Other semiconductor based tunable lasers are already used in telecommunication applications, such as distributed feedback lasers, distributed Bragg reflector lasers, and vertical-cavity surface-emitting lasers. Frequency modulation through differential pumping adds one more trick to the designers arsenal.

BIBLIOGRAPHY

[1] R. N. Hall, G. E. Fenner, J. D. Kingsley, T. J. Soltys, and R. O. Carlson. Coherent light emission from gaas junctions. *Phys. Rev. Lett.*, 9(9):366–368, Nov 1962.

[2] D. F. Welch. A brief history of high-power semiconductor lasers. *EEE Journal on Selected Topics in Quantum Electronics.*, 6(6), Dec 2000.

[3] D.Z. Garbuzov Y.V. Zhilyaev E. P. Morozov E. L. Portnoi Z.I. Alferov, V.M Andreev and V. G. Trofim. Investigation of the influence of the alas-gaas heterostructure parameters on the laser threshold current and the realization of continuous emmission at room temperature. *Fiz. Tekn. Poluprovodn*, 4:1826–1829, 1977.

[4] P. K. Tien. Integrated optics and new wave phenomena in optical waveguides. *Rev. Mod. Phys.*, 49(2):361–420, Apr 1977.

[5] Z. I. Alferov. Double heterostrucure lasers: Early days and future perspectives. *IEEE Journal on Selected Topics in Quantum Electronics*, 6(6), 2000.

[6] Onaka K Okuda M. Analysis of distributed bragg-reflector laser-amplifiers. *Japanese Journal of Applied Physics*, 16(1), 1977.

[7] Evens G. and Wilcox T. Mode-coupling and distributed feedback lasers in periodic fiber waveguides. *IEEE Journal of Quantum Electronics*, 13(4), 1977.

[8] R. C. Miller W. Wiegmann J. P. van der Ziel, R. Dingle and W. A. Nordland Jr. Laser oscillations from quantum states in very thin gaas-al0.2ga0.8 multilayer structures. *Appl. Physics Letters*, 25:463–465, 1975.

[9] R.D. Dupuis, D. P. Dapkus, N. Holonyak, E. A. Rezek, and R. Chin. Room-temperature laser operation of quantum-well ga/1-x/alxas-gaas laser diodes grown by metalorganic chemical vapor deposition. *Appl. Physics Letters*, 32:295–297, 1978.

[10] P. S. Zory. *Quantum Well Lasers*. Academic Press Inc, Burlington Massachesetts, 1978.

[11] Y. Arakawa and H. Sakaki. Multidimensional quantum well laser and temperature dependence of its threshold current. *Applied Physics Letters*, 40(11):939–941, 1982.

[12] N. N. Ledentsov, V. M. Usinov, and A Yu Egorov. Optical properties of heterostructures with ingaas-gaas quantum clusters. *Semiconductors (Engl. Transl.)*, 28(8):32–834, 1994.

[13] Sergey Melnik, Guillaume Huyet, and Alexander Uskov. The linewidth enhancement factor α of quantum dot semiconductor lasers. *Opt. Express*, 14(7):2950–2955, Apr 2006.

[14] Allen L. Gray Hua Huang Srivatsa P. G. Kutty Hua Li John Nagyvary Faisal Nabulsi Leonard Olona Edwin Pease Qi Sun Chris Wiggins John C. Zilko Zhengzhong Zou Lei Zhang, Ling-Shen Cheng and Petros M. Varangis. High-power low-jitter quantum-dot passively mode-locked lasers. Physics and Simulation of Optoelectronic Devices XIV. Proc. SPIE 6115, February 2006.

[15] Yongchun Xin. *Quantum Dot Multi-section Light Emitters*. PhD thesis, University of New Mexico, 2006.

[16] D. Murrell V. Kovanis Y.-C. Xin K. Brown, M. Fanto and L.F. Lester. Automated analysis of stable operation in two-section quantum dot passively mode locked lasers. Physics and Simulation of Optoelectronic Devices XV. Proc. SPIE 6468, March 2007.

[17] Dug K. Kim. Reverse bias voltage dependent pulse shape and transmission change through a semiconductor saturable absorber. *Applied Physics Letters*, 69(18):2635–2637, 1996.

[18] J. Yu and D. Bimberg. Suppression of self-pulsation for tens of gigahertz optical pulses from passively mode-locked semiconductor lasers. *Applied Physics Letters*, 67(22):3245–3247, 1995.

[19] F.; Mork J.; Yvind K.; Hvam-J.M.; Hanberg J. Romstad, F.; Ohman. Short pulse absorption dynamics in a p-i-n ingaasp mqw waveguide saturable absorber. 28th European Conference on Optical Communications. Optical Communication ECOC, Sep 2002.

[20] Y.; Arahira, S.; Ogawa. Passive and hybrid modelockings in a multi-electrode dbr laser with two gain sections. *IEEE Elect. Lett.*, 31(10):808 – 809, 1995.

[21] B.Wysocki J. Malowicki M. Fanto, R.Erdmann and T.McEwen. Ultra-stable harmonically mode-locked erbium-doped waveguide laser. *Proc. SPIE 6527*, 2007.

[22] Shin Arahira, Saeko Oshiba, Yasuhiro Matsui, Tatsuo Kunii, and Yoh Ogawa. Terahertz-rate optical pulse generation from a passively mode-locked semiconductor laser diode. *Opt. Lett.*, 19(11):834–836, Jun 1994.

[23] Joseph Kahn. Modulation and detection techniques for optical communication systems. In *Optical Amplifiers and Their Applications/Coherent Optical Technologies and Applications*, page CThC1. Optical Society of America, 2006.

[24] S. Luryi. Feasibility of an optical frequency modulation system for free-space optical communications. *International journal of high speed electronics and systems*, 16(2):559–566, 2006.

[25] Larry A. Coldren, G. A. Fish, Y. Akulova, J. S. Barton, L. Johansson, and C. W. Coldren. Tunable semiconductor lasers: A tutorial. *J. Lightwave Technol.*, 22(1):193, Jan 2004.

[26] Cunyun Ye. *Tunable External Cavity Diode Lasers*. World Scientific Pub Co Inc, Hackensack, NJ, 2004.

CHAPTER 3

OPTICAL PARAMETRIC OSCILLATOR BACKGROUND INFORMATION

3.1 Nonlinear Material Properties

An atomic system's response to an applied electric field is to create a polarization that tries to follow the field. This is a reasonable assumption at low optical intensities where the restoring forces inside the material are linear and balanced. Atoms in a material possess a position of least energy where the separation distance between adjacent nuclei results in a balance of repulsive and attractive forces. It is in this regime that linear material responses take place. Extremely strong optical intensities force the system to behave nonlinearly and can even break molecular bonds at electric field intensities on the order of 10^{13} W/cm^2. The interaction of electromagnetic waves with a dielectric material can be expressed with the wave equation:

$$\frac{\partial^2 E}{\partial r^2} - \frac{1}{c_o^2}\frac{\partial^2 E}{\partial t^2} = \mu_o \frac{\partial^2 P}{\partial t^2} \tag{3.1}$$

where E is the real electric field, P is the real induced polarization, c_o is the speed of light in a vacuum, and μ_o is magnetic permeability of free space. The induced polarization is a function of the applied electric field and the material susceptibility. It characterizes the interaction between the light and the medium. In linear optics the induced polarization of a material is assumed to be proportional to the applied electric field where the principal of superposition applies. This suggests that multiple beams traveling within a medium do not interact and that the resulting atomic response does not generate frequencies other than those present in the applied fields. This is a valid simplification at low intensities where no appreciable nonlinear interactions occur, but when the optical

intensity is high, this assumption no longer holds true. Under high intensity excitation the induced polarization in a real material is not proportional to the applied electric field but is a function of higher order terms as given in this Taylor series expansion [1]:

$$P = \epsilon_o[\chi^{(1)}E + \chi^{(2)}E^2 + \chi^{(3)}E^3...] \tag{3.2}$$

where χ is the susceptibility of the material to polarization and the superscripts (1), (2), and (3) represent the linear, second-order, and third-order susceptibilities respectively. The linear first term ($\chi^{(1)}$) is dominant when the optical intensities are kept low inside the medium and the material can follow the electric field linearly. The linear susceptibility is responsible for optical absorption and normal dispersion. High intensities lead to nonlinear responses where new optical frequencies are generated and multiple beams begin to interact inside the material. Odd-order susceptibilities ($\chi^{(1,3,\cdots)}$) occur in all substances while even-order susceptibilities are limited to materials without inversion symmetry. Second order effects ($\chi^{(2)}$) include second harmonic generation (SHG), sum frequency generation (SFG), difference frequency generation (DFG), and parametric down conversion (PDC). Third-order responses include Third-harmonic generation (THG), four-wave mixing, self-focusing, and self-phase modulation cross-phase modulation. Higher order nonlinear processes exist but will not be mentioned here.

Optical parametric amplification is especially important towards the design of the nondegenerate pump probe experimentation used in this work and is a second order three-wave interaction based on difference frequency generation which amplifies lower energy waves by splitting the energy of a pump photon. The gain obtained from optical parametric amplification is the basis for the construction of optical parametric oscillators.

3.2 Optical Parametric Oscillators

An optical parametric oscillator (OPO) is a device that utilizes a resonant cavity and an optical gain medium (in this case parametric amplification in a non-linear crystal) to generate coherent light which leads to gain in the lower frequency waves. An OPO down converts single photons into two photons of reduced energy by means of nonlinear frequency conversion or optical parametric generation. The original photon by convention is referred to as the pump while the two resulting photons of lesser energy, are called the signal and the idler. The conservation of energy and momentum dictates that the pump, signal, and idler photons be related by the following two relations:

$$\omega_{pump} = \omega_{signal} + \omega_{idler} \tag{3.3}$$

and

$$\mathbf{K}_{pump} = \mathbf{K}_{signal} + \mathbf{K}_{idler} \tag{3.4}$$

where the photon frequency (ω) is related to its energy (E) by E=$\hbar\omega$ and the specific energy values that the signal and idler take is determined by the momentum relationship or phase-matching condition as depicted in equation 3.4. Thus the signal and idler wavelengths can be controlled or tuned through manipulation of the phase-matching condition which is discussed in more detail in the next section. It is this tunability coupled with the fact that OPOs often have output wavelengths that are difficult or impossible to achieve directly with current lasers, and that they are capable of providing continuous wave operation as well as pulses in the tens of femtoseconds [2], that give them their utility.

Optical parametric amplification is the nonlinear effect that provides the signal and idler gain within an OPO. The energy conversion of a pump photon into the signal and idler is complete and does not result in heat deposition in the

crystal allowing the use of extreme energy densities within the crystal without damage. This is important since in any nonlinear device high optical intensities are required for efficient operation. A simplified block diagram showing the basic concept of optical parametric amplification is given in figure 3.1. The in-

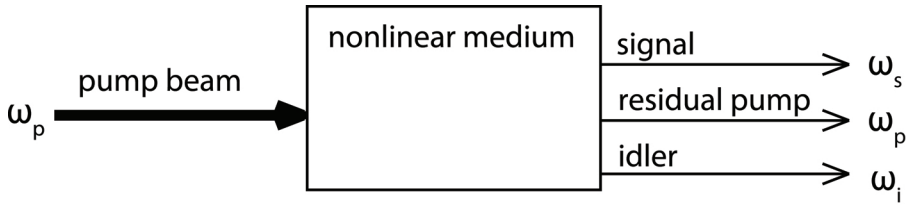

Figure 3.1: Simplified diagram depicting optical parametric amplification.

teraction of the three waves involved in optical parametric amplification can be characterized through coupled-amplitude equations as described in [3, 4] utilizing plane-wave interaction and the slowly-varying amplitude approximation outlined below with equations adapted from [5].

$$\left|\lambda_i \frac{\partial E_i}{\partial z}\right| << |E_i| \quad \text{and} \quad \left|\frac{\partial^2 E_i}{\partial z^2}\right| << \left|k_i \frac{\partial E_i}{\partial z}\right| \tag{3.5}$$

where i indicates the pump, signal, or idler, λ is the corresponding wavelength, and k is the wave vector:

$$k = \frac{2 \cdot \pi \cdot n_i}{\lambda}. \tag{3.6}$$

This approximation assumes that the transfer of energy between the waves is negligable over distances much shorter than the wavelength for pulses down to the 100 fs regime. Applying the infinite plane wave approximation, the slowly varying amplitude approximation, and assuming undeleted pump energy, the coupled amplitude equations become [6]:

$$\frac{\partial}{\partial z} E_{signal} = i \cdot \left(\frac{2\pi k_{signal}}{n^2_{signal}}\right) \cdot d_{eff} \cdot E_{pump}(z) \cdot E^*_{idler}(z) \cdot e^{i\Delta k z} \tag{3.7}$$

$$\frac{\partial}{\partial z}E_{idler} = i \cdot \left(\frac{2\pi k_{idler}}{n^2_{idler}}\right) \cdot d_{eff} \cdot E_{pump}(z) \cdot E^*_{signal}(z) \cdot e^{i\Delta kz} \tag{3.8}$$

$$\frac{\partial}{\partial z}E_{pump} = i \cdot \left(\frac{2\pi k_{pump}}{n^2_{pump}}\right) \cdot d_{eff} \cdot E_{signal}(z) \cdot E^*_{idler}(z) \cdot e^{i\Delta kz} \tag{3.9}$$

Where d_{eff} is the relative nonlinear coefficient of the material, and Δk is the phase mismatch between waveforms given by

$$\Delta k = k_{pump} - k_{signal} - k_{idler}. \tag{3.10}$$

The frequencies of the pump, signal, and idler waveforms follow a relationship dictated by the conservation of energy stated as

$$\omega_{pump} = \omega_{signal} + \omega_{idler} \tag{3.11}$$

Under normal conditions when the phases are not matched ($\Delta k \neq 0$) the exponential terms at the end of the coupled-amplitude equations oscillate, resulting in a sinusoidal transfer of energy back and forth between the pump and the signal/idler beams. But under phase matched conditions ($\Delta k = 0$), the exponent goes to zero and the oscillatory nature is replaced by a constant transfer of energy form the pump to the signal and idler. These relationships are shown in figure 3.3 along side the quasi-phase matching case to be discussed in the next section.

The OPO gained utility in the late 1980's and early 1990's as a tunable pump-probe devise capable of generating synchronized pulses at multiple wavelengths; a significant capability for investigating the relative rates of transition and decay of non-degenerate energy levels in optically excited materials. OPOs can be singly resonant, where only the signal beam is resonated in the optical cavity, doubly resonant where both the signal and the idler are resonated, or

even triply resonant, which are tuned for the pump, signal, and idler beams. Singly resonant systems are most common due to the complexities of stabilization and tuning inherent to doubly and triply resonant cavities, but the latter two offer increased efficiencies and reduced threshold powers. Pulsed OPOs require synchronous pumping often through the use of a mode-locked laser. The pump and signal pulses (and idler in doubly resonant systems) must travel overlapped in space and time through the nonlinear crystal. This requires the OPO round trip frequency or free spectral range to match the pulse repetition rate of the laser. The round trip frequency is inversely proportional to cavity length and is given by:

$$\Delta\nu = \frac{c}{2L} = \frac{c}{P} \tag{3.12}$$

where c is the speed of light, and 2L and P represent the round trip optical path length of the cavity for Fabry Perot and ring cavities. The signal gain achieved with parametric amplification is dependent on pump intensity and the effective length of the gain medium. The total gain is proportional to $g_o L$, where g_o is gain per unit distance and L is length of the gain medium. Using an optical cavity allows the signal to regenerativly build-up, increasing the effective gain of the process. Thus optical cavities are used to increase the gain of parametric amplification in the form optical parametric oscillators which are constructed of a nonlinear medium housed within an optical resonator as shown in figure 3.2. The parametric gain is sensitive to the relative phases of the waves involved and is maximized when the phase matching condition is met or when $\Delta k = 0$.

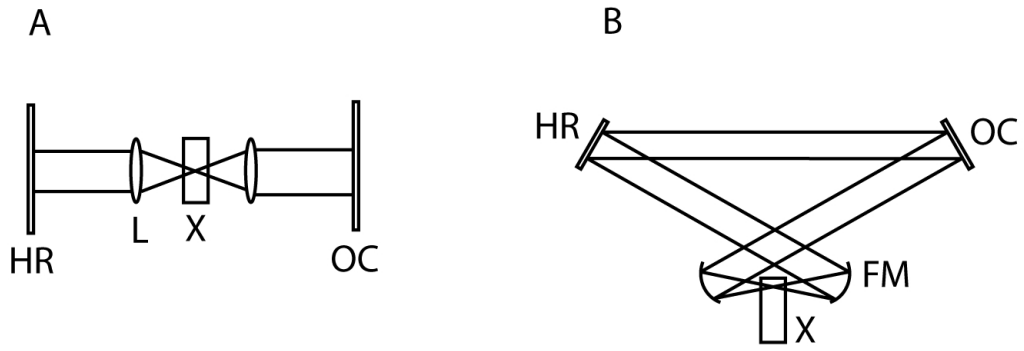

Figure 3.2: Block diagrams showing conceptual resonator configurations for OPOs. A: fabry perot cavity, B: ring cavity.

3.2.1 Quasi-Phase-Matching

The use of birefringent materials is the most common way to achieve phase matching. Birefringence is found in materials with directionally dependent differences in atomic bond properties resulting in directional variations of refractive index with polarization. With careful alignment, beams of varying frequency can be phase-matched. Since $n(\omega)$ increases with frequency, it is necessary that the highest frequency wave be polarized in the plane of lesser index. Tight control of all three refractive indices $n(\omega 1), n(\omega 2)$ and $n(\omega 3)$ is necessary to achieve phase-matching.

Quasi-phase matching is a technique used in nonlinear optics to align phases using periodically poled mediums, or in other words, mediums with a spatially modulated nonlinear susceptibility. In this type of phase matching, the sign of the susceptibility changes just as the nonlinear gain is about to become loss which takes place when the interacting beams become 180 degrees out of phase or every coherence length. First proposed in 1962 [7], quasi-phase matching was not very prevalent until the early 1990s when advances in lithography and

polling techniques made micrometer-scale fabrication practical. The period chosen for the poling is dependent on the coherence length of the interacting waves [8]:

$$l_c = \frac{\lambda}{4(n_2 - n_1)} \tag{3.13}$$

where i_c is the distance required for π phase mismatch to accumulate, lambda is the pump or fundamental vacuum wavelength, and n represents the associated index. The transfer of power between the waves is dependent on the relative phase so that the direction of power flow oscillates with constructive and destructive interference. The proper choice of periodic polling period results in positive gain for the signal from the pump as the waves propagate. A diagram illustrating the growth of the signal with respect to polling period is shown in figure 3.3 where the growth produced with birefringent phase matching, and the oscilating signal intensity associated with no phase match are also shown. You can see from the graph that QFM is less efficient than the ideal birefringent case given the same nonlinear coefficient. The d_{eff} value is reduced by a factor of $2/\pi$ from the ideal case, assuming a 50/50 polling cycle that is perfectly matched to the coherence length of the interacting waves. But achieving critical phase matching usually requires tight control of the operating parameters making it impractical at some wavelengths, hence even with this across-the-board reduction in efficiency, QPM offers great utility and flexibility often making it the more efficient choice for certain applications.

Quasi-Phase-Matching Advantages

Quasi-phase matching offers several advantages over birefringent methods. It provides to ability to engineer the periodicity of the polling thereby improv-

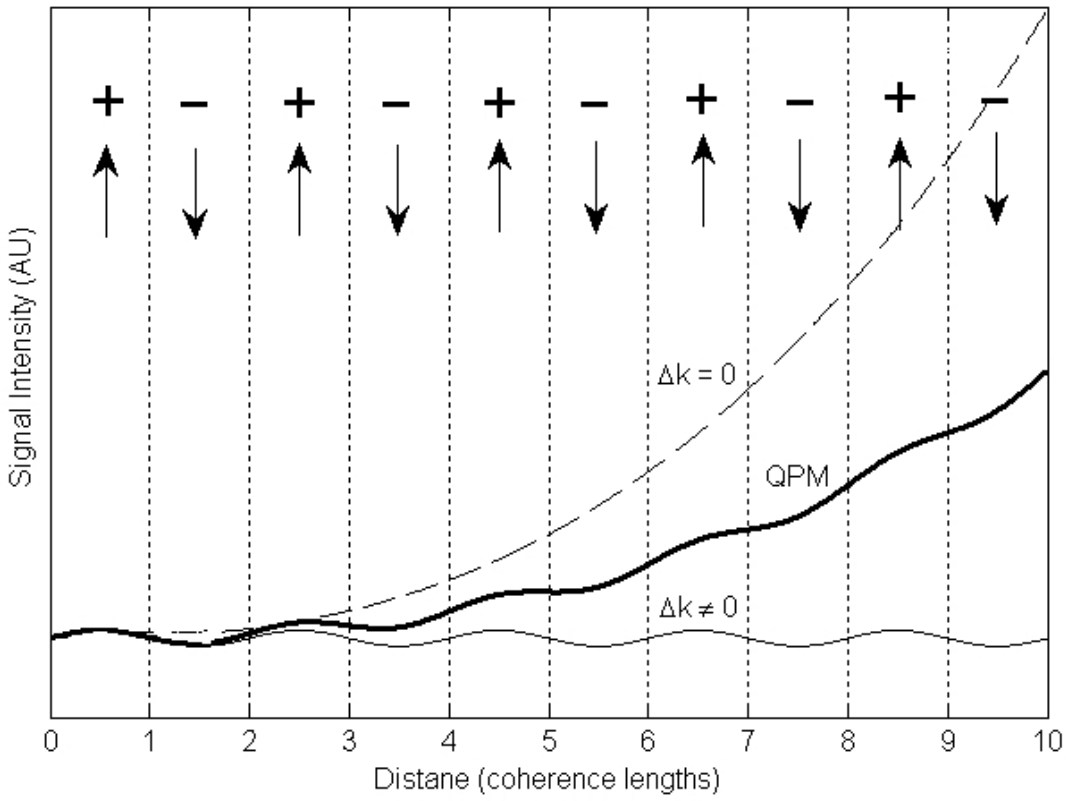

Figure 3.3: Signal intensity growth under different phase matching schemes; birefringent phase matching (dotted line), QPM (thick line), and without phase matching (thin line). The arrows indicate the poling sign of the nonlinear coefficent.

ing efficiency at certain wavelengths and by providing access to nonlinearly generated wavelengths not achievable in current homogeneous mediums. This ability to design the phase-matching properties of a given material expands the materials range of applications, providing more utility to device manufactures. In addition, the period can be optimized for generation of a specific wavelength range for a given operational temperature, reducing the complexity of temperature control systems. Recently, it has become common for a range of polling periods to be incorporated into a single crystal so that simple translation of the

medium within the beam utilizes a new period with access to expanded wavelength tunability.

Collinear quasi-phase matching can also eliminate the inefficiencies caused by spatial walk-off. Spatial walk-off or Poynting vector walk-off occurs in birefringent materials and thus in critical phase matching and is defined as the drift of a beams intensity away from its wave vector. The walk-off is caused by the anisotropic nature of the crystal and the strong angular dependence of the index of refraction. At propagation angles other than 0 or 90 degrees from the optical axis, the Poynting vector (S) and a propagation vector (k) diverge as they propagate [3]. As a consequence, the interaction length between two parallel waves of varying polarization becomes limited as the beam intensities separate. Spatial walk-off can be removed with QPM on-axis beam propagation, increasing the interaction length within the medium.

Another very powerful advantage to Quasi-phase matching is the large nonlinear coefficients that are available when all the interacting waves share the same polarization. Even though QPM suffers from a $2/\pi$ reduction in effective nonlinearity compared to birefringent phase-matching, the access to much stronger constituents of the nonlinear tensor can result in much higher conversion efficiencies.

Quasi-Phase-Matching Implimentation

QPM is achieved by reversing the sign of the materials nonlinear susceptibility every coherence length reinforcing the transfer of energy from the pump to the signal and idler. A periodically polled grating is introduced into the crystal

with the following period [9, 5, 10]:

$$\Lambda = 2 \cdot m \cdot l_c \tag{3.14}$$

where m is the grating order and l_c is the coherence length. In order for perfect phase-matching to occur Δk must be equal to zero, but when all the interacting beams are of the same polarization, the wave vector of the pump is longer than the sum of the signal and idler, assuming a normally dispersive medium ($n_{pump} > n_{signal} + n_{idler}$). This mismatch can be corrected with the additional wave vector that is produced by beams propagation through the periodic crystal structure, where the wave vector of the mth order is given by

$$k_{QPM} = \frac{2 \cdot \pi}{\Lambda} \tag{3.15}$$

A value of unity for the grating order (m=1) corresponds to a 50/50 duty cycle and is the most efficient configuration for QPM operation. The grating wave vector is used in QPM to make up the difference in phase between the interacting beams as can be seen in figure 3.4. Noncollinear pulsed OPOs are subject to both temporal and spatial pulse walk-off where the temporal separation is a byproduct of group-velocity mismatch and the spatial separation comes from the noncollinear configuration. These reduce the effective interaction length of the beams limiting the systems total gain and must be addressed when choosing a cavity configuration. These considerations, and how they influenced the design of our system, are discussed in more detail in section 4.1.

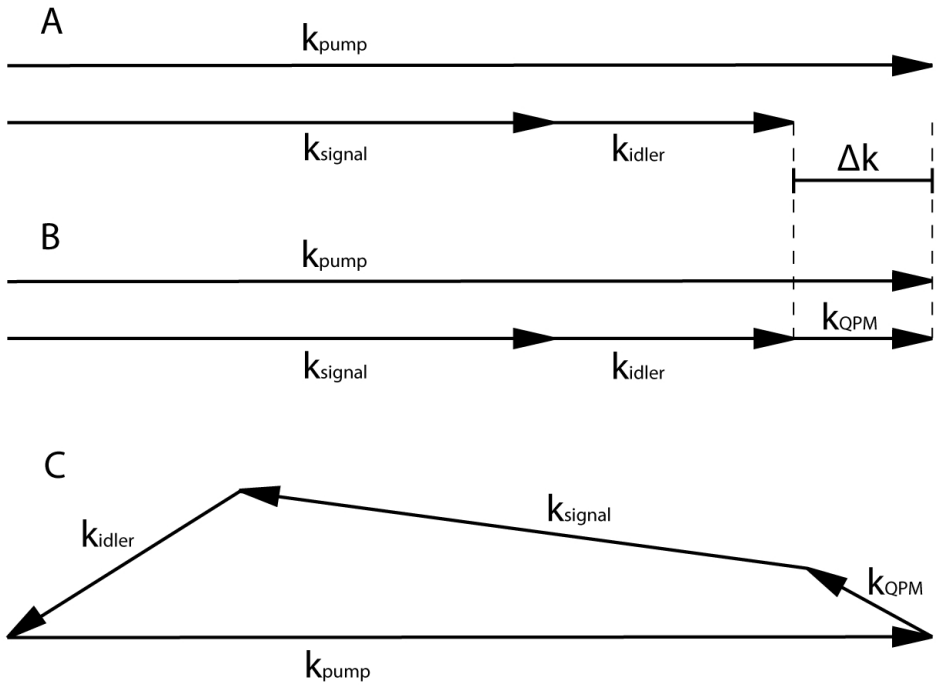

Figure 3.4: Vector representation of QPM showing momentum conservation. Part A represents the phase mismatch (Δk) caused by dispersion, Part B shows how the QPM wave vector can make up the difference in a collinear geometry, Part C shows QPM in the non-collinear case.

BIBLIOGRAPHY

[1] R. Trebino. *Frequency-Resolved Optical Gating: The Measurement of Ultrashort Laser Pulses*. Kluwer Academic Publishers, Norwell Massachesetts, 2002.

[2] J. Hebling, X. P. Zhang, H. Giessen, J. Kuhl, and J. Seres. Pulse characteristics of an optical parametric oscillator pumped by sub-30-fs light pulses. *Opt. Lett.*, 25(14):1055–1057, Jul 2000.

[3] R. W. Boyd. *Nonlinear Optics, Third Edition*. Academic Press, Burlington Massachesetts, 2008.

[4] J. Y. Zhang, J. Y. Huang, Y. R. Shen, and C. Chen. Optical parametric generation and amplification in barium borate and lithium triborate crystals. *J. Opt. Soc. Am. B*, 10(9):1758–1764, Sep 1993.

[5] K. C. Burr. *Mid-Infrared Femtosecond Optical Parametric Oscillators and Their Application to the Study of Ultrafast Hole Dynamics in GaAs*. PhD thesis, Cornell University, Ithaca, NY, 1999.

[6] C.L Tang and L.K Cheng. *Fundamentals of Optical Parametric Processes and Oscillators*. Hardwood Academic Publishers, Amsterdam, 1995.

[7] J. A. Armstrong, N. Bloembergen, J. Ducuing, and P. S. Pershan. Interactions between light waves in a nonlinear dielectric. *Phys. Rev.*, 127(6):1918–1939, Sep 1962.

[8] M. Fejer D. Hum. Quasi-phasematching. *Comptes Rendus Physique*, 8(2):180–198, 2007.

[9] R. W. Boyd. *Nonlinear Optics, 2nd Edition*. Academic Press, Burlington Massachesetts, 2003.

[10] T. G.D Alberto. *Measurment System For Ultra-Fast Phenomena Contained in Slow Relaxation Processes*. PhD thesis, Cornell University, Ithaca, NY, 2006.

CHAPTER 4

DUAL WAVELENGTH, TIME RESOLVED SPECTROSCOPY SYSTEM

One of the initial goals of this effort was to establish a tunable femtosecond, dual wavelength, time resolved spectroscopy capability in the lab. The system was build around an 80 fs mode-locked titanium sapphire laser and consists of a frequency stabilized femtosecond infrared OPO, a pulse selection system, and data acquisitions components. This chapter examines the design and configuration of this pump-probe system.

This OPO is based on a design first demonstrated by Burr et al [1, 2]. The PPLN crystals were fabricated by M. M. Fejers group at Stanford University using the electric-field poling technique. The design parameters considered in the construction of the OPO and the experimental set-up used in this dissertation are discussed in this chapter. The cavity configuration, crystal choice, frequency stabilization, and phase matching strategy will be considered in addition to external factors such as pulse selection and data acquisition.

4.1 OPO Cavity Configuration

Linear and ring cavity designs were considered for use is this system as depicted in figure 4.1. A ring cavity geometry was chosen for this OPO and was based on the increased efficiency offered by the synchronously pumped ring design. The disadvantage of this choice deals mostly with the challange of alignment and the lack of the ability to easily bypass the dispersion compen-

sating prism sequence. It is necessary in both geometries to accurately align the cavity with an external laser prior to searching for the weak multi-pass signal used for the extremely sensitive final alignment. Several round trip passes of the external beam should be overlapped before attempted OPO operation. The alignment lasers wavelength must match that of the resonated OPO signal and enter the resonator through the output coupler ensuring the proper alignment of the internal optics.

Linear cavities are resonators where counter propagating waves or pulses reflect back and forth between end mirrors. They are easier to align and optimize than rings due the increased simplicity of using an external alignment laser and the fact that the prisms can be added after initial operation is achieved. Figure 4.1 compares the two geometries where the prisms are araanged at brewser's angles. The prisms in the linear geometry are easily added or re-

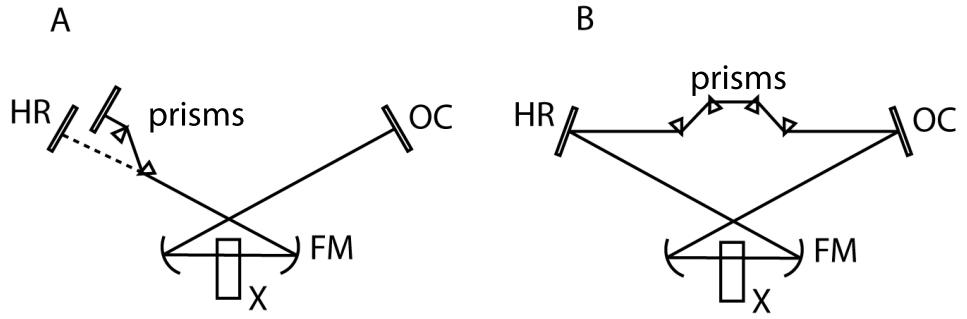

Figure 4.1: Comparison of linear (A) and ring (B) cavity geometries including prism placement. The prisms can be easily added or removed in the linear configuration simply by translating the first prism in or out of the beam.

moved from the cavity by translating the first prism in or out of the beam. A ring cavity contains no end mirrors and allows one way round trip propagation of the pulse. This is advantageous in pulsed OPO operation where the

pump and signal pulses are synchronized to pass through the gain medium overlapped in space and time. The advantage is that in a ring cavity the signal only passes through the dispersive material once per round trip allowing for amplification on each pass through the crystal while two passes are required in the linear configuration. This reduces group velocity dispersion GVD and decreases parasitic losses from SHG inflicted as the pulse travels back through the nonlinear crystal. The ring geometry was chosen for this OPO based on its increased efficiencies and reduced GVD.

The pump and signal pulses are synchronized within the OPO to the pulse repetition rate of the pump laser. The pulse repetition rate of the Ti:Sapphire pump was approximately 80.6 MHz which dictated that the round trip optical path length of the OPO resonator be near 3716 mm. The relationship between cavity length and pulse repetition rate is shown in figure 4.2. The high reflective mirror as shown in figure 4.3 was mounted on a translational stage for fine tuning of the cavity length. Minor adjustments of cavity length can be used to controll the wavelength of the OPO output provided that the pulses remain overlapped and synchronized. In the final configuration, the pump beam enters the cavity at the PPLN crystal then leaves the resonator, as does the idler, while the signal beam exits the crystal at the precise angle required to circulate in the cavity. The non-collinear pumping geometry is given in figure 4.4.

4.2 Phase-matching Method

QPM was chosen over birerefringent phase matching for use in this OPO. This choice was based on two advantages; QPM can utilize higher nonlinear coefficients which are not available for birefringent phase matching, and periodi-

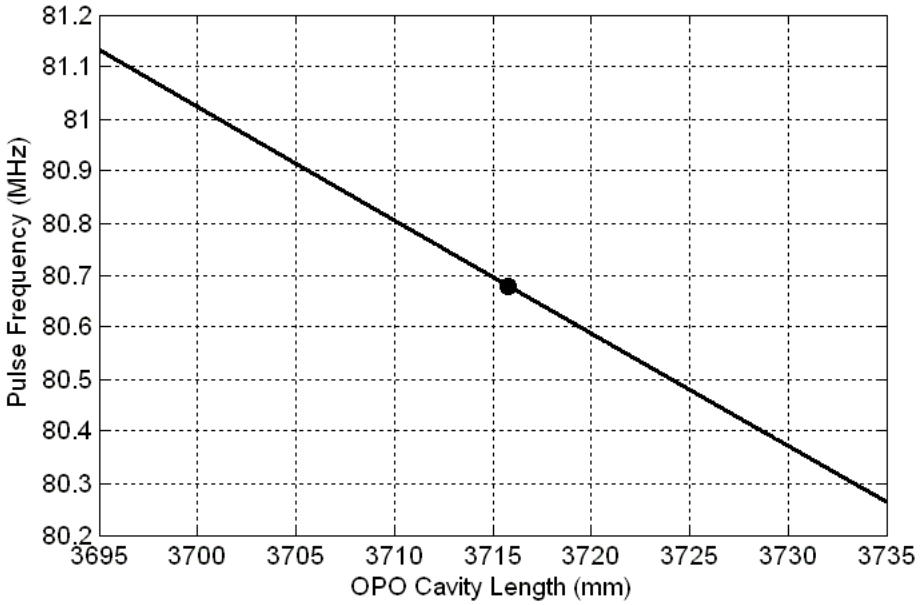

Figure 4.2: Plot showing the relationship between cavity length and pulse repetition rate. The cavity length of the OPO is 3716 mm corresponding to a pulse repetition rate of 80.67 MHz.

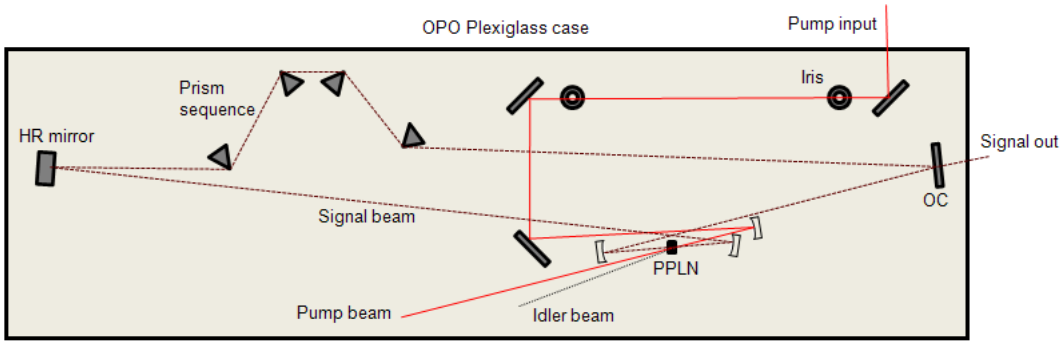

Figure 4.3: Block diagram of the noncollinear, singly resonant, femtosecond PPLN OPO.

cally poled materials can be engineered to specific phase matching requirements while the phase matching characteristics of birefringent materials are fixed and restrictive. QPM also has the advantage of avoiding the problem of walk-off when used in a collinear geometry allowing for longer interaction lengths but a

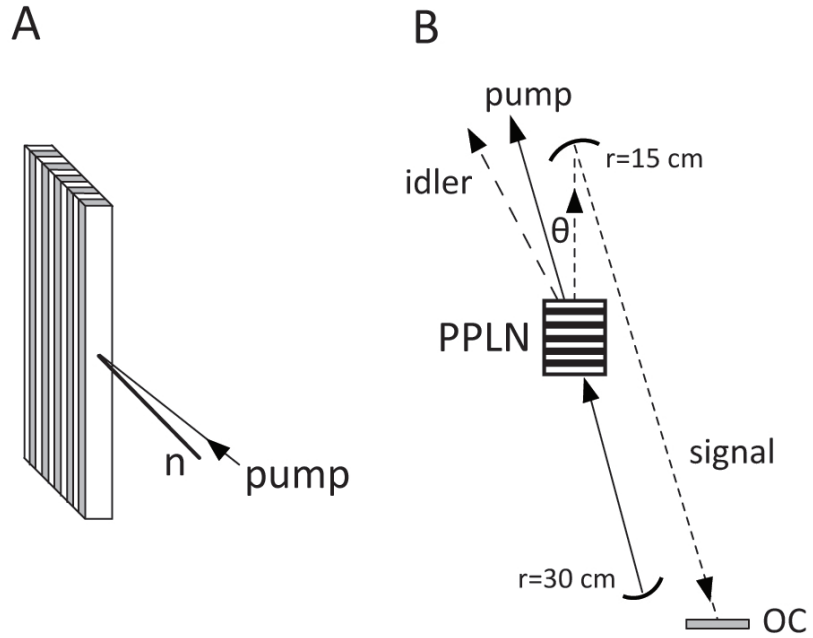

Figure 4.4: Noncollinear pumping geometry. A shows the crystal orientation with respect to pump beam and surface normal, while B represents the beam and optics configuration where θ is the Noncollinear angle measured external to the crystal ($\theta \approx 2.5$ degrees in this design).

non-collinear geometry was chosen for this design to the sacrifice of this benefit, because of the expensive custom optics that were required to pass the signal and filter the pump.

As stated earlier, birerefringent phase matching at $\Delta k = 0$, possess a higher effective nonlinear coefficient than does QPM given the same material nonlinear coefficient. This would be a severe set-back to the use of QPM if it were not for QPMs access to higher nonlinear coefficients. The nonlinear optical coefficients for $LiNbO_3$ are shown in table 4.1. Birefringent methods require the use of birefringent materials and that the polarizations of the interacting beams are orthogonal. These are not requirements of QPM which permits all the interacting beams to be of the same polarization, allowing access to larger nonlinear

Designation	D_{22}	D_{31}	D_{33}
Nonlinear Coefficient	2.1 pm/V	4.3 pm/V	27 pm/V

Table 4.1: Measured values of the nonlinear coefficients of $LiNbO_3$

.

coefficients. Recall that the d_{eff} value is reduced by a factor of $2/\pi$ assuming a 50/50 polling cycle which limits its application to materials with significantly higher d_{33} values. The three of the most common periodically polled materials are $LiNbO_3$, KTP, and SLT, but many ferroelectric nonlinear crystals have their largest optical nonlinear coefficient inaccessible to birefringent phase-matching and thus may benefit from QPM techniques. The choice of PPLN for use in this OPO gave us access to $LiNbO_3$'s D_{33} coefficient at 27 pm/V. Looking again at table 4.1 it can be seen that even with the $2/\pi$ factor reduction, the resultant 17.2 pm/V is much higher than the other available coefficients.

4.2.1 Engineering the Periodically Poled Crystal

One significant advantage that periodically-poled materials have over conventional nonlinear crystals is the ability to engineer the phase-matching condition. The poling periods can be designed to provide QPM for any nonlinear interaction supported by the transparency range of the material.

Birefringent materials are limited in their range of interactions by their reliance on direction and polarization dependent refractive indices. The drawbacks of birefringent phase-matching include the limited amount of suitable

materials, the fixed nature of the index ratios, and the meager range of wavelengths that can be matched for a given crystal. Although excellent efficiencies can be found through critically phase-matched birefringent crystals, the versatility of periodically poled materials make many otherwise unrealizable yet useful frequency conversions possible.

New designs of periodically poled structures have recently included chirped gratings for pulse compression or expansion [3, 4], variable periods within a crystal for tunability (see section 4.3.1), quasi periodic structures for the simultaneous operation of two three-wave-mixing processes [5], periodically poled $LiNbO_3$ waveguides [6], and two-dimensional gratings for increased efficiencies and multidirectional operation [7, 8, 9]. Periodically poled materials have recently made nonlinear frequency conversions with relatively weak semiconductor diode lasers possible. This has helped move nonlinear optics from the lab into commercial markets. Currently PPLN crystals are being considered for use in the next evolution of screens, projectors, and heads-up-displays for commercial and military applications, all based on nonlinear and laser technologies.

The fabrication of periodically poled crystals like $LiNbO_3$ is based on the electric dipole moment found in ferroelectric materials. The spatial orientation of the niobium and lithium ions within the unit cell is responsible for the direction of the electric dipole produced by the cell. Extremely high electric fields of approximately 21-23 kV/mm can invert the crystal arrangement and realign the electric dipole direction. The use of strong electric fields to induce poling is currently the most utilized method of fabrication among less common techniques that rely on the modulation of crystal growth parameters [10, 11, 12] or through the periodic implantation of impurities [13].

The periodically poled $LiNbO_3$ crystal used in this OPO was made using a

21 kV/mm electric field applied for 50 ms through the crystal by lithographically applied aluminum electrodes [14]. The crystal was annealed at 120 C for one hour to relieve strain and the end faces were polished. A single layer quarter wave stack of SiO_2 (n=1.46) was applied as an antireflective coating with the peak transmission centered near 1 μm. The particular crystal used here measured approximately 0.5 mm by 10 mm with a beam propagation dimension of 420 μm across. A 19.5 μm poling period was written in several sections of the crystal spanning the length of the longest dimension (15 mm). A picture of the crystal orientation and dimensions is shown in figure 4.5.

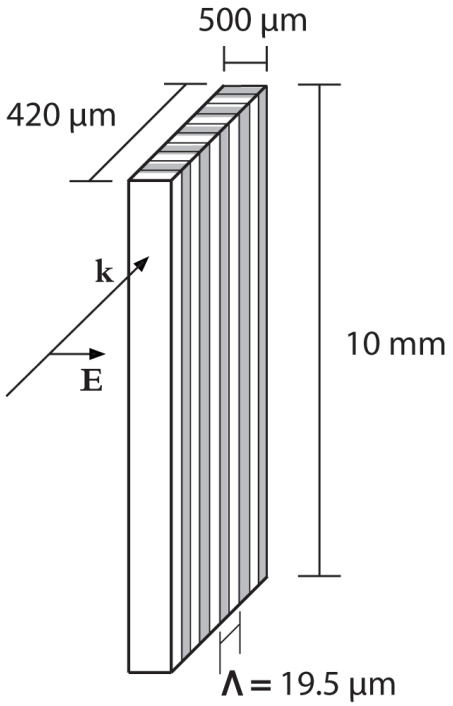

Figure 4.5: Dimensions of the PPLN crystal and the poling orientation with respect to beam path and polarization. The input beam is e-polarized and the stripes represent alternating poling directions. Not to scale.

4.3 Wavelength Tuning the OPO

One of the benefits of an OPO is the ability to tune the output wavelength. An OPO is commonly tuned through any of five techniques, changing the periodicity of the crystal, temperature tuning, pump wavelength tuning, cavity length tuning, and by varying the crystal and pump angle. The two most effective and easy methods employed when operating this OPO are pump wavelength tuning and OPO cavity length tuning. The tuning efficiency of this system is limited by the bandwidth of the cavity mirrors with an approximate signal range of 1040-1150 nm . Detailed aspects of tuning methods and the range limitations associated with this design are given in previous Cornell dissertations [15, 2] and will only be briefly addressed hear for convenience.

4.3.1 Tuning Through Variable Periodic Poling

As stated previously, the grating wavevector is a function of poling period ($\Delta K = 1\pi m/\Lambda$) and can make up the momentum difference in QPM. Thus one way to tune an OPO is by changing the period. A crystal length of 420 μm was used in this configuration with a fixed period of 19.5 μm. Given an external noncollinear angle of 2.5°, a pump wavelength of 780 nm, and a crystal temperature of 150 C, this period is optimized for an output wavelength near 1100 nm [16]. But it has become common for OPOs to utilize variable poling periods within a single crystal providing the means widely tune operation simply by translating the crystal [17, 18]. This tuning method is typically based on multiple parallel gratings or with fanned gratings as seen in figure 4.6.

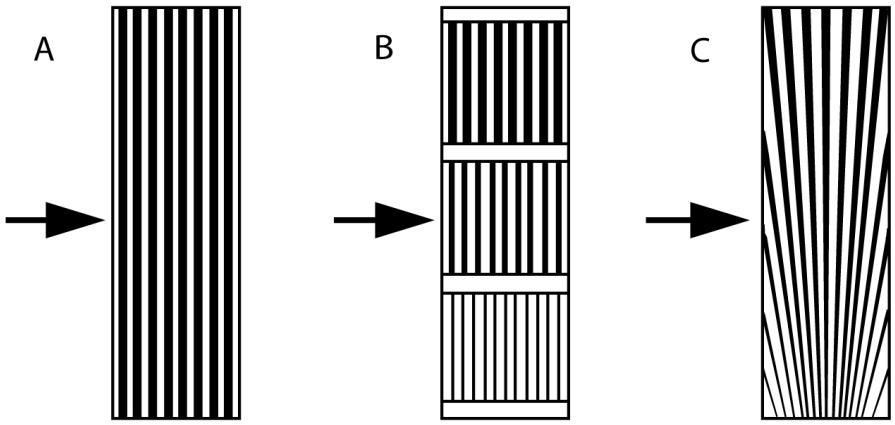

Figure 4.6: Periodic poling techniques, where A represents one period per crystal (similar to that used in this work), B has three poling periods, and C is a continuously tunable (fan-poling).

4.3.2 Crystal Temperature Tuning

Crystal temperature tuning works in a similar way to period tuning in that temperature induced changes in the refractive index and thermal expansion alter the periodicity. The relationship between temperature and index is readily modeled using the temperature dependent Sellmeier equations [19]. The change in periodicity is given by ($\Delta\Lambda = \alpha \cdot \Delta T$) where α is the coefficient of thermal expansion. Lithium niobates coefficient is equal to 1.54 x 10^{-5} resulting in a period range of +/- 30 nm over a 200 C shift. The change in period is reflected in the output providing an efficient way to tune the OPO although significant temperature swings are needed to tune over wide ranges.

4.3.3 Pump Wavelength Tuning

Adjusting the pump wavelength and thus its wavevector is an easy method of tuning the OPO and is often sufficient for many tuning requirements. Changes in the pump wavevector affect both the signal and idler wavelengths and serve as a convenient adjustment given a broadly tunable pump source like the Ti:sapphire laser. This method was used in conjunction with crystal temperature tuning and cavity length tuning to reach the desired pump and probe wavelengths used in experimental testing.

4.3.4 Cavity Length Tuninig

Cavity length tuning of the output wavelength is a convenient and highly effective method that does not require any addition alterations to the resonator or pump configurations. Simply changing the cavity length while holding the crystal period (19.5 μm), pump wavelength (780-820 nm), crystal angle (2.5 $^\circ$), and crystal temp (100-120 C) constant was an efficient way of tuning the OPO. Tuning ranges on the order of 150 nm were attainable depending on the center wavelength and was limited by the output coupler bandwidth [Burr] More typical ranges near 100 nm were common. Pulse overlap within the crystal is also affected by cavity length changes where a translation of 300 nm corresponds to only 1 fs of delay or only about 1.1 % FWHM.

The technique is based on the effects of cavity length detuning where changes in cavity length result in decreased signal gain as the synchronization between pump and signal pulses is reduced. In an attempt to maintain stability, the signal wavelength shifts towards a value that has the correct group

velocity to support the new optical path length of the resonator. The amount the wavelength shifts is dependent on dispersive nature of the crystal and its length, where the change in optical path length through the crystal is simply the product of index and length ($\Delta OPL = \Delta n \cdot L_{xtl}$). A dispersion curve showing lithium niobates (the nonlinear crystal in this OPO) refractive index for the extrordinary ray path as a function of wavelength is shown in figure 4.7 and was calculated using Sellmeier coefficients from published literature [20, 21]. The first demonstration of broad tunability using cavity length tuning in a fem-

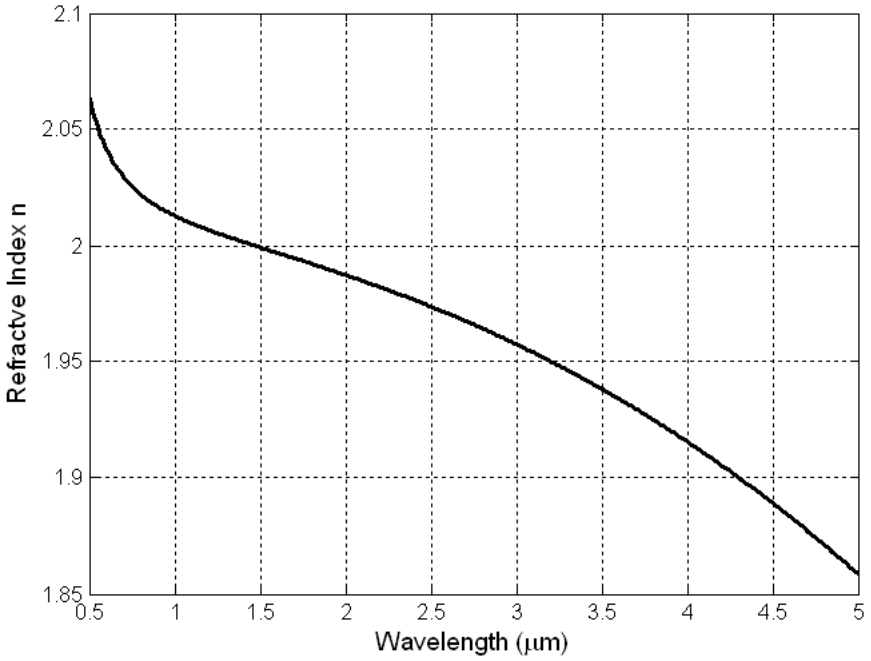

Figure 4.7: Dispersion curve showing the refractive index for the extraordinary ray (e) in $LiNbO_3$ as a function of wavelength. The e axis of the crystal corresponds to signal path of the PPLN OPO.

tosecond OPO was in 1989 [22] and since then the utility of such designs have been well established [23, 24, 25].

4.3.5 Crystal Angle Tuning

Tuning can also be achieved by rotating the crystal angle between the poled grating and the pump beam [26]. The resulting change in QPM wavevector effects changes in the signal and idler wavelengths with the pump held constant. This method was not used for tuning during any of the work covered in this dissertation due to the complexities of maintaining stability with angle adjustment in a non-collinear geometry. The crystal angle was held constant at approximately 2.5 deg as measured internal to the crystal. Major alteration of the crystal angle reduces efficiency an may result in loss of operation or the need for cavity realignment.

4.4 Frequency stabilization of the OPO

While previous stabilization methods for femtosecond OPO's have monitored fluctuations in the spectral envelope through direct measurement of the signal's center wavelength [27, 28], our system utilizes the visible second harmonic of the signal beam that naturally escapes the resonator. Higher order quasi-phase matching in the OPO produces a strong presence of visible wavelengths from the PPLN crystal through SHG and SFG. The active frequency stabilization scheme employed for this OPO monitors the signal SHG for fluctuations in its center wavelength and adjusts the cavity length to compensate. A feedback loop is used to adjust the OPO resonant cavity length by varying the voltage on a piezoelectric transducer on the HR mirror. A block diagram of the system is given in figure 4.8.

The signal SHG is diverted from the OPO resonant cavity as it passes

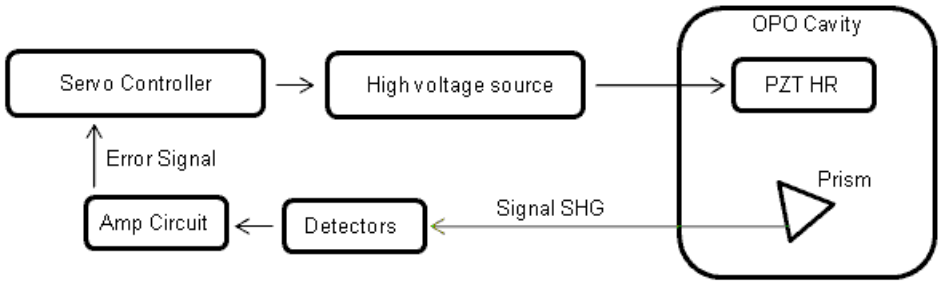

Figure 4.8: OPO frequency stabilization system. The signal SHG is monitored for frequency fluctuations and the resulting error signal is used to stabilize the signal frequency through cavity length changes via a piezoelectric transducer on the high reflective mirror.

through the intracavity dispersion compensating prisms and onto a pair balanced photodiodes (FDS100 Si photodiodes). As the signal wavelength varies, so does its SHG wavelength, and thus the angle it exits the prism, resulting in a translation of the spot on the balanced detector. As the spot walks, an error signal is generated in a feedback loop with a corresponding voltage change on the transducer, effectively modifying the cavity length and correcting the error. A balanced detector/amplifier was constructed as the feedback curcuit to sense the power fluctuations between two photodiodes as depicted in figure 4.9. No error signal is produced when the photodiodes receive equal amounts of radiation. A switchable inverter allows the phase of the error signal to be flipped by 180 degrees effectively suppressing runaway oscillations due to positive reinforcement and a 50 kΩ potentiometer was used to control the gain of the circuit. The output of the circuit was conditioned through a servo controller before it was sent to the (Burleigh RC-44) high voltage power supply.

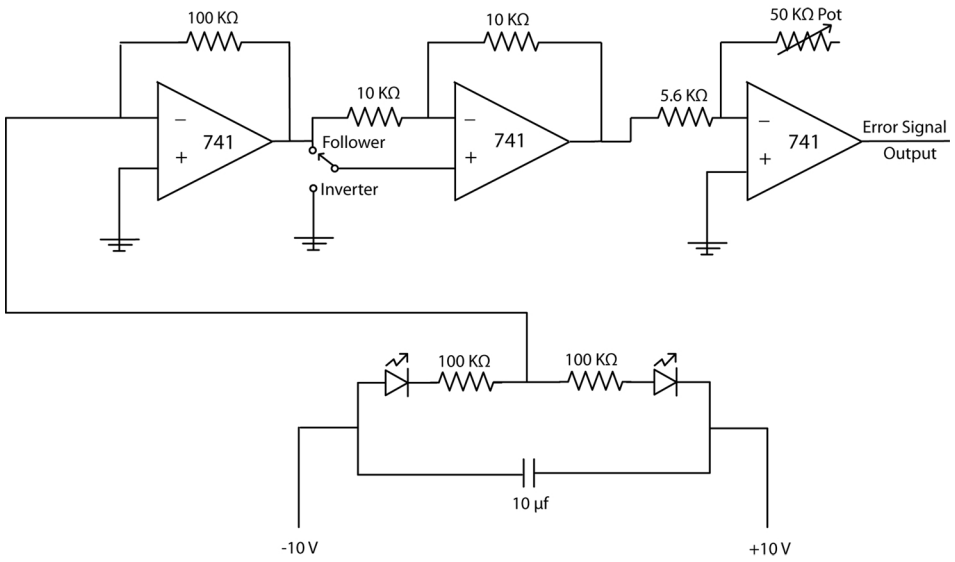

Figure 4.9: Feedback circuit used in the OPO frequency stabilization system.

4.5 Optical Configuration of the Nondegenerate Pump Probe Station

Accurate optical alignment and synchronization of the nondegenerate pump probe system is required for reliable operation. Three main concerns must be addresses to reach functionality; synchronization of the pump and probe pulses, alignment of the spatial modes within the sample, and synchronization of the pulse selection system. The pulse selection system is covered in the next section while the first two are discussed here. The experimental set-up of the non-degenerate pump probe station is depicted in figure 4.10.

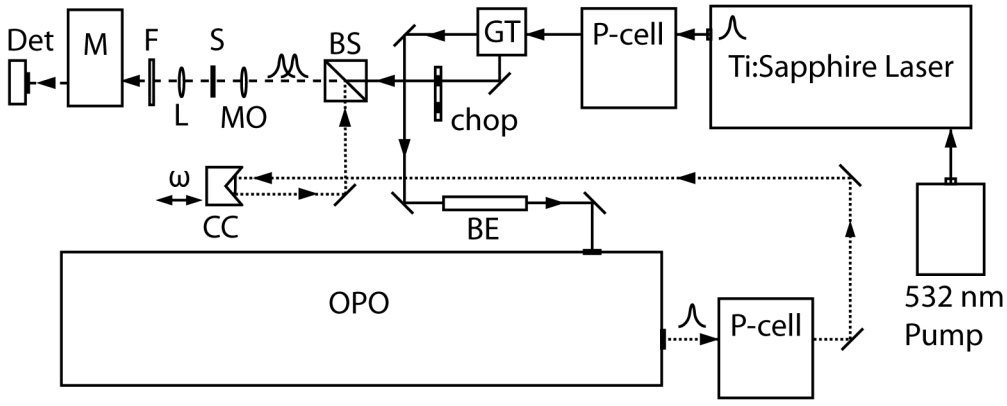

Figure 4.10: Optical configuration of non-degenerate pump probe system. P-cell, Pockels cell; GT, Glan Talylor polarizer; BS, beam splitter; CC, corner cube; BE, beam expander; MO, microscope objective; S, sample; L, lens; M, monochromator; Det, detector. The solid line represents 812 nm, Short dashes represent 1064 nm, and long dahes are the combined beams.

Synchronization of Pump and Probe Signals

The station is designed to continuously probe a sample while monitoring the transmitted probe signal, as pump pulses (at a much lower pulse repetition rate) excite electron transitions within the sample. Pump induced transparency changes at the probe wavelength give information on decay phenomenon within the sample. Figure 4.11 shows an example of the spectrums from the simultaneously generated pump and probe pulse. The pump laser must power the OPO while occasionally supplying a pumping pulse directly to the sample. As the pump pulses exit the laser, they move through a Pockels cell and a Glan Taylor beam splitter (prism) that passes the majority of pulses to the OPO but from time-to-time diverts a single pulse to the sample. The pulse repetition rate of this pulse diversion is controlled by a frequency generator connected to the Pockels cells high voltage power supply with an input range

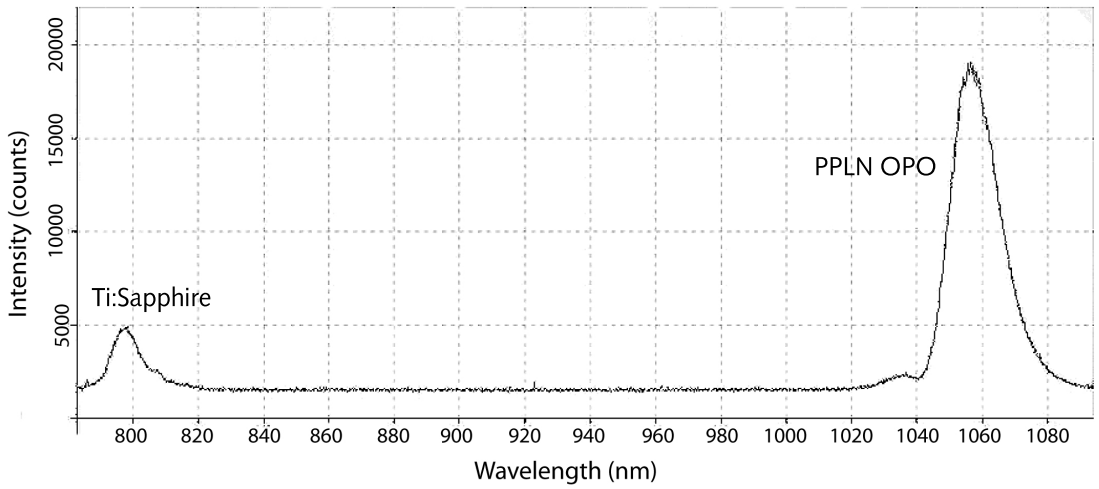

Figure 4.11: The measured spectrums of simultaneously generated pump and probe pulses. The relative intensities are arbitrary.

of 1-5000 Hz. Lets first consider the path of the pulses that power the OPO then return to ones that pump the sample.

The OPO pump beam leaves the Glan Taylor prism and is directed through a beam expander comprised of two 60 cm radius of curvature mirrors used to control the beam properties prior to entering the OPO cavity. The internal design of the OPO was given in figure 4.3 which shows the location of the output coupler (OC). The optical path length from the OC to the beam combiner (labeled BS in figure 4.10) is critical to temporal alignment of the pump and probe pulses and was calculated to be a required 3920 mm. The system is configured so that the total trip from the laser through the OPO and to the beam combiner is equal to two times the cavity length (2 x3716 mm) plus the distance from the pump laser to the beam combiner (700 mm) for a total of 8132 mm. The cavity length mentioned here being that of the laser or OPO, both being equal. This makes certain that a pump pulse reaches the sample at the same time as the probe pulse fired two laser pulses prior. This ensures that any perturbation to

OPO operation from the missing pulse (the one that was diverted to the sample) does not occur until well after the intensity of the probe pulse was recorded after passing through the sample. The pulse repetition rate of the pump laser was measured at 80.67 MHz separating each pulse by 12.4 ns or 3716 mm. The spatially modulated corner cube was mounted on a translational stage for adjustment of the probe path length. The corner cube is mechanically translated back and forth imparting a variable delay on the probe signal. From here the probe beam is recombined with the pump beam both spatially and temporally at the beam combiner.

The pump pulse diverted from the OPO takes a relatively simple path. As seen in the diagram, the diverted beam passes through an optical chopper straight to the beam combiner. The chopper was typically set between 30-200 Hz to be used in conjunction with a lock-in amplifier or phase-sensitive detector. Lock-ins can detect signals down to a few nanovolts and accurate measurements can be made even when signals are obscured by noise many thousands of times larger. Lock-ins only see signals and noise at the reference frequency since the other frequencies are removed by a low pass filter. Thus only changes in the probe intensity with the same phase as the chopped pump are detected.

When properly aligned the pump and probe pulses reach the beam combiner at a temporal separation based on the offset of the corner cube from zero delay. This relationship is given by $\delta t = C \cdot 2D$ where δt is the time delay, C is the speed of light in air, and D is the translated distance, the 2 comes from the bidirectional path of the beam reflecting off the corner cube.

Ensuring Proper Alignment

The pulses were roughly synchronized with the aid of a fast detector (InGaAs, 700-1800 nm, 10 ns rise time) and a 5 GHz oscilloscope, see figure 4.12. The rise and fall times of the detector and the speed of the oscilloscope limit the

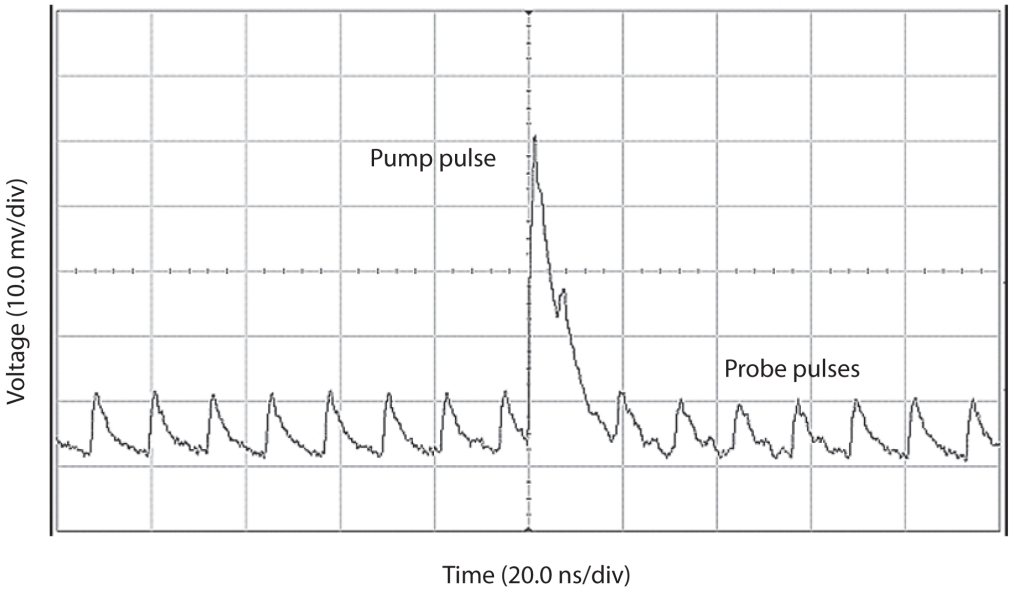

Figure 4.12: Oscilloscope trace of the pump and probe pulses used to roughly synchronize their timing.

resolution of this method so that alignment can only be electronically checked to within a few ns. Since many measurements require accuracies on the order of tens or hundreds of fs, an optical method of synchronization was required.

The station was checked for proper alignment by substituting a PPLN crystal in place of the sample. With the pump centered at 808 nm and the probe centered at 1064 nm, we planned to maximized SFG where $\hbar\omega_{SFG} = \hbar\omega_{pump} + \hbar\omega_{probe}$ or or alternately as

$$\lambda_{SFG} = \lambda_{pump}\frac{\lambda_{probe}}{\lambda_{pump} + \lambda_{probe}} \tag{4.1}$$

giving the expected SFG value of approximately 460 nm. An example of the wavelengths generated in this nonlinear process is shown in figure 4.3, where the SFG is extremely sensitive to timing and alignment providing the ideal method for system optimization. This process was not only useful for align-

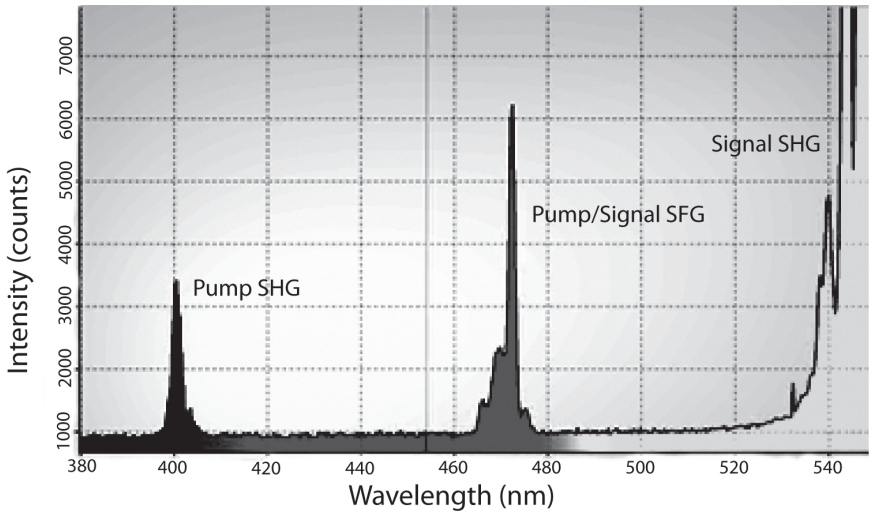

Figure 4.13: Measued spectrums of the nonlinear interactions used to align the sample and synchronize the pulses. A PPLN crystal was used in place of the sample to generate these signals.

ing the pulses in space and time but also for centering the pump and probe spectrums on the absorption band and probing wavelengths respectively. After alignment, the PPLN crystal was replaced by the sample for testing.

4.6 Pulse Selection System

It is often necessary to control the pulse repetition rates of the pump and/or the probing signals in time resolved spectroscopy experimentation. Pulse gating systems are ideal for such systems with applications in mode-locked laser pulse

picking, regenerative amplifier gating, laser pulse slicing, q-switching, and cavity dumping.

Two pulse selection systems utilizing high voltage Pockels cells were incorporated into the OPO based pump probe configuration as detailed in figure 4.10. One cell was used to pick pump pulses prior to entry into the OPO while the second was used to control the pulse repetition rate of the OPO generated probing pulses. The two systems were synchronized to the pulse repetition rate of the titanium sapphire pump laser by means of a photodiode that monitors the laser output. A diagram showing the synchronization set-up is depicted in figure 4.14. With rise and fall times as short as 3 ns the Pockels cells can easily respond to the fixed 80.6 MHz pulse repetition rate of the Kerr mode-locked pump laser.

Data Acquisition in the Time Resolved Spectroscopy Configuration

Detection of gain in the probe pulse signal immediately following population of the upper lasing level is a challenging problem. The total change of probe pulse energies before and after pumping can be much less than 1 percent due to the limited pulse energy of the pump and from difficulties with the optimization of mode overlap between the pump and probe within the crystal. Gain as low as 1/4 of a percent is likely meaning that the signal will reside well within the noise. Multiple methods of signal detection were employed in the experiment to include spectral filtering, gated detection, lock-in amplification, and time averaging.

The detector was a Thorlabs DET10C (InGaAs Detector) with a responsively from 700-1800 nm and a 10 ns rise time. One version of the detection and sig-

nal processing scheme is given in figuure 4.14. Many subtle variations were made throught the experimentaion such as removing the boxcar or lock-in. A

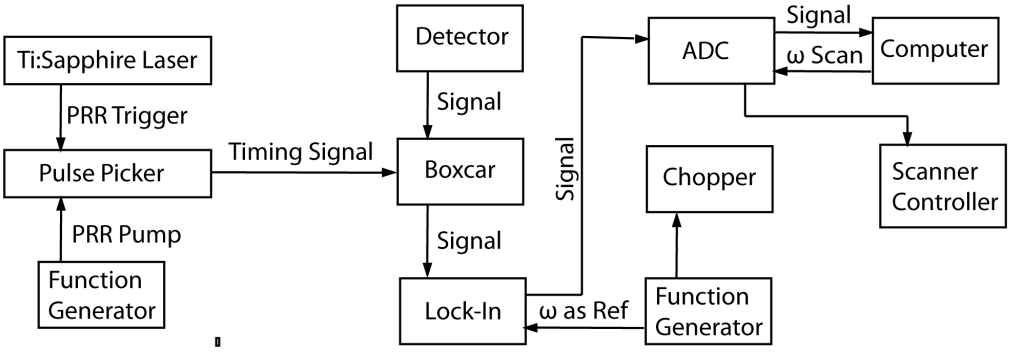

Figure 4.14: Box diagram of a typical signal processing set-up used when trying to locate the pump induced gain in the probe signal.

monochromator was used to ensure that the pump beam centered at 808 nm was spectrally filtered from the 1064 nm probe beam prior to reaching the detector. The filtering was verified when the lock-in did not detect the presence of stray pump light with the monochromator set to pass 1064 nm with the probe beam blocked and the Nd:YAG sample removed. This same configuration was used to verify the presence of 1064 nm fluorescence with the sample in place. The placement of the monochromator in the final experiment set-up is given in figure 4.15.

The raw detector output was connected to a boxcar of a gated detection system that was synchronized to the monitor output on the pump's Lasermetrics pulse selection system which was in turn synchronized to the pump lasers mode locked output. Use of the boxcar integrator allows for gated detection that improves the signal to noise ratio proportional to $\sqrt{N}$ where N is the number of

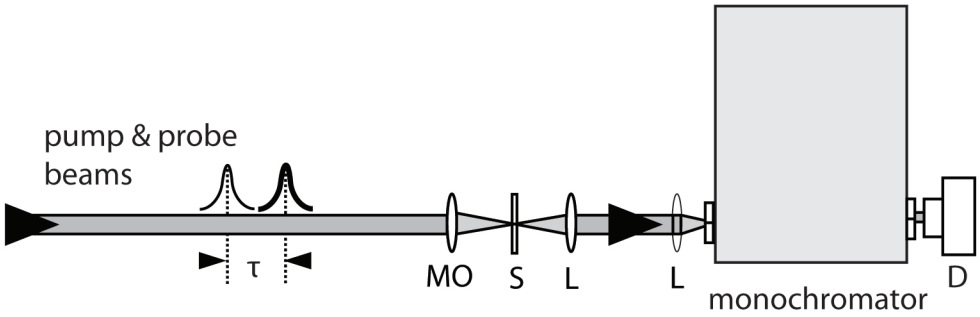

Figure 4.15: Illustration of the monochromator placement in the non-degenerate pump probe set-up. τ is the delay between the collinear pump and probe pulses; MO, microscope objective; S, sample; L, lens; D, detector.

individual measurements.

$$SNR = \frac{V_{signal}}{V_{noise}} = \frac{V_{signal}}{\frac{1}{\sqrt{N}}\sqrt{V_{noise}^2}} \propto \sqrt{N} \tag{4.2}$$

The boxcar is best suited for periodic signals like those taken in pump probe measurements and works by taking measurements only during the times when signatures are present in the data. Figure 4.16 shows a graphical representation of the timing sequence.

A lock-in amplifier or phase-sensitive detector was used to detect and measure very small AC signals down to a few nV. Accurate measurements can be made even when the signal is obscured by noise sources many thousand times larger. The model used in this effort was a Stanford Research SR850 Digital Signal Processor Lock-In amplifier. The DC output signal, which is proportional to phase-matched portion of the input signal amplitude, was sent to a digital-to-analog converter and recorded by a LabView script. The lock-ins reference input was supplied by the frequency generator which also controlled a chopper used to modulate the pump beam.

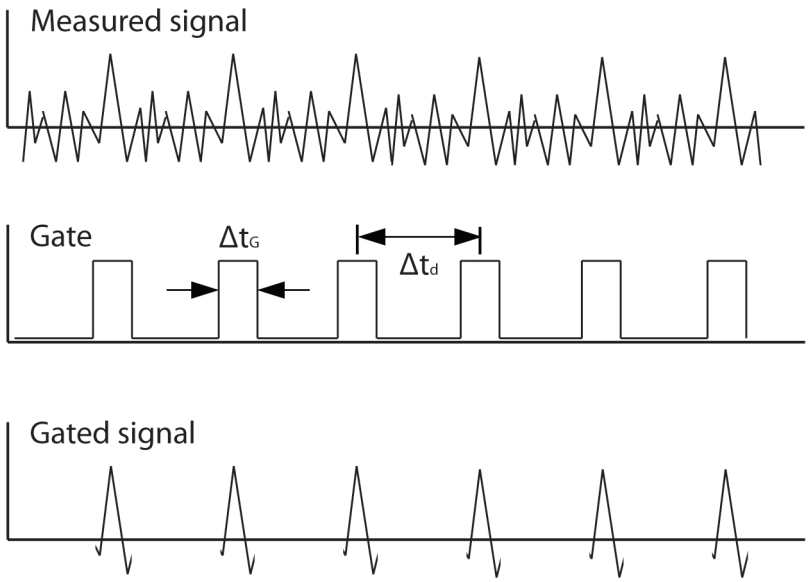

Figure 4.16: Timing sequence of the boxcar integrator. In this experimentation Δt_G was set between 3-10 ns due to the 12 ns delay between probe pulses and Δt_d was synchronized with the pump pulse repetition rate.

BIBLIOGRAPHY

[1] Kent C. Burr, C. L. Tang, Mark A. Arbore, and Martin M. Fejer. Broadly tunable mid-infrared femtosecond optical parametric oscillator using all-solid-state-pumped periodically poled lithium niobate. *Opt. Lett.*, 22(19):1458–1460, Oct 1997.

[2] K. C. Burr. *Mid-Infrared Femtosecond Optical Parametric Oscillators and Their Application to the Study of Ultrafast Hole Dynamics in GaAs*. PhD thesis, Cornell University, Ithaca, NY, 1999.

[3] A. M. Schober, G. Imeshev, and M. M. Fejer. Tunable-chirp pulse compression in quasi-phase-matched second-harmonic generation. *Opt. Lett.*, 27(13):1129–1131, Jul 2002.

[4] M. Fermann. Ultrafast lasers, technology and applications. *US Patent*, (6,275,512), 2001.

[5] Anatolii S Chirkin, V V Volkov, G D Laptev, and E Yu Morozov. Consecutive three-wave interactions in nonlinear optics of periodically inhomogeneous media. *Quantum Electronics*, 30(10):847, 2000.

[6] Yujie J. Ding. Efficient generation of far-infrared radiation from a periodically poled linbo3 waveguide based on surface-emitting geometry. *J. Opt. Soc. Am. B*, 28(5):977–981, May 2011.

[7] P. E.; Missey M. J.; Schepler K. L. Russell, S. M.; Powers. Broadband mid-infrared generation with two-dimensional quasi-phase-matched structures. *Journal of Quantum Electronics*, 37(7):877–887, Jul 2011.

[8] Yuzo Sasaki, Yuri Avetisyan, Hiroyuki Yokoyama, and Hiromasa Ito. Surface-emitted terahertz-wave difference-frequency generation in two-dimensional periodically poled lithium niobate. *Opt. Lett.*, 30(21):2927–2929, Nov 2005.

[9] N. G. R. Broderick, G. W. Ross, H. L. Offerhaus, D. J. Richardson, and D. C. Hanna. Hexagonally poled lithium niobate: A two-dimensional nonlinear photonic crystal. *Phys. Rev. Lett.*, 84(19):4345–4348, May 2000.

[10] Duan Feng, Nai-Ben Ming, Jing-Fen Hong, Yong-Shun Yang, Jin-Song Zhu, Zhen Yang, and Ye-Ning Wang. Enhancement of second-harmonic gener-

ation in linbo[sub 3] crystals with periodic laminar ferroelectric domains. *Applied Physics Letters*, 37(7):607–609, 1980.

[11] A. Feisst and P. Koidl. Current induced periodic ferroelectric domain structures in linbo[sub 3] applied for efficient nonlinear optical frequency mixing. *Applied Physics Letters*, 47(11):1125–1127, 1985.

[12] G. A. Magel, M. M. Fejer, and R. L. Byer. Quasi-phase-matched second-harmonic generation of blue light in periodically poled linbo[sub 3]. *Applied Physics Letters*, 56(2):108–110, 1990.

[13] M. M. Fejer E. J. Lim and R. L. Byer. Electron. *Electron. Lett.*, 25:174, 1989.

[14] L. E. Myers, R. C. Eckardt, M. M. Fejer, R. L. Byer, W. R. Bosenberg, and J. W. Pierce. Quasi-phase-matched optical parametric oscillators in bulk periodically poled linbo3. *J. Opt. Soc. Am. B*, 12(11):2102–2116, Nov 1995.

[15] T. G.D Alberto. *Measurment System For Ultra-Fast Phenomena Contained in Slow Relaxation Processes*. PhD thesis, Cornell University, Ithaca, NY, 2006.

[16] Kent C. Burr, C. L. Tang, Mark A. Arbore, and Martin M. Fejer. High-repetition-rate femtosecond optical parametric oscillator based on periodically poled lithium niobate. *Applied Physics Letters*, 70(25):3341–3343, 1997.

[17] N. Savege. Optical parametric oscillators. *Nature Photonics*, 4:124–125, Apr 1996.

[18] L. E. Myers, R. C. Eckardt, M. M. Fejer, R. L. Byer, and W. R. Bosenberg. Multigrating quasi-phase-matched optical parametric oscillator in periodically poled linbo3. *Opt. Lett.*, 21(8):591–593, Apr 1996.

[19] D. N. Nikogosian V. G. Dmitriev, G. G. Gurzadyan. *The Handbook of Nonlinear Optics,*. Springer, 1991.

[20] Dieter H. Jundt. Temperature-dependent sellmeier equation for the index of refraction, ne, in congruent lithium niobate. *Opt. Lett.*, 22(20):1553–1555, Oct 1997.

[21] M.V. Hobden and J. Warner. The temperature dependence of the refractive indices of pure lithium niobate. *Physics Letters*, 22(3):243 – 244, 1966.

[22] D. C. Edelstein, E. S. Wachman, and C. L. Tang. Broadly tunable high repetition rate femtosecond optical parametric oscillator. *Applied Physics Letters*, 54(18):1728–1730, 1989.

[23] D. T. Reid, Z. Penman, M. Ebrahimzadeh, W. Sibbett, H. Karlsson, and F. Laurell. Broadly tunable infrared femtosecond optical parametric oscillator based on periodically poled rbtioaso4. *Opt. Lett.*, 22(18):1397–1399, Sep 1997.

[24] A. Miller W. Sibbett D. T. Reid, G. T. Kennedy and M. Ebrahimzadeh. Widely tunable, near- to mid-infrared femtosecond and picosecond optical parametric oscillators using periodically poled linbo3 and rbtioaso4. *IEEE J. Sel. Top. Quantum Electron.*, 4:238–248, 1998.

[25] P. Loza-Alvarez, C. T. A. Brown, D. T. Reid, W. Sibbett, and M. Missey. High-repetition-rate ultrashort-pulse optical parametric oscillator continuously tunable from 2.8 to 6.8 μm. *Opt. Lett.*, 24(21):1523–1525, Nov 1999.

[26] Baigang Zhang, Jianquan Yao, Hao Zhang, Degang Xu, Peng Wang, Xuejin Li, and Xin Ding. Angle-tuned signal-resonated optical parametric oscillator based on periodically poled lithium niobate. *Chin. Opt. Lett.*, 1(6):346–349, Jun 2003.

[27] S. D. Butterworth, M. J. McCarthy, and D. C. Hanna. Efficient widely-tunable operation of an all-solid-state synchronously pumped optical parametric oscillator. In *Advanced Solid State Lasers*, page NF17. Optical Society of America, 1993.

[28] Tobias P. Lamour, Jinghua Sun, and Derryck T. Reid. Wavelength stabilization of a synchronously pumped optical parametric oscillator: Optimizing proportional-integral control. *Review of Scientific Instruments*, 81(5):053101, 2010.

CHAPTER 5

ATTEMPTED NONRADIATIVE LIFETIME MEASUREMENTS IN TRIVALENT NEODYMIUM YTTRIUM ALUMINUM GARNET CRYSTALS

5.1 Nonradiative Lifetimes in four-level laser systems.

Three types of nonradiative (NR) decay are critical to the operation of four-level laser systems. The first occurs during the pumping process where excited electrons nonradiativly decay from the pumping level to a lower energy metastable state which serves as the upper lasing level. These transitions typically take place at a rate which is much faster than the lifetime of the metastable level to ensure population inversion. In addition, this NR decay to the lasing level must be more probable that that to any other level to avoid excessive loss and increased lasing threshold. The second type of NR decay is that from the metastable lasing level to any other energy, where any NR decay from this level reduces the quantum efficiency of the laser and serves as a depletion mechanism, reducing population inversion and laser performance. A third NR transition that has critical impact to laser performance takes place from the terminal laser which determines three or four level operation. Faster relaxations clear the lower level making population inversion much easier while reducing the saturation fluence of the system. A diagram showing the energy levels of a four-level laser gain medium is shown in figure 5.1. The NR decay we attempted to measure in this experimentation is labeled radiationless transfer. The study of NR mechanisms provides insight into the thermal properties of laser gain mediums and enables novel pumping schemes towards increase efficiency such as direct and two photon excitation.

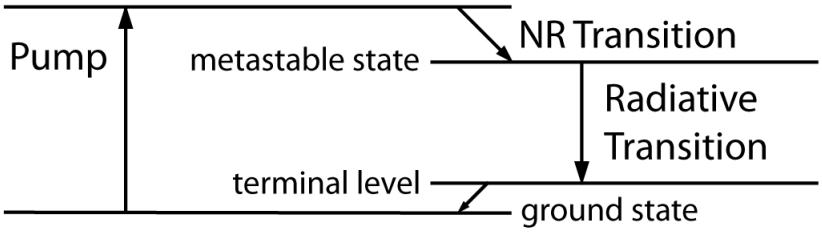

Figure 5.1: Generic four-level energy levels

5.2 Trivalent Neodymium Yttrium Aluminum Garnet

Neodymium doped yttrium aluminum garnet (ND:YAG) is a common gain medium in solid-state lasers with a chemical formula of: $Nd^{3+} : Y_3Al_5O_{12}$, where yttrium atoms are replaced with Nd^{3+} ions of comparable size. The quantum configurations for the neodymium atom and the Nd^{3+} ion are givien below.

$$Nd \Rightarrow 1s^2 2s^2 2p^6 3s^2 3p^6 3d^{10} 4s^2 4p^6 4d^{10} 4f^4 5s^2 5p^6 5d^0 5f^0 6s^2 \tag{5.1}$$

$$Nd^{3+} \Rightarrow 1s^2 2s^2 2p^6 3s^2 3p^6 3d^{10} 4s^2 4p^6 4d^{10} 4f^3 5s^2 5p^6 \tag{5.2}$$

Note that in the Nd^{3+} ion, the 4f ground state is shielded by 5s and 5p electrons thus the 4f levels of the Nd^{3+} ions are only weakly effected by the host ligand fields. But the effect is not zero and the energy levels are effectively split into nondegenerate bands through spin orbit coupling and weak crystal field splitting. The split ${}^4F\frac{5}{2}$ manifold provides a broadened absorption band peaking at 808 nm which is commonly used as the pump manifold as shown in figure 5.2. A measurement of the pump spectrum centered at 808 nm that is is used to excite the ground state electrons is shown in figure 5.3. When a population inversion is generated within the sample by a pump pulse, the stored energy becomes available for amplification of a probe beam. The probe pulses see gain as they pass

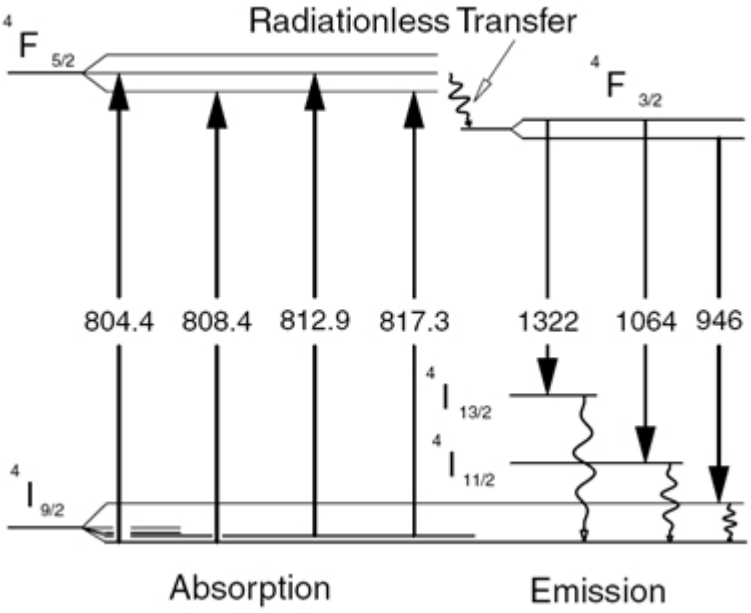

Figure 5.2: Energy levels found in ND:YAG laser crystals, courtesy of MEOS 2003.

through the energized region of the crystal. The gain is dependent on the number of excited ions the pump can generate and is therefore a function of pump absorption, the pulse and photon energies, as well as the beam's mode volume inside the sample. A pump wavelength of 808 nm with 2.46 x10^{-19} J/photon corresponds with the peak absorption band of the ND:YAG crystal ensuring maximum energy transfer to the Nd ions. The absorption of light as a function of penetration depth and material properties is given by the Beer-Lambert law:

$$I(z) = Exp(-n_{Nd} \cdot \sigma_a \cdot z) \tag{5.3}$$

where I is in W/cm^2, σ_a is the absorption cross section at 7.7x10^{-20} cm^2/atom, and n_{Nd} is the Nd^{3+} ion density at 1% doping or 1.36x10^{20} atoms/cm^3. Figure 5.4 is a plot showing the normalized 808 nm pump beam intensity as a function of penetration depth. Examining the graph, it is seen that the material is strongly absorptive at this wavelength and that high efficiencies can be achieved at crys-

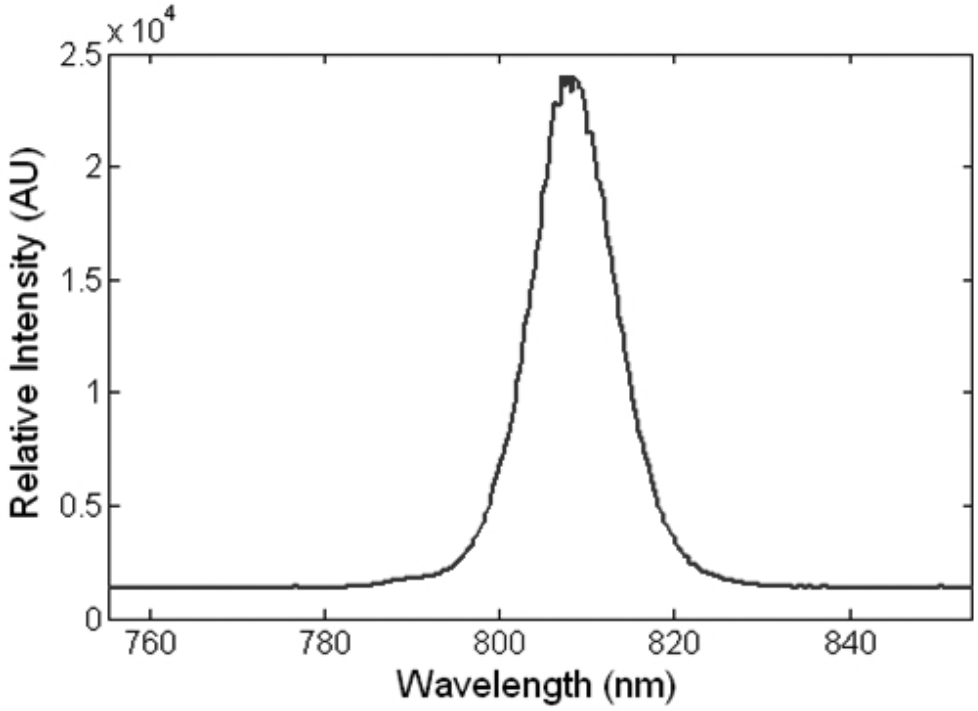

Figure 5.3: Spectral content of pump pulse, centered at 808 nm with a pulse width near 90 fs.

tal lengths greater than 1mm. Sample lengths between 1 and 6 mm were used during experimentation. These calculations are certainly a best case approximation due to the variations in absorption across the bandwidth of the pump laser which spans nearly 12 nm FWHM. Fortunately, the absorption lines in ND:YAG are relatively broad due to spin orbit coupling and weak crystal field splitting in the ${}^4F_{\frac{5}{2}}$ manifold providing strong absorption over this band.

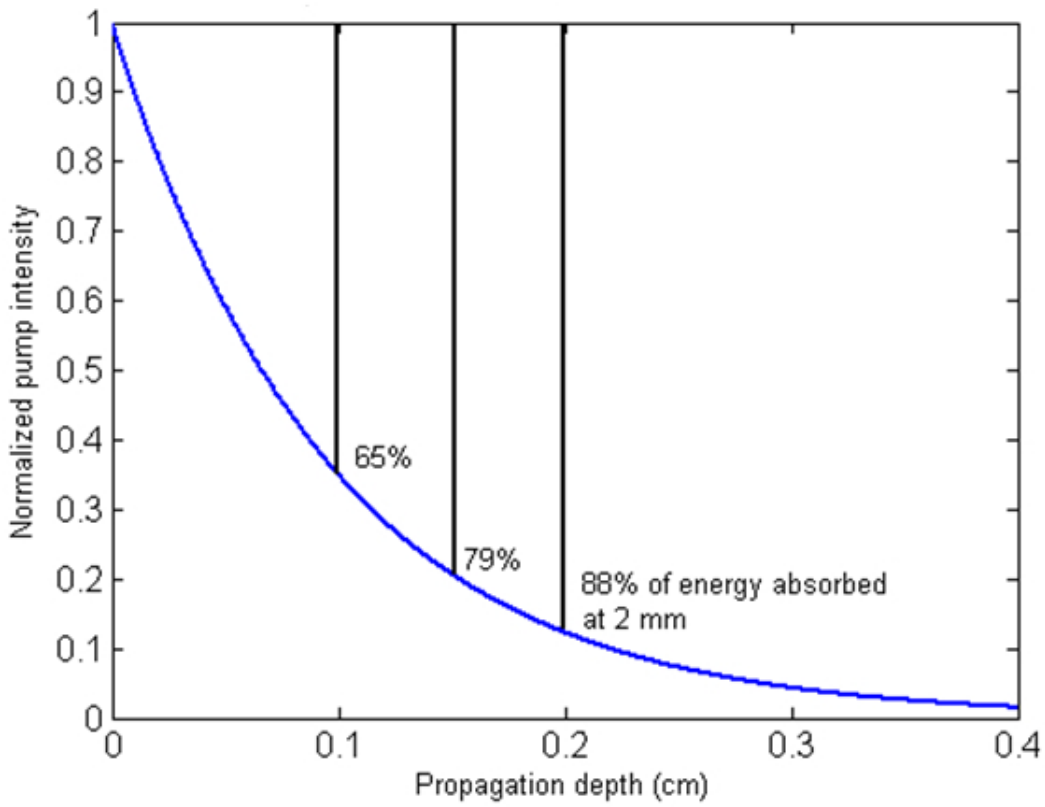

Figure 5.4: Pump intensity as a function of propagation length in 1% doped ND:YAG crystal.

5.3 The Energy Gap Law

The multi-phonon relaxations of excited states in rare-earth ion doped crystals and glasses were first investigated in the 1960s [1, 2, 3, 4, 5] but have seen a recent surge of interest in the late 1990's and after 2000 due to the increased availability of tunable pulse generation over a wide range of photon energies [6]. This led to the experimental observation of saturated phonon modes under high intensity excitation and to more advanced theoretical models [7, 8]. The Energy Gap Law can be used to estimate the multi-photon non-radiative decay

B = 6.9 x 10^{13} s^{-1}	β = 8.01 x 10^{-3} cm	$\hbar\omega$ = 700 cm^{-1}
K_B = 0.695 cm^{-1}/K	ΔE = 848 cm^{-1}	T = 300 K
Results	W_{nr}=8 x 10^{10} Hz	τ_{nr} = 12 ps

Table 5.1: Physical parameters used in the Energy Gap Law calculations and the resultant multiphonon decay rate and lifetime for the $^4F\frac{5}{2}$ manifold in Nd:YAG.

rates in rare-earth doped hosts. The law predicts a multiphoton decay rate with exponential dependence on the energy gap between the excited energy level and the lower energy target level after relaxation. The multiphoton decay rate can be expressed by the Energy Gap Law in the following form:

$$W_{nr} = B \cdot exp(-\beta \cdot \Delta E) \cdot \left(1 - exp\left(\frac{h\nu_{max}}{k_B \cdot T}\right)\right)^{-\frac{\Delta E}{\hbar\omega}} \tag{5.4}$$

Where the values of B and β are empirically fitted host parameters while ΔE is the energy gap between levels and hν_{max} is the highest phonon energy supported by the host medium. Using host parameter values for YAG from the literature [9, 10, 11, 12], and Nd:YAG energy states, the non-radiative rate of the $^4F\frac{5}{2}$ manifold was calculated to be W_{nr}=8 x 10^{10} Hz with a lifetime of τ_{nr} = 12 ps. The values used for the calculation are listed in table 5.1. The host parameters B and β are assumed to be independent of the 4f states of the doped ions. The energy of the highest frequency optical phonon (hν_{max}) is taken from the hosts vibration spectrum where the least number of phonons required to bridge the gap is derived simply from:

$$\text{Least number of phonons to bridge energy gap} = \frac{\Delta E}{h\nu_{max}} \tag{5.5}$$

The plot in figure 5.5 shows the Nd:YAG multiphoton nonradiative lifetime of the $^4F\frac{5}{2}$ level as a function of the energy gap as calculated using the Energy

Gap Law as previously shown in equation 5.4. The calculated lifetime of approximately 12 ps given an expected energy gap of 848 cm^{-1} or 1.68 x 10^{-20} J is highlighted.

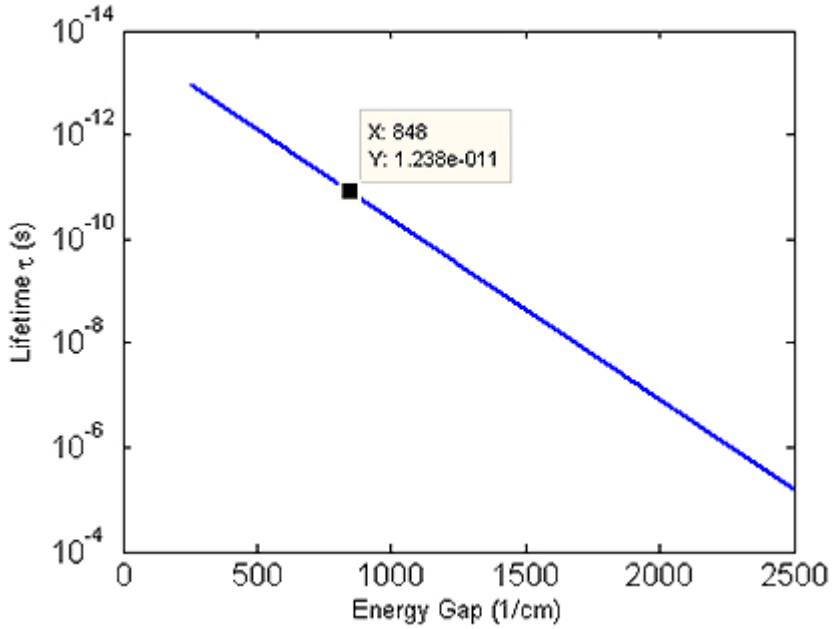

Figure 5.5: Plot of nonradiative ${}^4F5/2$ lifetime in Nd:YAG as a function the energy gap according to the Energy Gap Law and host parameters from the literature [12]

The Energy Gap Law was validated many times as an accurate way to predict nonradiative lifetimes in rare-earth doped hosts [13, 14, 15], but loses accuracy for gaps that exceed energies greater that 4 to 5 times the highest phonon energy supported in the medium where the probabilities of coordinated multiphonon relaxations begin to give way to fluorescent decay. For this experimentation, the ratio of the maximum supported phonon energy to that of the gap between the ${}^4F_{\frac{5}{2}}$ and the ${}^4F_{\frac{3}{2}}$ levels in Nd:YAG is only 1.2 which is within the validity of the energy gap theory.

5.4 Saturation Energy

The saturation energy is the optical pulse energy required to excite a considerable portion (in this case half) of the doped ions into the upper level in a gain medium or saturable absorber, while the saturation fluence is the saturation energy per unit area (J/cm^2) which is dependent on the absorption cross section for a given wavelength as follows:

$$e_{sat} = \frac{h \cdot \nu}{\sigma_{abs}} \tag{5.6}$$

where $h\nu$ is the photon energy and σ_{abs} is the absorption cross section in cm^2. In the case of ND:YAG we assume that all absorbed photons are from the ground level (no two photon absorption), that the ${}^4F_{\frac{5}{2}}$ to ${}^4F_{\frac{3}{2}}$ transition has negligible radiative emissions, so that W_{total}=W_{nr}+W_r ≈W_{nr}, and that there is no branching to other levels. The saturation intensity in (W/cm^2) is then given by:

$$I_{sat} = \frac{h \cdot \nu}{\sigma_{abs} \cdot \tau} \tag{5.7}$$

where τ represents the upper-state lifetime in seconds. Given 808 nm or 2.46 x10^{-19} J/photon, and an absorption cross section of 7.7 x 10^{20} cm^2 per ion for ND, we get an intensity saturation of $I_{sat} = 1.39 W/cm^2$ and energy density saturation of $e_{sat} = 319 J/cm^2$. The pump intensity inside the sample is dependent on optical power, and mode volume in the crystal. The output from the Tsunami Ti:sapphire laser can be accurately modeled as a Gaussian beam with TEM_{00} transverse mode and the following intensity profile:

$$I(x, y) \propto -k(x^2 + y^2). \tag{5.8}$$

The mode volume can be estimated by calculating the focused beam waist over a specified confocal parameter. The Rayleigh range is defined as the distance

from the focal point that the beam width expands by a factor of $\sqrt{2}$ given by:

$$Z_R = \frac{\pi \cdot w_o^2}{\lambda} \tag{5.9}$$

Where w_o is the beam radius at the focus and λ is the wavelength. The confocal parameter is simply twice the Rayleigh range so that given a desired confocal parameter; the beam radius can be calculated:

$$w_o = \sqrt{\frac{b \cdot \lambda}{2\pi}} \tag{5.10}$$

Where b represents the confocal parameter or $2Z_R$. Assuming a confocal parameter of 1 mm we get a beam radius of 11.4 μm and a radiated sample volume of 4.04 X 10^{-7} cm^3. There are 5.5 x 10^{13} ions in the mode volume at 1% doping requiring 6.76 x 10^{-6} J to excite half the ions within the mode volume. Given a pulse energy of 1.75 x 10^{-8} J, the sample will see a best case saturation of 0.26 percent. A change of such small magnitude is difficult to detect and in this case must be extracted from the noise. The signal processing techniques employed in an effort to detect this change are outlined in section 4.6.

5.5 Rate Equations

Rate equations are used to model the population dynamics within a gain material. This section examines the evolution of level population with time, for a four-level Nd:YAG sample, with emphasis on the availability of excited states for 1064 nm probe gain. The differential rate equation for the pumping level

(N_4), along with the general solution, is shown below:

$$\frac{dN_4}{dt} = -\frac{1}{\tau_4} \cdot N_4(t) \Rightarrow N_4(t) = p \cdot e^{-\left(\frac{t}{\tau_4}\right)} \tag{5.11}$$

where p is the initial N4 population at t=0 and τ_4 is the nonradiative lifetime from the pump level. Here we assume no additional branching so that all the energy that leaves level four goes to level three and that the$^4F\frac{5}{2}$ manifold functions as a single energy level. The differential rate equation for the upper lasing level (N_3) can be written as

$$\frac{dN_3}{dt} = p \cdot e^{-\left(\frac{t}{\tau_4}\right)} - \frac{1}{\tau_3} \cdot N_3(t) \tag{5.12}$$

and can be solved with the first order linear differential equation theorem, giving the population behavior for N_3 as:

$$N_3(t) = \frac{e^{-\frac{t}{\tau_3}}\left(-1 + e^{\frac{t(\tau_4 - \tau_3)}{\tau_4 \cdot \tau_3}}\right) \cdot p \cdot \tau_3}{\tau_3 - \tau_4} \tag{5.13}$$

where τ_3 is strictly a function of radiative decay to the lower lasing level. A comparison of typical NR lifetimes and how they affect the upper level (N3) population growth are plotted in figure 5.6 and figure 5.7 over different observation times.

The Energy Gap Law calculations predicted a N4 NR lifetime of 12 ps. Using this predicted value for estimation, the graphs show that over 85 percent of the pulse induced carriers have decayed within 20 ps suggesting that a 60 ps scan range is reasonable for the pump and probe delay. The graph in figure 5.8 shows the upper lasing level population decay given a metastable lifetime of 250 μs. The long metastable lifetime ensures that negligible decay from N3

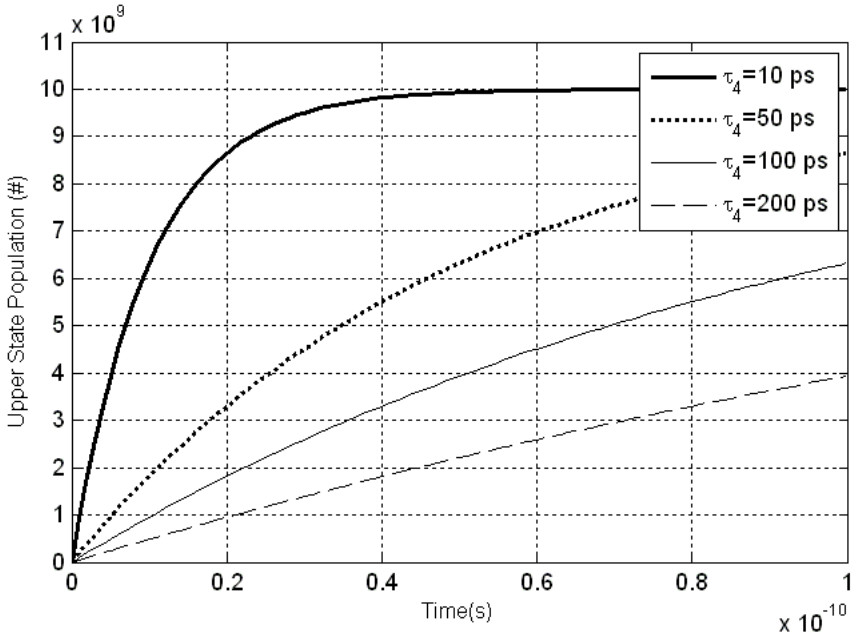

Figure 5.6: Growth of upper state level.

occurs during the delay between the arrival of the pump and probe, so that any potential probe gain is undiminished. The pulse widths involved are also much shorter than any of the involved lifetimes ($\tau_p << \tau_4 << \tau_3$) providing the required resolution to detect any picosecond timescale dynamics.

5.6 Nd:YAG Sample Preparation

The Nd:YAG samples were prepared from cylindrical crystal rods doped with a 1% Nd^{3+} ion density at $1.36x10^{20}$ atoms/cm^3 and cut into variable lengths ranging from 1 to 6 mm that were polished prior to testing. A 1 mm thick sample was obtained through prior collaboration, but the thicker samples were cut from a 5 mm diameter rod with a water cooled diamond blade circular saw. Sections measuring 2 mm, 3 mm, and 6 mm were cut allowing for the use of

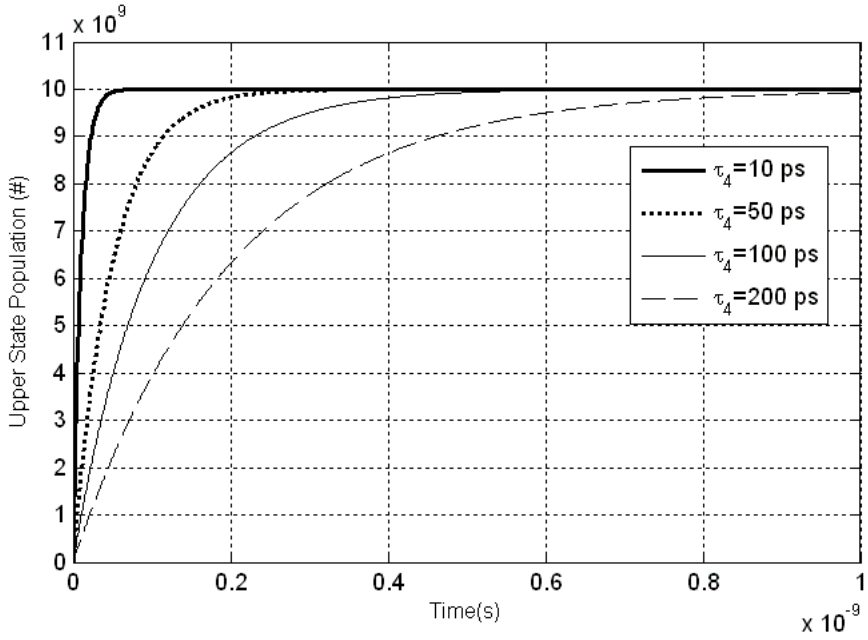

Figure 5.7: Growth of upper state level over longer time.

different confocal parameters with respect to the pump and probe beam focus. Each face was hand polished with diminishing sizes of aluminum oxides to remove the coarse highly dispersive damage caused by the cutting.

The samples were individually mounted on an optical post whose position was controlled by a three dimensional translational stage. A PPLN nonlinear crystal was also mounted on the post adjacent to the sample to facilitate easy switching between the PLLN and the sample. The mounting configuration proved to be advantageous during pump and probe beam alignment and for quickly verifying or optimizing the mode overlap within the crystals. A diagram showing the mount is presented in figure 5.9. The sample was held in place with a drop of hot glue which made swapping out samples relatively simple but the PPLN crystal was mounted on a more complicated piece of folded copper that reqired carefull handling so as not to bump the crystal out of alignment.

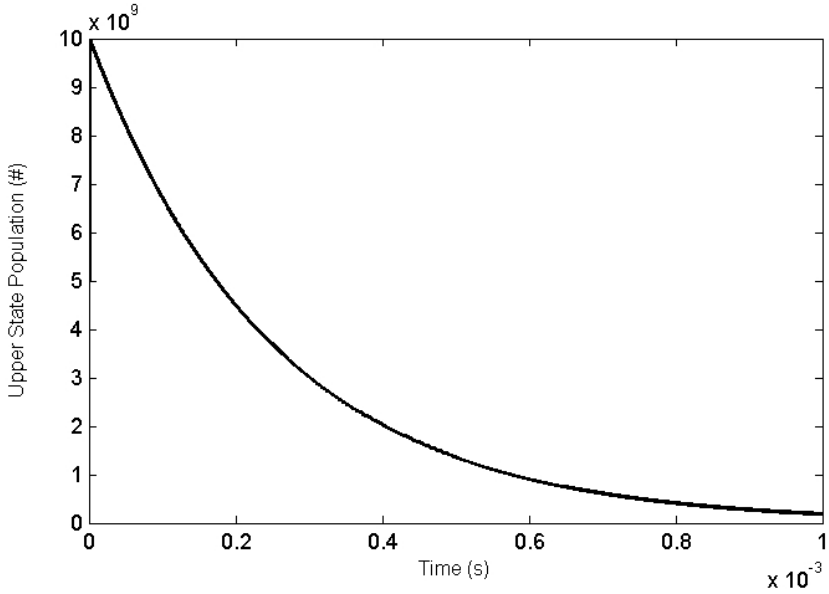

Figure 5.8: Decay of upper state level over longer time.

5.7 Measurements

Chapters 3 and 4 examined the theory and design of the tunable femtosecond, dual wavelength, time resolved pump probe system. The general configuration used in time resolved measurements was covered with emphasis on overall performance and capabilities. Additionally, within the previous sections of chapter 5, the physical properties of Nd:YAG were reviewed to include excited energy levels, optical absorption, and saturation intensity. The expected value of the ${}^4F_{\frac{5}{2}}$ lifetime in Nd:YAG was theoretically determined to be near 12 ps and the rate equations provided a solid estimate of how the gain in the probe signal evolves with time. This section examines the specific methodology used during the attempted measurements of the ${}^4F_{\frac{5}{2}}$ lifetime in Nd:YAG.

A reasonable scan length to measure the decay (seen as probe gain) for the assumed 12 ps lifetime was determined to be near 60 ps which corresponds to

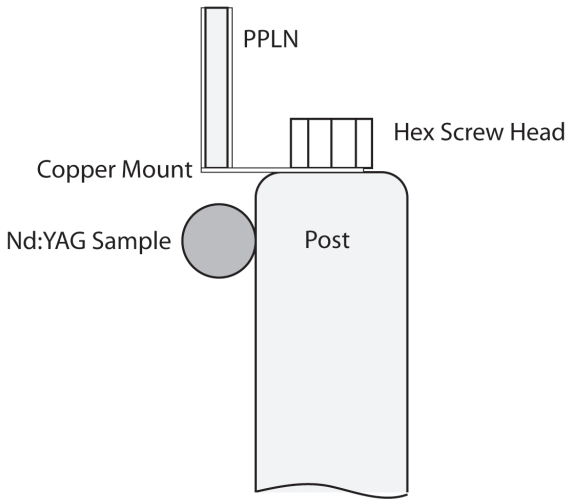

Figure 5.9: The mount used to hold the Nd:YAG samples and the PPLN nonlinear crystal.

an optical path length change of 1.8 cm. Our system reliably produced a corner cube scan length of 1.5 cm in the double pass arm of the beam path, which gave 100 ps of travel. A 1 mm glass slide was used to calibrate the scanning mechanism by taking preliminary measurements with the slide both in and out of the beam path. The pump was tuned to an 808 nm center wavelength and set at the maximum average output power at the sample of 1.4 W at 80.6 MHz with 17 nJ per pulse. The pump beam was focused to approximately 11 μm along with the probe in a collinear configuration. Residual pump energy was removed from the combined beams that exited the sample with a monochromator before the filtered probe energy reached the detector. Many signal detection and processing configurations were constructed in the attempted measurement of the ^{4}F5/2 lifetime, but no satisfactory data was recorded. Intensity fluctuations in the detected probe signal obscured any gain that might have been present in the pulses. This was not entirely unexpected since the best case probe signal gain was predicted to be around 0.2 percent. Signals so deeply obscured by noise are

difficult to detect but these difficulties were compounded by optimistic predictions of noise levels and system stability. The boxcar integrator was itself a large source of noise with sensitive and often times unpredictable reliability. In addition, the synchronization of much of the older equipment pushed the limits of the technology with required responses in the 3 to 12 ns range. But certainly the most obvious factor responsible to the lack of detected signal was the relatively weak pulse energies. Pulse energies on the order of 1 μJ are required to see a much more prominent saturation of near 15 %.

The pulse energies required to generate a strong and detectible signal can be easily realized with multi-pass regenerative amplifiers that produce pulse energies greater than 4.0 mJ, but budget constraints could not support such a purchase at that time. As far as we know, this lifetime has never been successfully directly measured, since it requires extremely specialized pump probe capabilities. After considerable effort, it was decided that this measurement be temporarily postponed to concentrate on new developments in ultrafast optics until additional equipment became available. Thus the capabilities of the pump probe system were focused on exploring the ultrafast carrier dynamics of highly ordered pyrolytic graphite (HOPG) which is covered in the next chapter.

BIBLIOGRAPHY

[1] M. J. Weber. Selective excitation and decay of er^{3+} fluorescence in laf_3. *Phys. Rev.*, 156(2):231–241, Apr 1967.

[2] M. J. Weber. Radiative and multiphonon relaxation of rare-earth ions in y_2o_3. *Phys. Rev.*, 171(2):283–291, Jul 1968.

[3] M. J. Weber. Probabilities for radiative and nonradiative decay of er^{3+} in laf_3. *Phys. Rev.*, 157(2):262–272, May 1967.

[4] W. D. Partlow and H. W. Moos. Multiphonon relaxation in lacl_3: nd^{3+}. *Phys. Rev.*, 157(2):252–256, May 1967.

[5] L. A. Riseberg and H. W. Moos. Multiphonon orbit-lattice relaxation of excited states of rare-earth ions in crystals. *Phys. Rev.*, 174(2):429–438, Oct 1968.

[6] F. S. Ermeneux, C. Goutaudier, R. Moncorgé, Y. Sun, R. L. Cone, E. Zannoni, E. Cavalli, and M. Bettinelli. Multiphonon relaxation in yvo_4 single crystals. *Phys. Rev. B*, 61(6):3915–3921, Feb 2000.

[7] Jianhu Yang, Shixun Dai, Nengli Dai, Lei Wen, Lili Hu, and Zhonghong Jiang. Investigation on nonradiative decay of 4i13/2–¿4i15/2 transition of er3+-doped oxide glasses. *Journal of Luminescence*, 106(1):9 – 14, 2004.

[8] Auzel F. Excitation effects in non-radiative multiphonon decays of rare earth doped laser materials. *Optical Materials*, 8:15–20(6), July 1997.

[9] M. J. Weber. Nonradiative decay from 5d states of rare earths in crystals. *Solid State Communications*, 12(7):741 – 744, 1973.

[10] Richard C Powell. *Physics of Solid State Laser Materials*. Springer, 1998.

[11] P. F. Liao and H. P. Weber. Fluorescence quenching of the 4f3/2 state in nd x2010;doped yttrium aluminum garnet (yag) by multiphonon relaxation. *Journal of Applied Physics*, 45(7):2931 –2934, July 1974.

[12] B.M. van der Ende, R.L. Brooks, H.F. Tiedje, and H.K. Haugen. Measurement of the and manifold lifetime in nd3+:y3al5o12 and nd3+:laf3. *Journal of Luminescence*, 124(2):311 – 315, 2007.

[13] M. J. Weber. Multiphonon relaxation of rare-earth ions in yttrium orthoaluminate. *Phys. Rev. B*, 8(1):54–64, Jul 1973.

[14] Camille Bibeau, Stephen A. Payne, and Howard T. Powell. Direct measurements of the terminal laser level lifetime in neodymium-doped crystals and glasses. *J. Opt. Soc. Am. B*, 12(10):1981–1992, Oct 1995.

[15] Tasoltan T. Basiev, Alexei Yu. Dergachev, Yurii V. Orlovskii, and Alexander M. Prokhorov. Multiphonon nonradiative relaxation from high-lying levels of nd3+ ions in flouride and oxide laser materials. *Journal of Luminescence*, 53(1-6):19 – 23, 1992.

CHAPTER 6

FEMTOSECOND CARRIER DYNAMICS IN PHOTOEXCITED HIGHLY ORDERED PYROLYTIC GRAPHITE FILMS

6.1 Femtosecond Carrier Dynamics in Photoexcited HOPG films

Graphene and graphite thin films have been the subject of great interest due to their unique material properties and their potential for applications in electronics, ultrafast optics, and as the focus of basic research [1, 2]. The hexagonal symmetry and strong covalent bonding found in graphite are responsible for the material's planar structure. Additionally, the relatively weak coupling between individual atomic layers gives rise to graphite's quasi-2D behavior, so that many of graphene's useful characteristics are found in few layer graphite (FLG) films with the electronic properties of the nearly decoupled layers governed by Dirac fermions [3, 4]. FLG is also readily fabricated and robust in nature; thus, FLG holds great promise for applications in electronics and optics [5, 6]. Graphite has been shown to act like a semiconductor with a vanishing bandgap approaching the Dirac point [1] while demonstrating broad spectrum optical absorption. This broadband nature coupled with ultrafast relaxation processes make these materials potential saturable absorbers in mode-locked lasers [7, 8, 9], although the linear increase of nonsaturable absorption with increasing layers limits the use of FLG to systems with high loss tolerances.

The relaxation of photo-excited carriers in graphene and graphite films can be grossly attributed to four mechanisms; intraband carrier-carrier equilibration, optical phonon emission [10, 11], acoustic phonon emission, and electron-

hole recombination. The electrons and holes relax in similar ways due to the symmetric band structure where the probabilities of occupation are related $fe(E) = fh(-E)$. Through the use of mode locked lasers, optically excited electron-hole plasmas can be generated within a sample and then probed to watch their return to the pre-perturbed state. Time resolved measurements of these relaxations shed light on the internal mechanisms that govern these processes.

The measurement of excited carrier dynamics of FLG and graphene is important for determining suitable applications for these unique materials and in uncovering the basic physics behind their behavior. The published literature documents the detection of excited carrier relaxations that range from a few fs to ps [12, 13, 14, 15]. This chapter focuses on the measurement of two initial ultrafast relaxations to be referred as τ_1 and τ_2 which are products of intraband carrier-carrier and carrier-phonon interaction respectively. Figure 6.1 shows the theoretical relationship between these relaxations as a function of energy and time. Recently, ultrafast carrier dynamics in FLG were investigated with optical pump-probe spectroscopy utilizing 7 fs pulses with reported lifetimes of $\tau_1 = 13 \pm 3$ fs and τ_2 on a 100 fs timescale [15]. Additionally, Z-scan measurements of epitaxial graphene determined τ_1 to be 8 ± 3 fs [16]. Both results correspond well with our results obtained using the equal pulse correlation technique (EPC) on FLG samples described in this work.

There can be substantial difficulties using traditional pump-probe techniques for extracting relaxation times in systems where a relatively fast process is overlaid by a significantly slower one [17, 18, 19]. In this chapter we document the use of the EPC technique to examine ultrafast relaxations in thin film graphite which are much shorter than the laser pulse. EPC is a degen-

erate form of pump-probe using identical pulses at orthogonal polarizations, allowing the measurement of time constants on the order of one tenth the laser pulse width [20, 21]. Saturation of the absorption results in the symmetric increase in transmission centered about the zero delay point, which is detected as a peak over an otherwise constant transmission background. The presence of this transmission correlation peak (TCP) is a direct indicator to the existence of a fast relaxation process. The TCP is proportional to the intensity autocorrelation convolved with a double sided exponential decay of time constant τ, which is easily extracted from the data. In this work, two decay times (τ_1 and τ_2), corresponding to carrier-carrier and carrier-phonon interactions were determined using a least squares fit algorithm that in essence deconvolves the TCP into the known intensity autocorrelation and unknown double sided exponentials that represent the subsequent relaxations. The idealized theoretical decay process of excited carriers in relation to the measured relaxations is shown in figure 6.1.

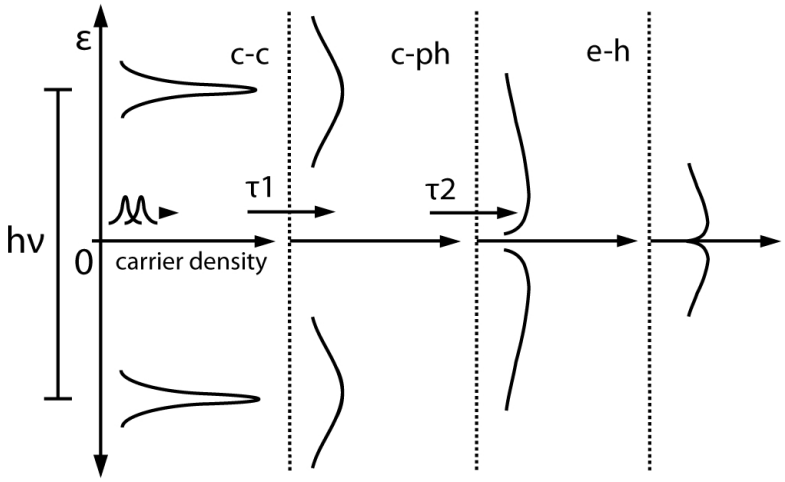

Figure 6.1: Diagram depicting the idealized evolution of the photo-excited carriers with respect to energy and time. The pulses are overlapped in the sample at t=0).

6.2 The Equal Pulse Correlation Technique

The equal-pulse correlation technique [19, 20] is an effective method to extract extremely fast excited state relaxation times in the presence of slower relaxation mechanisms. In addition, this method provides the means to measure relaxation times much shorter than the pulse of the probing laser, down to approximately one-tenth the pulse width. This degenerate pump-probe technique utilizes the effects of saturation on the absorption of equal amplitude optical pulses passing through a sample. A pump pulse is used to optically excite lower level energy states into higher levels, altering a selected material property of the sample to be monitored. Then a probe pulse, slightly delayed in time, is used to examine the sample for changes in its reflectivity or transmissivity which can be tied back to changes induced by the pump pulse. Unlike typical pump-probe measurements, these pulses are equal in power, wavelength and shape. The beam is separated into two identical pulse trains of orthogonal polarizations and recombined collinearly through the use of a polarizing beam splitter. A variable delay (τ_d) between pulses is controlled by a piezoelectric transducer located in one arm of an interferometer. The combined flux incident on the sample from both pulses as a function of time is given by:

$$I_{combined} = I_1 f(t) + I_2 f(t - \tau_d) \tag{6.1}$$

where f is the pulse envolope function, the flux I is in units of (photons/second) and the variable delay (τ in seconds) is controlled by the optical delay line as depicted in figure 6.2. The pulse envelope is often assumed to be Gaussian of the form:

$$f(t) \propto \exp[-8ln2(t/T_p)^2] \tag{6.2}$$

or a hyperbolic secant squared:

$$f(t) \propto sech^2(t/T_p) = \frac{1}{cosh^2(t/T_p)} \tag{6.3}$$

when dealing with laser pulses. Recall that the pulses intensities are equal (I_1 =

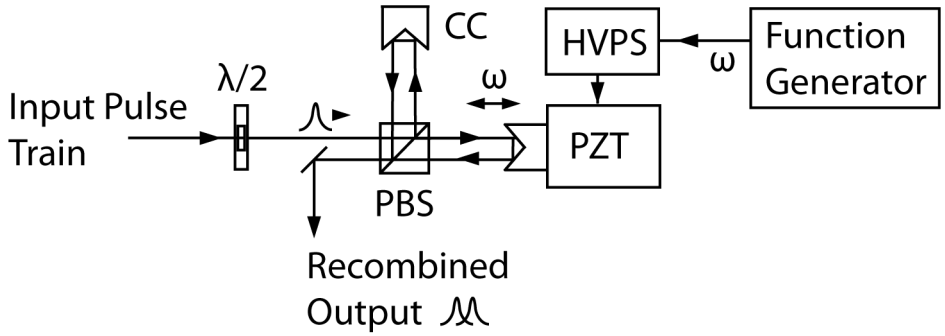

Figure 6.2: Block diagram of the beam splitter and delay line configuration: CC, corner cube; PBS, polarizing beam splitter; HVPS, high voltage power supply.

$I_2 = I$) in EPC thus the combined flux simplifies to:

$$I_{combined} = I[f(t) + f(t - \tau_d)]. \tag{6.4}$$

Since the total transmitted flux from both pulses passing through the sample is measured, any increase in the throughput caused by partial saturation is detected. This change in total transmitted power (ΔT) is a function of the pulse intensities and is proportional to:

$$\Delta T \propto \int_{-\infty}^{\infty} I[f(t) + f(t - \tau_d)][n_1(t, \tau) - n_3(t, \tau)]dt \tag{6.5}$$

where n1, and n3 are the fractional densities of absorbing centers in the energy states as described in Taylor's original paper [20]. The detected signal shows a symmetric increase in transmission centered about the zero delay point and is observed as a peak over an otherwise constant transmission background. The

appearance of a transmission correlation peak (TCP) is a sure sign to the existence of a fast relaxation process in the sample, such that if no nonlinear saturation were present, the change in transmission would be zero ($\Delta I = 0$). A diagram detailing a typical EPC detection scheme is shown in figure 6.3. Other configurations have been demonstrated and are well documented in the literature [22, 23, 24, 25, 19], while all are similar in basic design, they employ varying methods of noise reduction. A common method of noise reduction, and the method used in this research, is to split the pulse train into two arms allowing for balanced detection and the subsequent reduction of amplitude noise in the difference signal as shown in the diagram. A small percent of the beam is picked off by a beam splitter (bs) and bypasses the sample to pass directly through a neutral density (ND) filter and onto the reference arm of a balanced detector (D2), while the main beam is focused through the sample at normal incidence then collimated through a variable ND filter onto the signal arm of the detector (D2). Theoretical TCP signals for a variety of fast relaxation times representing

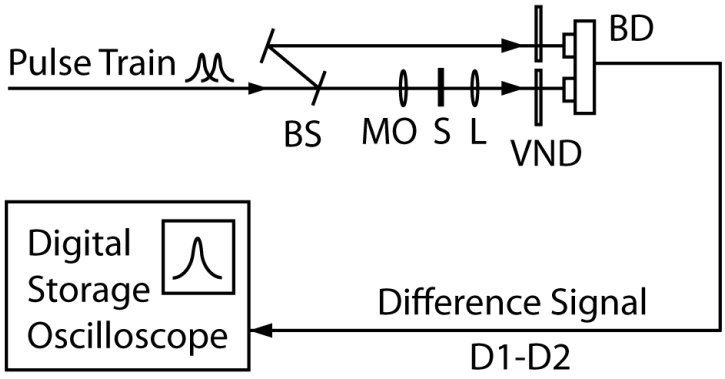

Figure 6.3: Block diagram of the transmitted power detection system: ND, neutral density filter, VND variable neutral density filter; BS, beam splitter; MO, microscope objective; S, sample; L, lens; BD, balanced detectors (D1,D2).

differenet percentages of the laser pulse width are shown in figure 6.4 along

with the corresponding intensity autocorrelation. The ECP technique is theoretically able to resolve relaxation times on the order of 1/10th of the laser pulse width represented by the liine adjacent to the intensity autocorrelation on the graph. It is a trivial exercise to resolve the TCP broadening theoretically but the

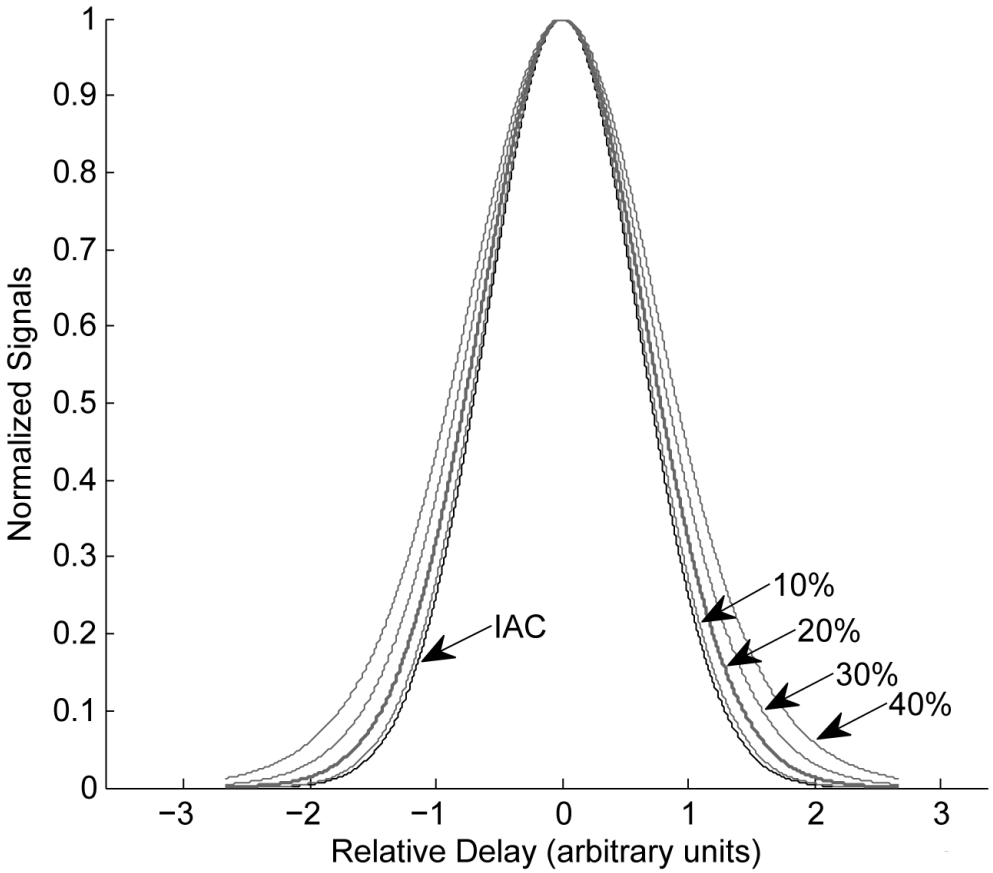

Figure 6.4: Simulation results showing the laser intensity autocorrelation compared to thebroadened TCP plots. The graph displays the TCP signals for relaxations between ten and forty percent of the laser pulse width. The curves are normalized to unity.

processes is experimentally sensitive to noise and requires careful collection of data. Even then, experimental limitations may restrict the temporal resolution to times much closer to the pulse width of the source. Since the TCP is propor-

tional to the convolution of the intensity autocorrelation with a double sided exponential decay, it is possible to extract the decay times through deconvolution given the known intensity autocorrelation. The approach used here convolves the intensity autocorrelation with different double sided relaxation curves and matches the theory to the data with a least squares fit algorithm. This method can be used to find multiply decays by weighting the presence of each decay, assigning a decay constant, and then testing the convolved curve against the data. This process is repeated until a match of sufficient fit is reached.

6.3 Experimental ECP set-up

A mode-locked Ti:Sapph laser centered at 800nm (1.55 eV) with a pulse repetition rate of 80 MHz was used to degenerately excite and probe the samples. The details of the experimental set-up are depicted in Figure 6.5 and an interferometric autocorrelation of 100 fs pump pulses measured by the system is given in figure 6.6. A four prism (SF-14) sequence configured external to the cavity was used to compensate for the dispersion of the optical components. The prisms were aligned to minimize and control the pulse width at the sample. Intensity autocorrelation measurements were simultaneously made at the lasers exit and at the location of the sample allowing for real time feedback during prism adjustment. Pulse durations between 80-150 fs were used to verify the resolution of the method with respect to pulse width. The beam was separated into two equal power pulse trains of orthogonal polarizations and recombined collinearly. A variable delay (d) between pulses is controlled by a piezoelectric transducer located in one arm of the interferometer with a scan frequency of 6.5 Hz and a total scan of 1.2 ps or 600 fs on each side of τ=0.

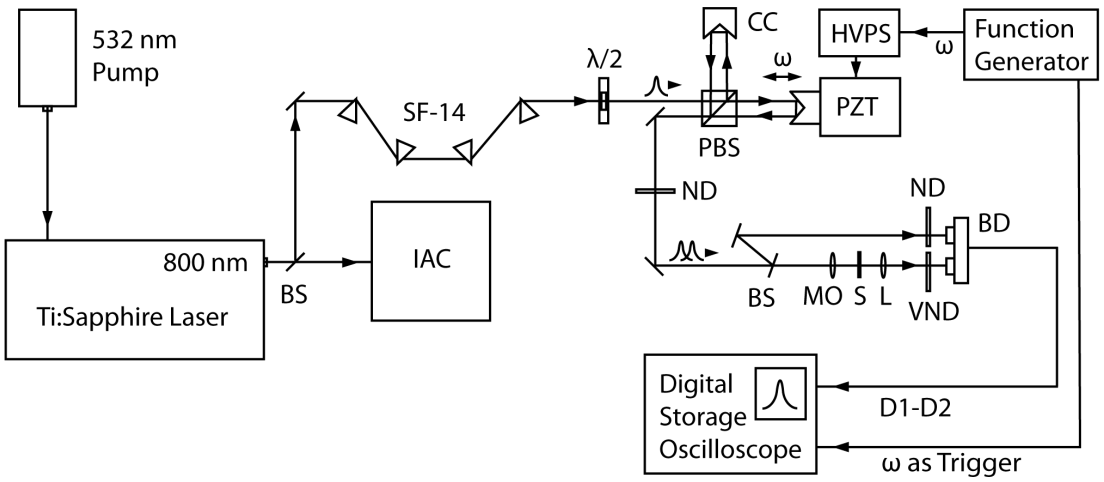

Figure 6.5: Schematic of experimental set-up. IAC, intensity autocorrelation; CC, corner cube; PBS, polarizing beam splitter; HVPS, high voltage power supply; ND, neutral density filter, VND variable neutral density filter; BS, beam splitter; MO, microscope objective; S, sample; L, lens; BD, balanced detectors (D1,D2).

A beam splitter was used to direct 5 percent of the recombined beam through a neutral density (ND) filter and onto the reference arm of a balanced detector (D2), while the main beam was focused through the sample at normal incidence by a 10X microscope objective, then collimated through a variable ND filter onto the signal arm of the detector (D2). The spot diameter at the sample was 30 μm. The irradiance on the photodiodes was kept low to ensure operation in the linear regime. The balanced detection scheme proved extremely effective in reducing the signal to noise ratio. The difference signal (D1-D2) was averaged over hundreds of cycles and recorded on a digital storage oscilloscope.

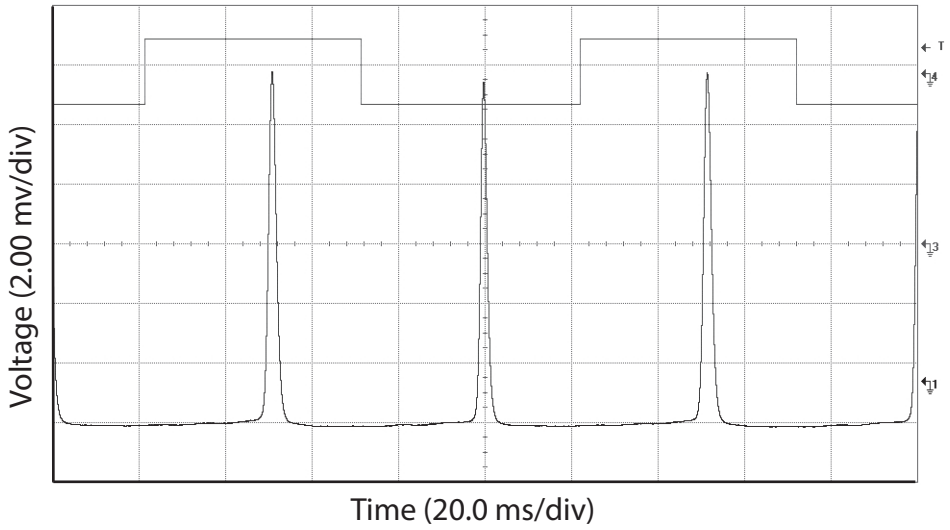

Figure 6.6: Oscilloscope trace of the intensity AC of the pump at at λ = 800 nm, with a pulse width near 80 fs. The square wave at the top is the trigger output from the corner cube scanning frequency.

6.3.1 Dispersion

When light travels in a vacuum, free from the perturbing nature of atoms, all frequency components travel at the same speed, universally referred to as c or at 2.99792 x10^8 m/s. This is not the case in a material medium. Chromatic dispersion is the phenomenon where different frequencies of a wave packet propagating in matter appear to travel at slightly different speeds. In other words, the index of refraction for a given medium behaves as though it is frequency dependent. This apparently slower propagation is a complex interaction of the subject wave and the surrounding electric fields generated in the host medium. Yet the net results of this electromagnetic interaction are a behavior that mimics a retarded wave with decreased phase velocity and it is this apparent behavior on which we will concentrate. Excellent acounts for the physical origin of the refractive index can be found in the literature [26, 27] and will not be discussed

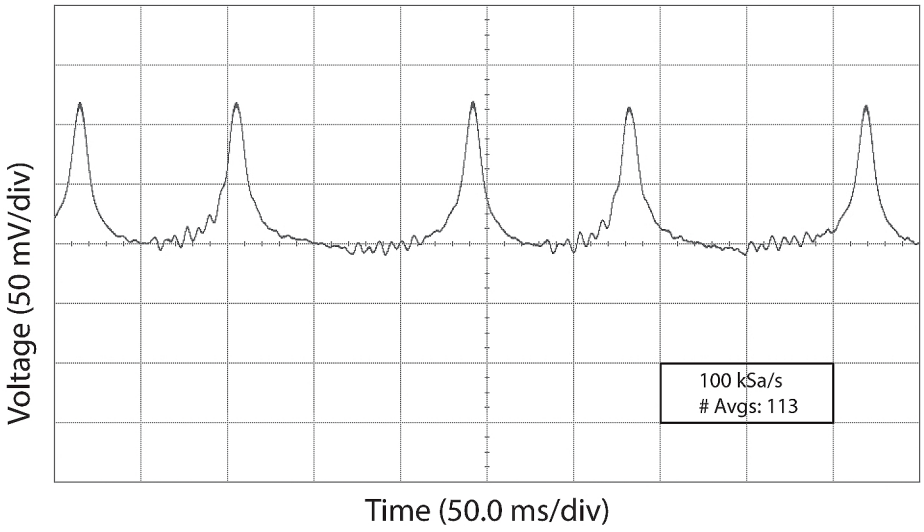

Figure 6.7: Oscilloscope trace of the difference signal averaged 113 times.

further here. All matter is dispersive and the frequency dependent phase velocity of a wave traveling in a material is given by the equation:

$$v_{ph} = \frac{c}{n(\omega)} \tag{6.6}$$

where v is the phase velocity of the wave and c and n are respectfully the vacuum speed of light and the material index of refraction.

When an optical pulse, which is composed of many frequencies, travels in a material, it accumulates phase as $exp(ik_o n(\omega)z)$ where the index (n) is frequency dependent, so that each frequency component of the wave experiences a different total phase. This is called dispersion, which it is not restricted to linear behavior and can be examined as a Taylor series approximation of the spectral phase function:

$$\phi(\omega) = \phi_o + \frac{\delta\phi}{\delta\omega}(\omega - \omega_o) + \frac{1}{2}\frac{\delta^2\phi}{\delta\omega^2}(\omega - \omega_o)^2 + \frac{1}{6}\frac{\delta^3\phi}{\delta\omega^3}(\omega - \omega_o)^3 + ... \tag{6.7}$$

where ϕ_o is the common phase, ω_o is the center angular frequency of the pulse, and ω is the specific angular frequency. Each term of the expansion represents a

specific type of dispersion, each becoming more complicated and difficult to correct with higher orders. The shorter the pulse (larger bandwidth), the more significant the higher order terms become. First order dispersion ($\delta\phi/\delta\omega$), known as group delay, is linear and results in a time delay of the pulse without altering the pulse shape. The group delay, like the absolute phase, cannot currently be measured by any self referencing techniques such as autocorrelation, frequency resolved optical gating (FROG) [28, 29], or SPectral Interferometry for Direct E-field Reconstruction (SPIDER) [30]. Second order dispersion ($\delta^2\phi/\delta\omega^2$) or the group delay dispersion (GDD) is responsible for chirping and separates the frequency components of a pulse. GDD is often given in units of fs^2 and is the product of group velocity dispersion (GVD) and material length, where GVD is a material property given in (fs^2/mm). Control of chirp, or how the instantaneous frequency of a pulse changes with time, is important since the minimum pulse width for a given frequency bandwidth is found in wave packets with zero chirp or flat phase. The pulse spreading effect of GDD on an unchirped Gaussian pulse as it travels through a dispersive medium can be summarized by the following equation [31]:

$$\tau = \tau_o\left[1 + \left(4 \cdot ln2\frac{GDD}{\tau_o^2}\right)^2\right]^{1/2} \tag{6.8}$$

where τ is the FWHM of the broadened pulse in the time domain, while τ_o is the FWHM of the original undispersed pulse. Figure 6.8 uses equation 6.8 to show how the GDD broadening of femtosecond pulses at 808 nm changes according to input pulse width after traveling through 50 mm of BK7 glass. The parameters for the plot were chosen to coincide with the dispersion produced by the optics in the EPC experiment. The effect of GDD becomes great when ($GDD > \tau_o^2$). Control of only second order dispersion is usually sufficient when generating pulses on the order of 40 fs or longer, but higher order dispersion

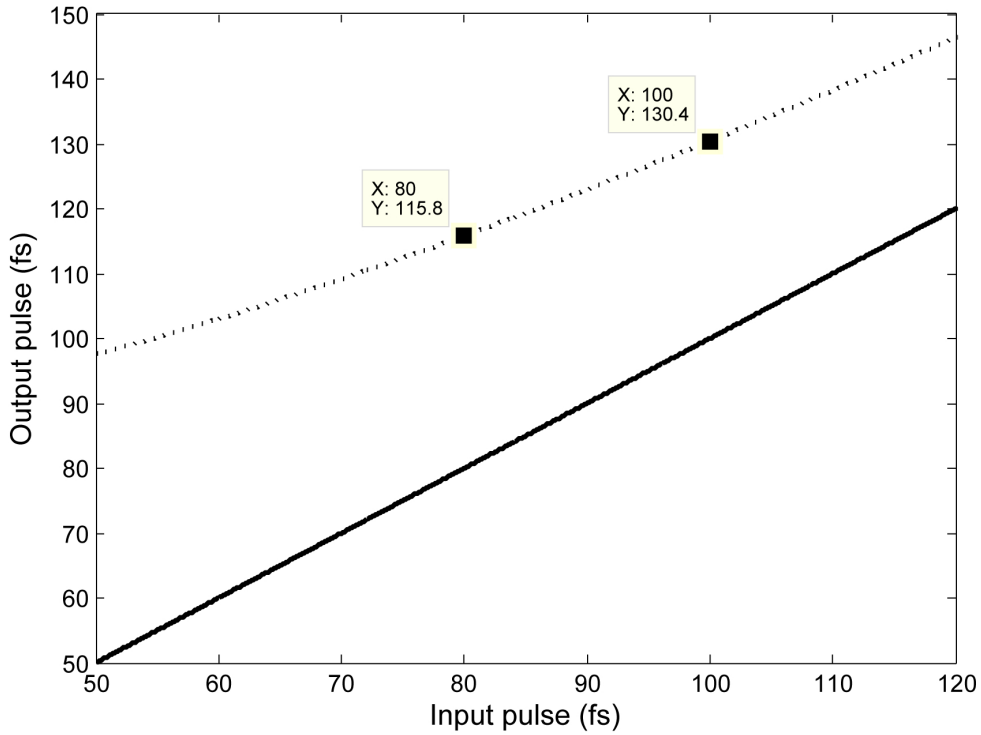

Figure 6.8: The effect of GDD on the width of an 808 nm Gaussian pulse before and after propagation through 50 mm of BK7 glass. A value of 50.6 fs^2/mm was used for the GVD and the effects of TOD were considered negligible at these pulse widths.

usually needs to be addressed in order to achieve pulse durations below this mark. Third order dispersion (TOD) or cubic dispersion ($\delta^3\phi/\delta\omega^3$), given in units of fs^3, becomes significant when TOD becomes greater than τ_o^3. For shorter pulse operation, higher orders dispersion such as quartic and quintic must also receive compensation.

Dispersion compensation

Dispersion compensation is a vital aspect of ultra-fast optics and this section will attempt to review the most prominent approaches. The most straight

forward way to limit dispersion is by minimizing the amount of dispersive material within the laser cavity or in the experimental design in the case of time resolved measurements. But since dispersive gain mediums and optics are part of most systems, methods of compensation have been developed.

Temporally short pulses being comprised of a broad band of frequencies can suffer from multiple orders of dispersion when propagating in matter, which results in pulse broadening in the time domain. Combinations of positively and negatively dispersive techniques are used to compensate for the accumulated group delay dispersion (GDD) in the pulse. The sign of the chromatic dispersion can be positive (normal) or negative (anomalous) in a single material and is smoothly dependent on frequency or wavelength. The point where the transition from normal to anomalous dispersion occurs is known as the zero dispersion wavelength, and the region surrounding this point sees only weak dispersive broadening. Consider a dispersion shifted optical fiber, where the zero dispersion wavelength is near 1550 nm. The telecommunications industry has engineered a global fiber-optic network that takes advantage of the low dispersion surrounding this point. All the wavelengths shorter than 1550 nm undergo positive dispersion while longer wavelengths see negative. Although the zero dispersion point is different for different materials, this trend remains, and methods for compensation have been developed for most cases.

A properly designed compensation system operating in the near IR will add just the right amount of negative dispersion to couteract the positive dispersion acquired from the transparent optical components in a laser system such as gain mediums, nonlinear crystals, and output couplers. Varying schemes can be utilized to control GDD and for pulse compression in solid state lasers most often utilizing prism sequences and/or chirped mirrors.

The most common form of dispersion compensation is through the use of Brewsters angle prism sequences and is the method used on the optical parametric oscillator and the equal pulse correlation pump-probe method desribed in this work. In this method, the prisms are comprised of a low loss material for the wavelength range of the optical system and are arranged to allow for adjustable dispersion. Prism pairs are generally restricted to the compensation of GDD but are an effective method which has been used to generate pulses as low as around 8.5 fs [32]. A typical configuration for this set-up is shown in figure 6.9. The first prism is used to refract the beam so that different optical

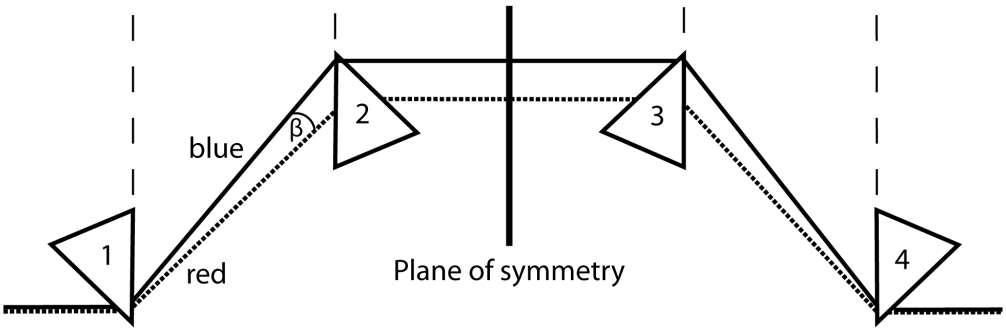

Figure 6.9: Diagram depicting a typical four prism dispersion compensation configuration. The longer dashed lines indicate the parallel faces of the prisms.

frequencies exit at different angles where they spread until reaching the second prism. The long wavelengths travel a shorter free space distance to reach prism 2 but popagate through more glass. The distance between prisms 2 and 3 does not effect GDD. Once the plane of symetry is reached, the pulse can be reflected back through 1 and 2 or progress through 3 and 4 where after the specified distance the frequencies are recombined. In short, this method relies on the dispersive nature of the prisms to adjust the optical path length that each frequency follows providing control over the pulse's GDD. The prisms are usu-

ally mounted on translational stages providing controll over the thickness of material in the beam (posative dispersion) for fine tuning of the total GDD. The negative GDD obtained from such systems is proportional to the prism separation and the GVD of the prism material. Calculations detailing the design of prism geometry are presented in section 6.4.

Chirped mirrors are another widely used method of compensation. Similar to other dielectric reflectors, chirped mirrors are based on quarter wave stacks but with slowly increasing layer thickness. As a result the longer wavelengths (lower frequencies) penetrate more deeply into the stack delaying them in relation to the more quickly oscillating wavelengths. The net result is negative dispersion tailored to the needs of a specific system and its compensation requirements [33, 34, 35]. A diagram depicting the basic concept is given in Figure 6.10. These mirrors have the added benefit of broader reflection bandwidth when

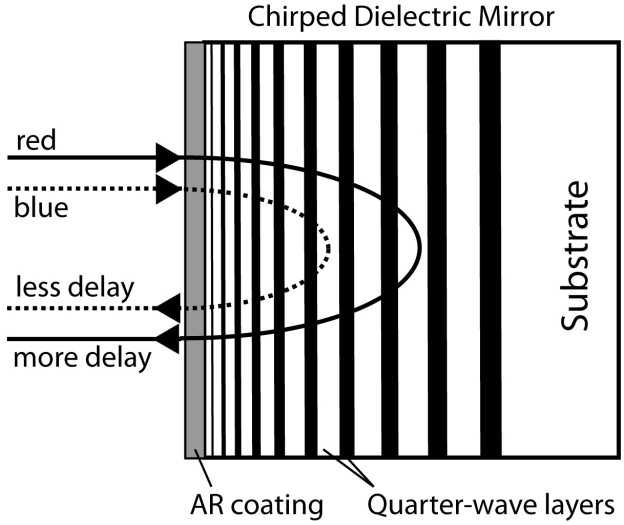

Figure 6.10: An illustration depicting the basic structure of a dispersion compensating chirped mirror. The quarter-wavelength layers are optimized to reflect chosen wavelengths as a function of penetration depth.

compared to standard mirrors. Although the idea appears straight forward, the design and implementation of chirped mirrors is complex and requires refined computer analysis. This is due to the difficulty in removing unwanted oscillations of the group delay as a function of frequency caused by reflections between the mirrors top coat and the structure beneath. Efforts to reduce the oscillations led to the design of double chirped mirrors (DCMs) which utilize advanced designs combined with an anti-reflective coating on the surface. The shortest pulsed ever directly generated from a laser, less than 6 fs FWHM, were obtained from a Ti:sapphire laser outfitted with DCMs [36, 37].

6.4 Dispersion Compensation in the EPC Set-up

Prism pairs were the obvious choice for external cavity dispersion compensation. The four prism sequence provided the means to conveniently adjust total GDD and to compensate for changes in the optical configuration as we exchanged lenses, filters, and beam splitters. The prisms also allowed for quick tailoring of the pulse width when testing the measurement apparatus. The design of the 4 prism dispersion compensator is covered in this section.

The Sellmeier equation is an empirical formula used to determine the wavelength dependent relationship of the index of refraction (n) for a given optical material. The standard form of the equation is given by [38, 39]

$$n(\lambda) = \sqrt{1 + \sum_j \frac{A_j \cdot \lambda^2}{\lambda^2 - B_j}} \tag{6.9}$$

where experimentally determined values known as Sellmeier coefficients (a_j and b_j) are input into the equation for calculations and λ is the wavelength given in μm. The coefficient values are readily available in the published literature in

A_1 = 1.69022361	B_1 = 0..130512113 μm^2
A_2 = 0.288870052t	B_2 = 0.061369188 μm^2
A_3 = 1.7045187	B_3 =149.517689 μm^2

Table 6.1: Sellmeier coefficients for SF-14 [SCHOTT Glass].

the form of tables, databases, and handbooks. A four SF-14 prism configuration was used to compensate for the dispersion created by the optics external to the laser cavity. Table 6.1 contains the Sellmeier coefficients for SF-14 that were used in the calculations. Six coefficients are typically sufficient for accurate results so that j=3 and equation 6.9 expands to read:

$$n(\lambda) = \sqrt{1 + \frac{A_1 \cdot \lambda^2}{\lambda^2 - B_2} + \frac{A_2 \cdot \lambda^2}{\lambda^2 - B_2} + \frac{A_3 \cdot \lambda^2}{\lambda^2 - B_3}} \tag{6.10}$$

Figure 6.11 shows how the index of refraction for SF-14 changes with wavelength as calculated with equation 6.10 and the coefficients listed in table 6.1. To reduce loss, the prisms are arranged at Brewster angles as detailed in previous sections. SF-14 was chosen for its large GVD which was needed to compensate for the significant amount of glass in the set-up. Some of the relevant optical properties of SF-14 and other common prism materials are displayed in table 6.4. The negative dispersion is a function of prism separation and is based on the geometry and spacing. The prism material itself does not produce negative dispersion but contributes to the total positive dispersion of the system which must be included in the calculations. The separation between the two center prisms does not affect dispersion so that only distances between prism 1-2 and 3-4 must be considered. The dispersion can be varied by adjusting the thickness of prism present in the beam by translating any of the prisms normal to its base

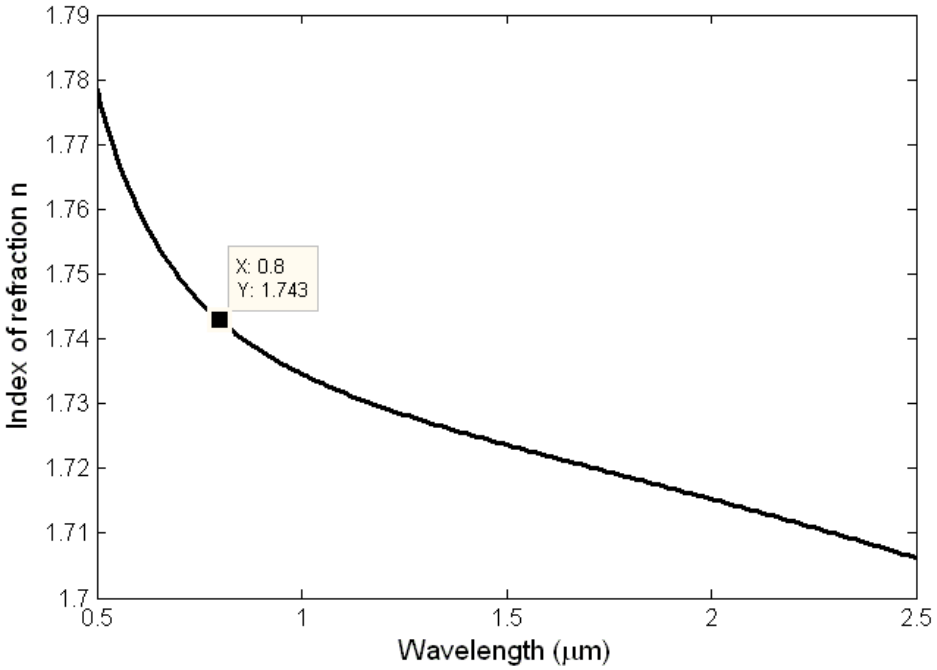

Figure 6.11: Sellmeier calculations of index of refraction versus wavelength for SF-14. The highlighted data point shows the approximate center wavelength of the pump laser.

[40]. This translation changes the magnitude of positive dispersion while the prism separation and thus the negative dispersion remain constant, providing the means to introduce the optimum amount of negative dispersion for minimum pulse width. The total negative dispersion introduced by the sequence as a function of prism separation is given by

$$GVD_{neg} = \frac{\lambda_c^3}{2\pi \cdot c^2 \cdot l_{ps}}\left(2\left(\left(\frac{d^2n}{d\lambda^2}\right) + \left(2n(\lambda_c) - \frac{1}{n(\lambda_c)^3}\right)\left(\frac{dn}{d\lambda}\right)^2\right)2W_r - 2l_{ps}\left(\frac{dn}{d\lambda}\right)^2\right) \quad (6.11)$$

Where λ_c is the center wavelength of the pulse, c is the speed of light, l_{ps} is the length of prism separation in each arm, and W_r is the beam radius at the prisms. The positive dispersion from the prisms themselves is related to the

Material	GVD (fs^2/cm)	TOD (fs^3/cm)	index n	θ_{Br}(deg)
SF-14	-113.5	-473	1.745	60.2
SF-10	-97.5	-388	1.711	59.7
Fused Silica	-16.5	-20	1.453	55.6
CaF_2	-5	-12	1.430	55.0

Table 6.2: OPtical properties of common prism materials [THOR Labs]

A1 = 1.03961212	B1 = 6.00069867 x $10^3 \mu m^2$
A2 = 0.231792344	B2 = 2.00179144 x $10^2 \mu m^2$
A3 = 1.01046945	B3 =1.0356065 x $10^2 \mu m^2$

Table 6.3: Sellmeier coefficients for borosilicate crown glass (BK7) [SCHOTT Glass].

second derivative of the index as

$$GVD = \frac{\lambda^3}{2\pi \cdot c^2 \cdot l_{ps}} \cdot \left(\frac{d^2 n}{d\lambda^2}\right) \cdot l_{mat} \tag{6.12}$$

where l_{mat} is the length of dispersive material in the beam. With an estimated 10 mm of SF-14 in the beam and a 1.1 mm beam radius, the positive GDD from the prisms was near 1764 fs^2. The positive dispersion form the optics located between the laser output and the sample, see figure 6.5, is calculated the same way using the Sellmeier coefficients for BK7 glass as listed in table 6.2. A plot of the index and wavelength for BK7 glass is shown in figure 6.12 Approximately 50 mm of glass was measured in this section with a calculated group delay dispersion of 2588 fs^2. The overall positive GDD is the sum of that from prisms and the

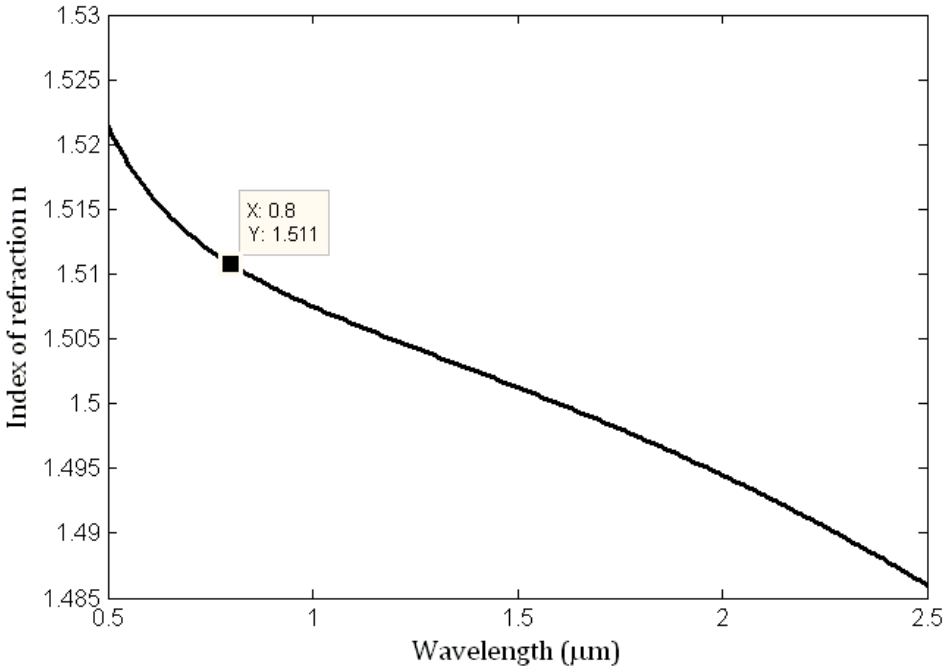

Figure 6.12: Sellmeier calculations of index of refraction versus wavelength for BK7 glass. The highlighted data point shows the approximate center wavelength of the pump laser.

glass optics totaling 4352 fs^2 requiring a prism separation of 27 cm in each arm to fully compensate the total GDD. The effect of residual GDD on pulse width is easily calculated with the following equations. The total GDD is the sum of the negative dispersion from prism separation, the positive dispersion from the prism material, and the positive dispersion from the optical glass (GDD_{total} = GDD_{neg} + GDD_{prism} + GDD_{optics}). The calculated value of total GDD should be close to zero when seeking short pulses since any residual GDD (both positive and negative) lengthens the pulse. The frequency span of the laser is given by

$$\Delta freq = 2\pi c \cdot \left(\frac{1}{\lambda_c - \Delta\lambda/2} - \frac{1}{\lambda_c + \Delta\lambda/2} \right) \tag{6.13}$$

where $\Delta\lambda$ is the pulse spectral wavelength bandwidth. This quantity is used to calculate the change in pulse width measured in fs.

$$\Delta PW = GDD_{total} \cdot \Delta freq \tag{6.14}$$

The length of the resulting dispersion compensated pulse is simply the length of the original plus the change in pulse width caused by residual GDD.

$$PW_{new} = PW_{original} + \Delta PW \tag{6.15}$$

Experimentally we were able to adjust the pulse width between 80-150 fs by tweaking the Ti:sapphire output and by translating the prism seperation. The MATLAB code used for the dispersione calculations is presented in appendix A.

6.5 Control of Pump/Probe Delay for the EPC Configuration

The piezoelectric scanner provided a stable scan range of 1.2 ps or 600 fs on each side of $\tau = 0$ and corresponds to a 300 μm movement of the corner cube. A 1 cm polarizing beam splitter was the least dispersive model available that provided a 1000:1 extinction ratio. A half wave plate ensured a balanced 50/50 ratio in each polarization. A non polarizing beam splitter was occasionally used to take interferometric autocorrelations as seen in figure 6.13 which were used to accurately align and test the interferometer.

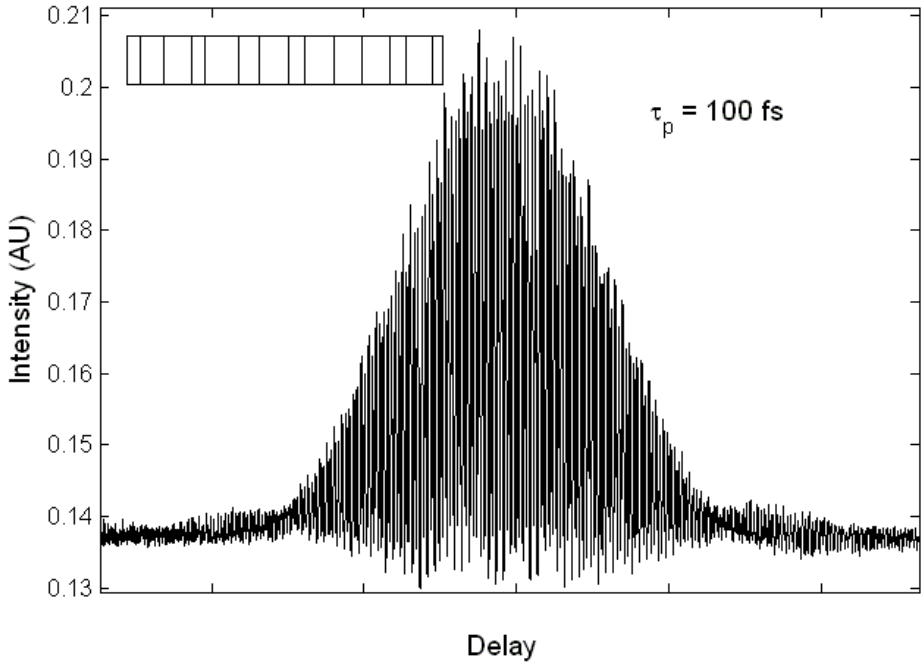

Figure 6.13: An interferometric AC of the pump at λ = 800nm and a pulse width of 100 fs.

6.6 Collinear Pump Probe Geometry

A collinear geometry was used for the EPC measurements where both pulses contribute to the measured transmitted intensity. Figure 6.14 shows the basic configuration. Recall that EPC requires that the pulses be of equal intensity so that $I_{combined} = I_1 f(t) + I_2 f(t - \tau_d)$, where in this case f(t) represents a Gaussian pulse shape ($f(t) \propto \exp[-8ln2(t/T_p)^2]$). Under normal conditions, where no saturation is observed, the sum of the transmitted beams (measured at detector D1) remains constant as the relative delay between pulses is swept (τ). This assumes an integration time for the detector that is much greater than the temporal pulse separation. In general, both pulses contribute equally to the generation of excited carriers within the sample, but in the presence of absorption saturation, the

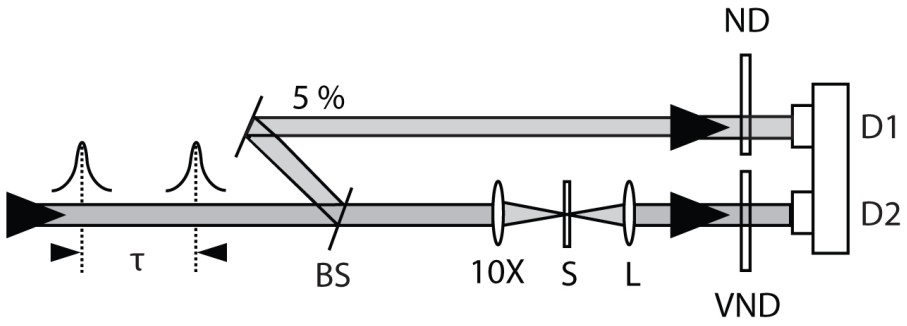

Figure 6.14: An interferometric AC of the pump at λ = 800nm and a pulse width of 100 fs. The inset at the top left shows a close-up of the sharp interference fringes.

combined transmission is increased resulting in an observed TCP. The FLG on quartz samples were mounted on a three dimensional translational stage so that high quality portions of the material could be precisely aligned. The best results were obtained for samples with approximately 16 % absorption. A variable ND filter made it easy to balance the signals on D1 and D2. Balanced detection was used to remove common mode noise and for its ability to detect small signals on a large DC background. When properly balanced, the DC signal is canceled (D1-D2) and only the AC component is amplified. The detector was comprised of two well-matched pairs of 5 mm diameter Si PIN photodiodes. This difference signal was averaged on a digital oscilloscope and the captured waveform was used in the computer based signal analysis.

6.7 Graphite and Graphene

Carbon has been a subject of great interest throughout much of scientific history and is currently the focus of intense global research in the form of

fullerenes; consisting of graphene, carbon nanotubes, and carbon buckyballs. These recently discovered materials are polymorphs of carbon, as are graphite and diamond, which posses different crystal structures and radically different material properties. Graphene is the strongest and stiffest material ever measured, yet it is the most stretchable crystal known, it possesses the largest area to weight ratio of any known substance, and has electronic and optical properties that could revolutionize future technology [41]. This section reviews the physical structures of graphite and graphene and the characteristics that make them unique.

Graphene is the most basic form of the sp^2 carbon systems and consists of a single atomic layer of graphite arranged in planar sheets of hexagonal structure. The unit cell consists of two carbon atoms as depicted in the insert of figure 6.15. Each atom is covalently bonded to three others in the basal plane resulting

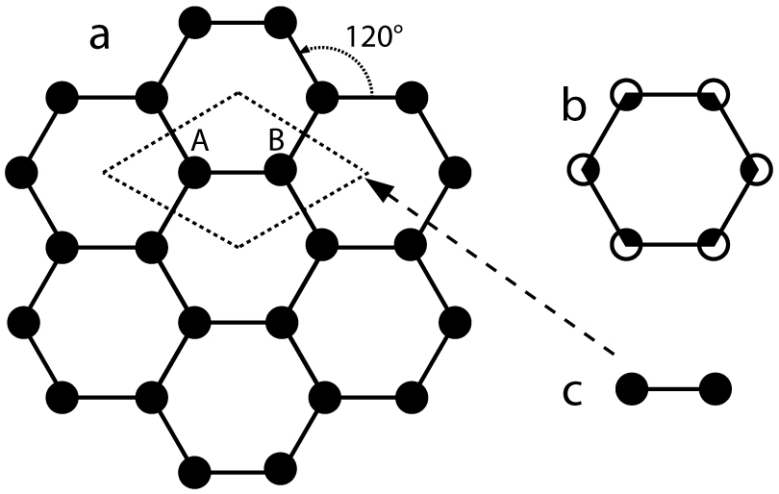

Figure 6.15: Diagram depicting the hexagonal structure of graphene where A and B represent individual carbon atoms. a. Hexagonal lattice and unit cell arrangement, B. Unit cell structure containing 1/3 of six atoms. c. Unit cell structure containing two whole atoms.

in bond strengths greater than that of diamond. Individual layers of graphite share the same structure as graphene with the layers or sheets held together by relatively weak van der waals forces in the Bernal (ABABAB) stacking configuration. The atoms have a nearest neighbor separation within a layer of 1.42 A while the separation between the planar layers is 3.35 A [42]. The relationship between stacked layers is shown in figure 6.16.

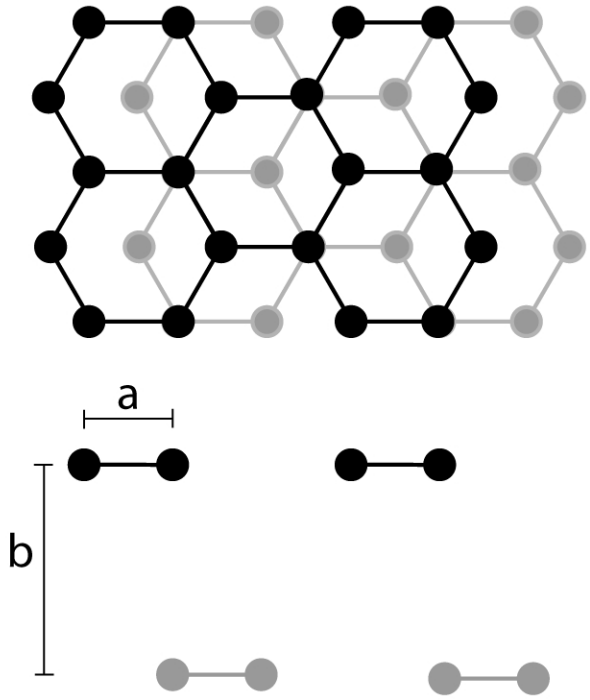

Figure 6.16: Diagram showing the ABAB stacking structure found in graphite in relation to individual graphene layers. The upper portion is a top view and the lower shows the layer configuration and relative distances. Letter a designates the nearest neighbor atomic distance of 14.2 nm while b signifies the 33.5 nm layer separation.

The electron configuration of carbon is $1s^2 2s^2 2p^2$ with four electrons in the outermost shell. The carbon atoms in graphite encompass an sp^2 hybridization resulting in a linear combination of 2s and 2p orbitals with strongly directional bonds, see figure 6.17. Sigma bonds (sp^2) with the three nearest neighbors are

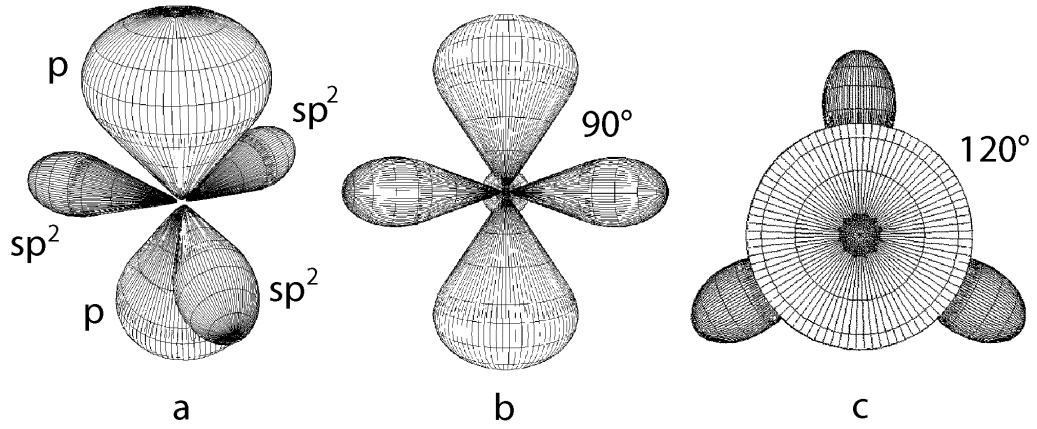

Figure 6.17: Authors illustration of the hybrid sp^2 orbital configuration of carbon. a: arbitrary viewpoint, b: side view, c: top view.

responsible for the hexagonal structure while the overlap of 2p orbitals produce pi bonding within the sheet. The weakly bound π orbital electrons contribute to graphites conductivity. Both graphite and graphene posses the properties of a semiconductor with a vanishing bandgap at the k = 0 point and also retain the properties of a metal with a vanishing Fermi surface, and as such, rest on the edge between metal and semiconductor behavior. This is due to the hybridized bonding mentioned earlier. The in-plane sigma bonding and strong atomic potentials normally result in a large bandgap, but since the $2p_z$ orbitals which extend perpendicular to this plane in both the positive and negative z directions contact the neighboring $2p_z$ orbitals at the Fermi energy, the bandgap is essentially bypassed. Figure 6.18 provides a conceptual drawing of the σ and π bond orientation. The valence and conduction bands can be visualized as cones that intersect at the Dirac point, or at the six points of the Brillouin zone.

Highly ordered pyrolytic graphite (HOPG) is a commercially available, extremely pure form of graphite with exceptional crystal properties, exhibiting mosaic angles as low as 0.4 +/- 0.1. HOPG is a lamellar material and has excep-

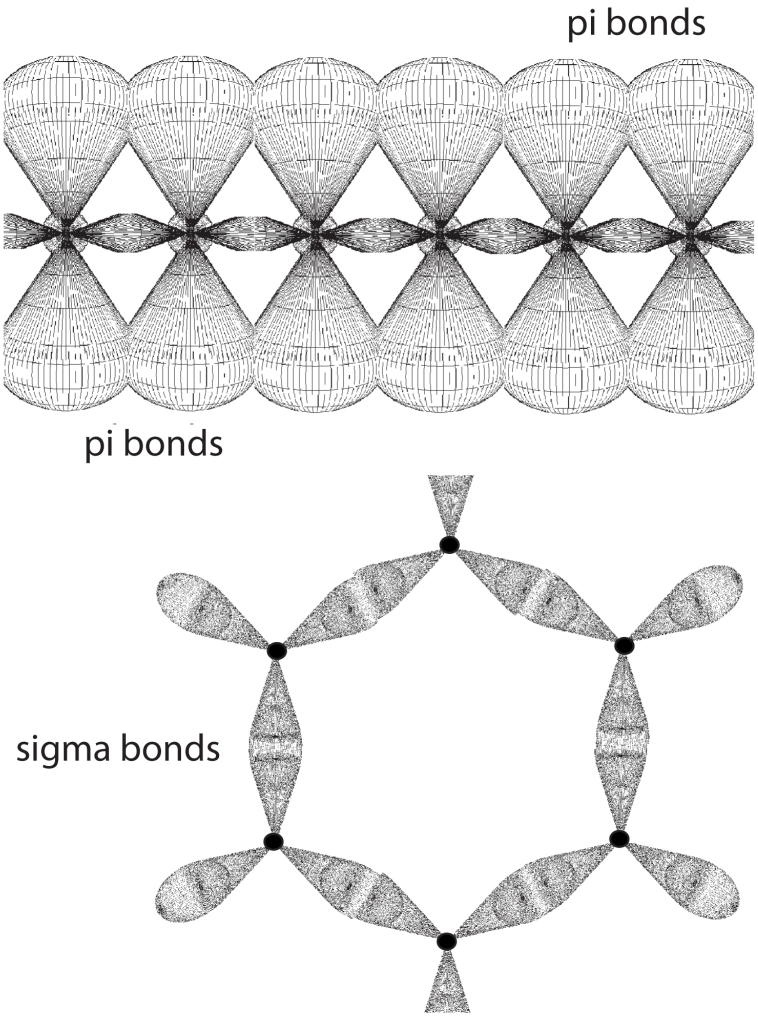

Figure 6.18: The authors conceptual illustration of sigma and π bonding in graphene. The π bonding which takes place both above and below the central plane is responsible for graphenes electronic properties. The sigma bonds lie between the nuclei and give graphene its rigidity.

tionally flat cleavage planes due to its well ordered crystal structure when compared to normal graphite. HOPG can be reduced to films of graphene through mechanical cleaving and transferred to a desired substrate. The number of layers can be verified or at least estimated using three common procedures. First,

and perhaps the least accurate, is through measurement of optical absorption. Graphene has broadband spectral absorption with approximately 2.3 percent absorption per layer, allowing an estimation of film thickness through optical transmission measurements. The second method uses an optical microscope to detect variations in color and transparency that are indicators of thickness. Single layers appear as purple translucent flakes with areas of uniform color. Raman spectroscopy is a third method of determining layer count. Graphene's Raman spectrum is characterized with two sharp peaks, known as the G (1585 cm^{-1}) and G (2700 cm^{-1}) bands [43]. The G feature is derived from the oscillation of in-plane covalent bond lengths between nearest neighbors while the G' feature is related to the breathing of the hexagonal lattice rings. The G band spectrum is nearly independent from the number of layers but the G' band demonstrates predictable changes in the number of peaks with changes in feature thickness. These variations provide the means to determine the number of graphene layers [44] and their stacking order [45] in FLG samples.

6.8 Sample Preparation

The samples were mechanically cleaved from highly ordered pyrolytic graphite (HOPG) with a mosaicity of 0.4+/-0.1 and mounted on a quartz substrate. The mosaic spread is a measure of crystalline order, where a lower number indicates a highly ordered atomic structure. High quality HOPG demonstrates superb cleavage producing smooth surfaces with virtually no steps. The bulk HOPG used in this work was ZYA grade purchased from SPI supplies and its quality was verified by the supplier using X-ray diffraction. Mechanical cleavage of HOPG is currently the most utilized and successful method of pro-

ducing FLG and graphene sheets [46]. The adhesive tape method [47, 48] was used here and the samples were transferred to the substrate by pressure and release. This method has been shown to produce single layer graphene flakes up to millimeters in size [4] but suffers from low yield and scalability. Samples with approximately 16% absorption were used for testing corresponding roughly to 6-8 layers of graphene assuming 2.3% absorption per layer [4]. A modulation in the absorption depth of near 1.4% was observed in the samples from partial saturation due to Pauli blocking.

6.8.1 Electronic properties of graphene

As previously addressed, the sp^2 hybrid bonding gives graphene it's unique structural and electronic properties. This section takes a closer look at graphenes orbital and electronic structure and how this relates to its electronic band structure.

The sp^2 hybridization in graphene contains four linear combinations of s and p atomic orbitals that organize themselves into σ and π bonds as detailed below [43] and as shown graphically in figure 6.19.

$$|\, sp_1^2\rangle = \sqrt{\frac{1}{3}}\,|\, s\rangle + \sqrt{\frac{2}{3}}\,|\, p_x\rangle \tag{6.16}$$

$$|\, sp_2^2\rangle = \sqrt{\frac{1}{3}}\,|\, s\rangle - \sqrt{\frac{1}{6}}\,|\, p_x\rangle + \sqrt{\frac{1}{2}}\,|\, p_y\rangle \tag{6.17}$$

$$|\, sp_3^2\rangle = \sqrt{\frac{1}{3}}\,|\, s\rangle - \sqrt{\frac{1}{6}}\,|\, p_x\rangle - \sqrt{\frac{1}{2}}\,|\, p_y\rangle \tag{6.18}$$

$$| sp_4^2\rangle = | p_z\rangle \tag{6.19}$$

where each of the three σ orbitals is constructed from a combination of 1/3 of an s electron plus 2/3 of a p electron while the fourth orbital is strickly p type extending in the z directionand and is responsible for the π bonds.

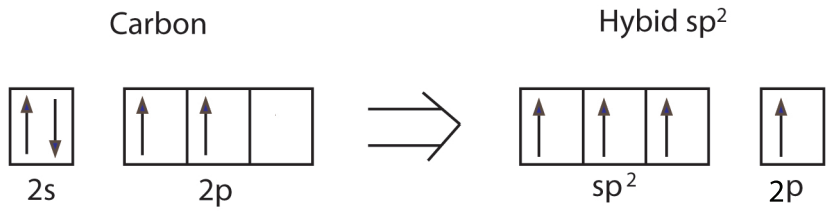

Figure 6.19: A block diagram depicting the band filling of an sp^2 hybridized system.

The covalent c-c bonds (σ) in the honeycomb structure of graphene are very strong at 6.3 eV [49]. They give graphene its ridged mechanical properties and superb thermal conductivity with little or no effect on its electronic transport properties assuming a planar unfolded surface. The σ bonds are located between the nuclei of neighboring carbon atoms at 120 degree intervals forming the familiar honeycomb lattice and each contain 1/3 of an s electron and 2/3 of a p electron.

The π bonds are comprised of one strictly p type electron and extend perpendicular to the σ bound honeycomb plane in both the positive and negative p_z directions where they overlap with adjacent π orbitals. The overlap allows electrons to jump from one atom to the next at the extremely fast rate of about 1 x 10^{15} transitions per second so that the electrons are not associated with a single host atom. The electrons are essentially free to travel parallel to the graphene sheets through the network of π bonds which are responsible for the materi-

als electronic properties. The p electrons of the π orbitals oscillate within the p_z lobes above and below the atomic nucleus perpendicular to the basil plane. When this oscillation is in phase with a neighboring π orbitals oscillation, they form an attractive bonding relationship but when they are 180 degrees out-of-phase, they form a repulsive one, each respectively know as the bonding (π) and antibonding (π*) configurations. These cases represent the two extremes and it is important to understand that any phase relationship between the neighboring and partially overlapping wave functions is possible. Each electron is a wave that extends over the entire plane of the graphene with specific values for amplitude and phase at each location. The total energy of the electron wave is the sum of energies at each bond where in-phase relationships have negative energy while out-of-phase relationships have positive energy. Certain phase and amplitude configurations result in electron waves with a total energy of zero which define the Fermi surface of graphene where the energy bands of the (π) and (π*) bands intersect and sum to zero.

The velocity of an electron in matter is typically dependent on electron energy which results in an effective mass for the particle different than that of a free electron. The velocity of electrons in graphene is independent of electron energy as a result of the (π) bonds and behaves more like a photon giving the electron a massless behavior [50]. The momentum of a π electron is given by: P=hk/2pi where h is Planks constant and k is the electron wavenumber. When propagating in the x direction each π or $\pi*$ election possesses energy of: E=+/-hν(1+2cos(kd/2)) where, ν is the electron frequency and d is the graphene lattice constant of 0.26 nm [43]. The minus value for energy corresponds to π while the positive relates to $\pi*$ bonding. The electron wave energy is zero where the two band cross or when K=k=+ 4π/3d and K′=k=+ 4π/3d [51]. A traveling elec-

tron wave in an infinite sheet of graphene is interesting since it behaves like a Boson in that it has a dispersion relation similar to a photon with a non-energy dependent velocity and quasi-massless behavior. None-the-less, electrons are Fermions and subject to the Pauli exclusion principle which directs graphenes band filling process.

The electrons fill the π and $\pi*$ bands with one valence electron donated from each atom beginning with the lowest available energy levels and filling the bands until all the carbon atoms in the sheet have contributed and the crystal is neutrally charged. It is at this point that the bands are filled to the Fermi energy level which is in this case perfectly equal to the K and K′ energy also known as the Dirac point. In single layers of graphene the two bands show identical linear dispersions so that the energy of the electron changes linearly with momentum. The result is a semimetal that acts like zero-bandgap semiconductor with a linear dispersion relationship for both electrons and holes [52, 53], regardless of the direction of travel within the plane [54]. Many of graphite and graphenes transport properties can be understood through this model of band structure. The nearly unbound electrons in the overlapped π bonds are free to move under the force generated by an electromagnetic field where they hop between filled and unfilled energy levels.

The optical absorption in graphene is dependent on the density of states corresponding to the energy of the incident photon. Absorption is maximized for a given wavelength when the difference between occupancies in the valence and conduction bands is maximized. The generation of photoexcited carriers fills energy states in the conduction band while depleting the density in the valence band at energies equal to $\hbar\omega/2$ on either side of the Dirac point effectively reducing the difference and increasing the transparency through partial satura-

tion.

6.8.2 Carrier Dynamics in graphene

The ultrafast carrier dynamics in graphite and graphene are regulated by carrier-carrier interaction and carrier-phonon coupling. The electrons and holes relax in similar ways due to the symmetric band structure where the probabilities of occupation are related $f_e(E)=f_h(-E)$, Through the use of mode locked lasers, optically excited electron-hole plasmas can be generated within a sample and then probed to watch their return to the pre-perturbed state. Time resolved measurements of these relaxations shed light on the internal mechanisms that govern these processes. Photoexcitaion from an optical pulse fills the states in the conduction band with electrons having a narrow energy distribution as depicted in figure 6.20. Immediately after absorption, this narrowly packed non-equilibrium distribution broadens as the energies migrate toward an equilibrium state through carrier-carrier scattering. It begins as the newly excited carriers loose coherence with the generating field and between themselves as they move towards a Fermi-Dirac like distribution. This ultrafast broadening process takes place within tens of femtoseconds and reduces the density of carriers centered at the absorption peak thereby increasing the number of available absorption states. It is this process that is responsible for the initial relaxation of the transparency and it ends as a hot electron gas that must cool through phonon emission. The slightly slower relaxation time that follows is attributed to carrier-phonon coupling resulting in a transfer of energy to the lattice. This intraband cooling occurs in few layer graphite on a 100 femtosecond timescale followed by electron-hole recombination in the picoseconds regime [55].

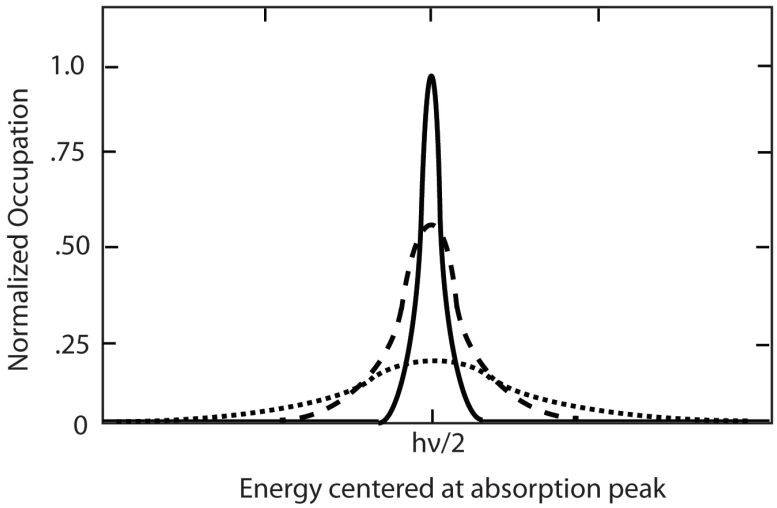

Figure 6.20: Caption: A graphic depiction showing the evolution of the initially narrow photogenerated carrier distribution. The solid line represents the athermal starting distribution while the dashed lines show the broadening effect of carrier-carrier scattering. The effects of carrier-phonon coupling are not shown for clarity.

6.9 Results

A recursive linear least squares fit algorithm was used to find time constants and amplitudes of exponential decays present in the experimental data. The numerical values of the time constants were extracted from the results by fitting the convolution of the pulse autocorrelation and the double sided exponentials (representing τ_1 and τ_2) to the TCP signal. Typical experimental TCP scans and their corresponding intensity autocorrelations are shown in figure 6.21. The least squares fit algorithm detected two time constants in the saturation broadened TCP signals. The results suggest an initial extremely fast relaxation of 15 ± 10 fs followed by a slower relaxation on the order of 175 ± 30 fs. Theoretical simulations of the ECP technique were used to gain insight into the measurement uncertainties. The experimental resolution of the faster relaxation (τ_1) is

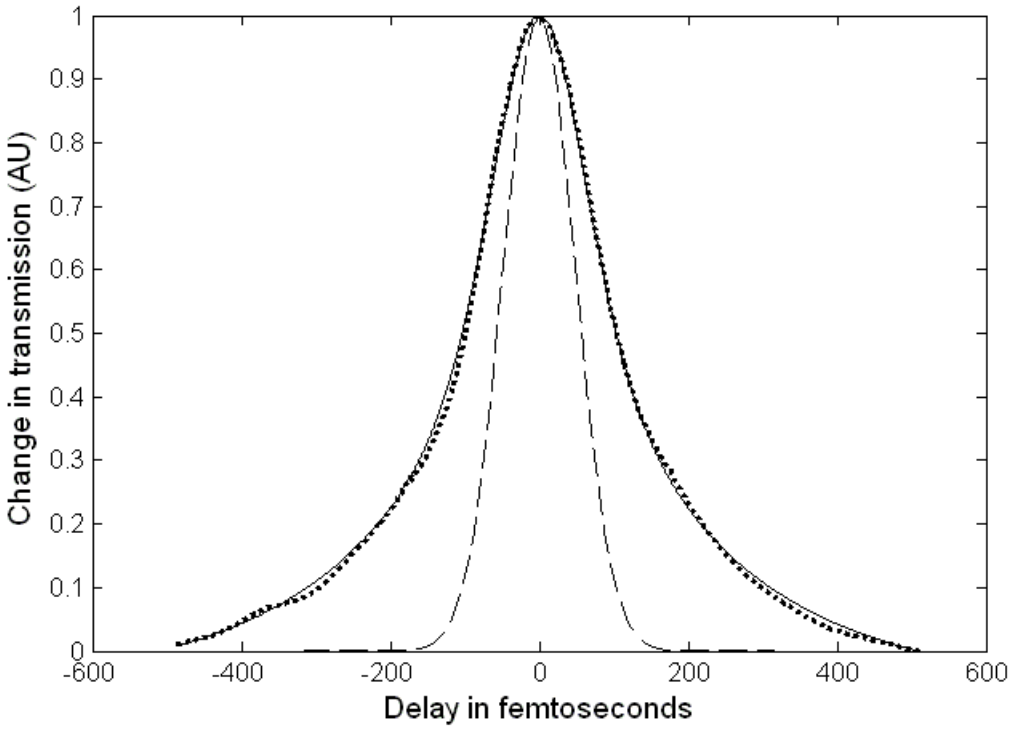

Figure 6.21: Comparison of the intensity autocorrelation (long dashes) of an 80 fs pulse and the corresponding TCP (dotted). The solid line represents the theoretical curve fit utilizing two time constants

near 20 fs and is based on both the noise levels in our data and on the extreme sensitivity in matching the exponential decays to the data. We have limited the experimental resolution of the slower relaxation (τ_2) to 60 fs based on a higher standard deviation caused by experimental noise in the tails of the TCP where τ_2's signature is most prominent.

The generation of photoexcited carriers fills energy states in the conduction band while depleting the density in the valence band at energies equal to $\frac{h\nu}{2}$ on either side of the Dirac point effectively reducing transparency through partial saturation. This experiment used an 800 nm or approximately 2.5 x10^{-19} J/photon pump energy corresponding to 1.25 x10^{-19} J above and below the

Dirac point. This narrowly packed non-equilibrium distribution broadens as the energies migrate toward a Fermi-Dirac like distribution. The ultrafast carrier dynamics in graphite are regulated by carrier-carrier interaction and carrier-phonon coupling with the tightly bound lattice of the basal planes. Immediately after absorption, the newly excited carriers lose coherence with the generating field and themselves as they thermalize under carrier-carrier collisions resulting in a spread of energy centered on the photon excitation level. We believe that the measured fast relaxation time of 15 ± 10 fs corresponds to this carrier-carrier interaction. The slightly slower relaxation time of 175 ± 30 fs is attributed to carrier-phonon mediated intraband cooling of electrons and holes. Recently published simulation results based on Boltzmann equations [15] support these findings and infer that hot phonons which played a negligible role in early relaxations become prevalent after approximately 100 fs. Finally, as the carriers relax to near the band extrema within a few hundred fs, they are subject to electron-hole recombination on a much longer ps timescale.

In summary, we have investigated the ultrafast relaxation of photoexcited carriers in thin films of mechanically cleaved HOPG using the equal-pulse correlation technique. Experimental results were analyzed using linear least squares fitting to extract the time constants and amplitudes of exponential decays form the data. A modulation depth of near 1.4% was observed in the samples due to a partial saturation caused by Pauli blocking. Decay times much less than the temporal pulse width of the laser were resolved through careful control of noise using a balanced detection system and by extensive averaging of the TCP signal. The results suggest a fast relaxation of 15 ± 10 fs caused by intraband carrier-carrier thermalization followed by a slower relaxation on the order of 175 ± 30 fs attributed to carrier-phonon interactions with the lattice. The EPC

technique was validated as an effective method to extend the measurement range of pump-probe systems to measure events much shorter than the laser pulse for materials with overlapping relaxation processes. The results reinforce graphene's potential for use as saturable absorbers in mode-locked lasers and ultra-fast optical systems.

6.9.1 Graphene as a saturable absorber in mode-locked lasers

Solid state lasers remain the backbone of ultrashort pulse generation with broad relevance in research, industry, manufacturing, commerce, and medical applications. These ultrafast lasers often employ saturable absorbers as the means of mode-locking through self absorption modulation. The net transmission of an absorbing element can be given by [56]

$$T = 1 - exp(-\sigma(\omega)l(N_1(t) - N_2(t)) \tag{6.20}$$

Where $\sigma(\omega)$ is the frequency dependent absorption cross section, l_a is the absorber thickness, and $N_1(t)$ and $N_2(t)$ are the populations of the lower and upper absorption transition levels respectively. Since the density of absorption sites is fixed within the material, we assume a limited supply of available absorption states so that N_o=N_1+N_2 in $(absorbers/cm^3)$. Initially, all the carriers are in the ground state and (N_1-N_2) is at its largest value, resulting in maximum absorption. But as the ground state population is optically excited from N_1 to N_2, the transmition increases until at the theoretical limit N_1=N_2, the transmition reaches 100%.

The desired material properties of a universal saturable absorber are a fast response time and recovery, broadband optical absorption, high damage

threshold, low saturated loss, and ease of implementation. Most saturable absorbers are currently based on semiconductor technology in the form of semiconductor saturable absorber mirrors or SESAMs [57, 58], but these are complex devices with relatively narrow tuning range [59, 60] over which graphene could offer many advantages.

Graphene displays many of the qualities desired in a passive mode-locking element and is an ideal candidate for a universal, ultrabroadband, ultrafast saturable absorber. Normally grown semiconductor materials have relaxation times on the order of nano-seconds and advanced low temperature growth III-V techniques utilizing defect carrier traps, has pushed this into the single to tens of ps range [57]. We have reported phonon related recovery times in FLG within the 100 fs regime. This represents a tenfold reduction in recovery times as compared to the latest semiconductor saturable absorbers which is especially relevant in fast absorber mode-locking [61].

In addition, the broadband nature of graphene removes the need for the bandgap engineering required of semiconductor materials. Similar to equation 6.20 the linear optical absorption of graphene can be approximated by applying the Fresnel equations in the thin film limit and assuming a material with a fixed universal optical conductance [62, 63]. The optical conductance of single layer graphene ($G_o = e^2/4\hbar$) is related to the fine structure constant (α) so that

$$\alpha = \frac{e^2}{\epsilon_o \hbar C} = \frac{G_o}{\pi \epsilon_o C} \tag{6.21}$$

where e is electron charge. The unsaturated transmittance can then be given by

$$T = (1 + 0.5\pi\alpha)^{-2} \approx 1 - \pi\alpha \approx 97.7\%. \tag{6.22}$$

The experimentally measured absorption spectrum of exfoliated graphene matches well with theory and is relatively flat between 200-2500 nm with approximately 2.3% absorption per layer from the infra-red through the visible

spectrum [4]. Single-walled nanotubes (SWNT) have also recently demonstrated utility as a saturable absorber [64], but since their resonant absorption frequencies are related to tube diameter, they involve close dimensional controls. SWNT absorbers with broad spectral bandwidth [65] require a vast range of diameters to ensure a flat response while unwanted diameters result in optical loss. Graphene offers a flat optical response and cost effective fabrication without the material engineering restraints found in semiconductors and SWNTs. Graphenes high damage threshold and absence of two photon absorption make it a candidate for high energy short pulse applications. Epitaxially grown samples were shown to have a single shot damage thresholds near $5x10^{10}Wcm^{-2}$ for 50 fs pulse duration [66]. Persistent laser damage thresholds were investigated with an erbium-doped fiber laser mode-locked with atomic layer graphene and endurance tested for over 140 hours subjecting the sample to an optical fluency of 52 mJ/cm^2 with no degradation to mode-locked performance [67]. Graphene also offers advantages in the area of unwanted optical loss. The thin nature of graphene reduces scattering losses which can be significant under the high optical intensities found in a laser cavity. Also, graphene reflects less than 0.1 % of the visible light incident on a single layer and only ~ 2 % at ten layers [68].

The in plane sigma bonding and strong atomic potential that gives graphene its unmatched strength and resilience normally produces materials with large bandgaps, but fortunately, the hybridized bonds in graphene give this remarkable material both the structural and optical properties desired in a saturable absorber. The demonstrated extremely fast recovery time, broadband absorption, and high damage threshold found in graphene and FLG make them potential materials for a universal saturable absorber that could simplify and reduce de-

sign costs making ultrafast pulsed system availible to a new demographic of reaserchers worldwide.

BIBLIOGRAPHY

[1] K. S. Novoselov A. K. Geim. The rise of graphene. *Nature Materials*, 6:183–191, 2007.

[2] Q. Bao, H. Zhang, Y. Wang, Z. Ni, Y. Yan, Z. X. Shen, K. P. Loh, and D. Y. Tang. Atomic-layer graphene as a saturable absorber for ultrafast pulsed lasers. advanced functional material. *Advanced Functional Materials*, 19:30773083, 2009.

[3] A. F. Bello, D. J. Erskine, and H. B. Radousky. Separating the coherent and incoherent effects in optical correlation experiments on semiconductors and other saturable absorbers. *Review of Scientific Instruments*, 67:503, 1996.

[4] F. Bonaccorso, Z. Sun, T. Hasan, and A. C. Ferrari. Graphene photonics and optoelectronics. *Nature Photonics*, 4:611–622, 2010.

[5] Markus Breusing, Claus Ropers, and Thomas Elsaesser. Ultrafast carrier dynamics in graphite. *Phys. Rev. Lett.*, 102(8):086809, Feb 2009.

[6] Won Bae Cho, Hwang Woon Lee, Sun Young Choi, Jun Wan Kim, Dong-Il Yeom, Fabian Rotermund, Jinho Kim, and Byung Hee Hong. Monolayer graphene saturable absorber for bulk laser mode-locking. In *Conference on Lasers and Electro-Optics*, page JThE86. Optical Society of America, 2010.

[7] S. B. Hubbard, T. J. Kershaw, A. Usher, A. K. Savchenko, and A. Shytov. Millikelvin de haas–van alphen and magnetotransport studies of graphite. *Phys. Rev. B*, 83(3):035122, Jan 2011.

[8] J. Jiang, R. Saito, A. Gruneis, G. Dresselhaus, and M. Dresselhaus. Electron phonon interaction and relaxation time in graphite. *Chemical Physics Letters*, 392:383–389, July 2004.

[9] Tobias Kampfrath, Luca Perfetti, Florian Schapper, Christian Frischkorn, and Martin Wolf. Strongly coupled optical phonons in the ultrafast dynamics of the electronic energy and current relaxation in graphite. *Phys. Rev. Lett.*, 95(18):187403, Oct 2005.

[10] Y. Kopelevich and P. Esquinazi. Negative c-axis magnetoresistance in graphite. *Adv. Mater.*, 19:4559, 2007.

[11] Ryan W. Newson, Jesse Dean, Ben Schmidt, and Henry M. van Driel. Ultrafast carrier kinetics in exfoliated graphene and thin graphite films. *Opt. Express*, 17(4):2326–2333, Feb 2009.

[12] Richard Van Noorden. Moving towards a graphene world. *Nature*, 442:228–229, July 2006.

[13] S. L. Palfrey and T. F. Heinz. Coherent interactions in pump-probe absorption measurements: the effect of phase gratings. *J. Opt. Soc. Am. B*, 2:674–679, 1985.

[14] A. Reina, J. Ho X. Jia, D. Nezich, H. Son, V. Bulovi?, M.S. Dresselhaus, and J. Kong. Large area, few-layer graphene films on arbitrary substrates by chemical vapor deposition. *Nano Letters*, 9:30–35, 2009.

[15] M. J. Rosker, F. W. Wise, and C. L. Tang. Femtosecond relaxation dynamics of large molecules. *Phys. Rev. Lett.*, 57(3):321–324, Jul 1986.

[16] K. Seibert, G. C. Cho, W. Kütt, H. Kurz, D. H. Reitze, J. I. Dadap, H. Ahn, M. C. Downer, and A. M. Malvezzi. Femtosecond carrier dynamics in graphite. *Phys. Rev. B*, 42(5):2842–2851, Aug 1990.

[17] Tze Chien Sum, Guichuan Xing, Cheng Hon Alfred Huan, Hongchen Guo, and Xinhai Zhang. Probing ultrafast carrier-carrier scattering dynamics in epitaxial graphene. In *Lasers and Electro-Optics (CLEO) and Quantum Electronics and Laser Science Conference (QELS), 2010 Conference on*, pages 1 –2, May 2010.

[18] W. D. Tan, C. Y. Su, R. J. Knize, G. Q. Xie, L. J. Li2, and D. Y. Tang. Mode locking of ceramic nd:yttrium aluminum garnet with graphene as a saturable absorber. *Applied Physics Letters*, 96:031106, 2010.

[19] C. L. Tang and D. J. Erskine. Femtosecond relaxation of photoexcited nonequilibrium carriers in $al_xga_{1-x}as$. *Phys. Rev. Lett.*, 51(9):840–843, Aug 1983.

[20] A. J. Taylor, D. J. Erskine, and C. L. Tang. Equal pulse correlation technique for measuring femtosecond excited state relaxation times. *Applied Physics Letters*, 43(11):989 –991, December 1983.

[21] H. Wang, J. H. Strait, P. A. George, S. Shivaraman, V. B. Shields, Mvs Chandrashekhar, J. Hwang, C. S. Ruiz-Vargas, F. Rana, M. G. Spencer, and

J. Park. Ultrafast relaxation dynamics of hot optical phonons in graphene. *Applied Physics Letters*, 96:081917, 2010.

[22] J. E. Bair, D. Cohen, J. P. Krusius, and C. R. Pollock. Femtosecond relaxation of carriers generated by near-band-gap optical excitation in compound semiconductors. *Phys. Rev. B*, 50(7):4355–4370, Aug 1994.

[23] M. J. Rosker, F. W. Wise, and C. L. Tang. Femtosecond relaxation dynamics of large molecules. *Phys. Rev. Lett.*, 57(3):321–324, Jul 1986.

[24] Steve Smith, Niels Christian Roemer Holme, Brad Orr, Raoul Kopelman, and Ted Norris. Ultrafast measurement in gaas thin films using nsom. *Ultramicroscopy*, 71(1-4):213 – 223, 1998.

[25] A.J. Taylor, D.J. Erskine, and C.L. Tang. Femtosecond vibrational relaxation of large organic molecules. *Chemical Physics Letters*, 103(5):430 – 435, 1984.

[26] Sands Faynman, Leighton. *The Feynman Lectures on Physics*. Addison-Wesley Publishing Company, the definitive edition edition, 1977.

[27] Helmut Rechenberg Jagdish Mehra. *The Quantum Theory of Planck, Einstein, Bohr and Sommerfeld*. Springer, 2000.

[28] Y. Mairesse and F. Quéré. Frequency-resolved optical gating for complete reconstruction of attosecond bursts. *Phys. Rev. A*, 71(1):011401, Jan 2005.

[29] R. Trebino. *Frequency-Resolved Optical Gating: The Measurement of Ultrashort Laser Pulses*. Kluwer Academic Publishers, Norwell Massachesetts, 2002.

[30] C. Iaconis and I.A. Walmsley. Spectral phase interferometry for direct electric-field reconstruction of ultrashort optical pulses. *Opt. Lett.*, 23(10):792–794, May 1998.

[31] Almantas Galvanauskas Martin E. Fermann and Gregg Sucha. *Ultrafast Lasers Technology and Applications*. Marcel Dekker, Inc., 2003.

[32] Jianping Zhou, Greg Taft, Chung-Po Huang, Margaret M. Murnane, Henry C. Kapteyn, and Ivan P. Christov. Pulse evolution in a broad-bandwidth ti:sapphire laser. *Opt. Lett.*, 19(15):1149–1151, Aug 1994.

[33] Robert Szipöcs, Kárpát Ferencz, Christian Spielmann, and Ferenc Krausz.

Chirped multilayer coatings for broadband dispersion control in femtosecond lasers. *Opt. Lett.*, 19(3):201–203, Feb 1994.

[34] Andreas Stingl, Christian Spielmann, Ferenc Krausz, and Robert Szipöcs. Generation of 11-fs pulses from a ti:sapphire laser without the use of prisms. *Opt. Lett.*, 19(3):204–206, Feb 1994.

[35] J. Hebling, E. J. Mayer, J. Kuhl, and R. Szipöcs. Chirped-mirror dispersion-compensated femtosecond optical parametric oscillator. *Opt. Lett.*, 20(8):919–921, Apr 1995.

[36] U. Morgner, F. X. Kärtner, S. H. Cho, Y. Chen, H. A. Haus, J. G. Fujimoto, E. P. Ippen, V. Scheuer, G. Angelow, and T. Tschudi. Sub-two-cycle pulses from a kerr-lens mode-locked ti:sapphire laser. *Opt. Lett.*, 24(6):411–413, Mar 1999.

[37] D. H. Sutter, G. Steinmeyer, L. Gallmann, N. Matuschek, F. Morier-Genoud, U. Keller, V. Scheuer, G. Angelow, and T. Tschudi. Semiconductor saturable-absorber mirror assisted kerr-lens mode-locked ti:sapphire laser producing pulses in the two-cycle regime. *Opt. Lett.*, 24(9):631–633, May 1999.

[38] W. Sellmeier. *Ann. Phys. Chem.*, 143, Apr 1995.

[39] Rdiger Paschotta. *Encyclopedia of Laser Physics and Technology*. John Wiley and Sons, 2008.

[40] R. L. Fork, O. E. Martinez, and J. P. Gordon. Negative dispersion using pairs of prisms. *Opt. Lett.*, 9(5):150–152, May 1984.

[41] A. Geim. In praise of graphene. *Nature News*, 2010.

[42] J Slonczewski and P Weiss. Band structure of graphite. *Physical Review*, 109(2):272–279, 1958.

[43] Klaus D. Sattler. *Handbook of Nanophysics*. CRC Press, first edition, 2010.

[44] A. C. Ferrari, J. C. Meyer, V. Scardaci, C. Casiraghi, M. Lazzeri, F. Mauri, S. Piscanec, D. Jiang, K. S. Novoselov, S. Roth, and A. . Geim. Raman spectrum of graphene and graphene layers. *Phys. Rev. Lett.*, 97(18):187401, Oct 2006.

[45] L. M. Malard, J. Nilsson, D. C. Elias, J. C. Brant, F. Plentz, E. S. Alves, A. H. Castro Neto, and M. A. Pimenta. Probing the electronic structure of bilayer graphene by raman scattering. *Phys. Rev. B*, 76(20):201401, Nov 2007.

[46] Li-Hong Liu and Mingdi Yan. Simple method for the covalent immobilization of graphene. *Nano Letters*, 9(9):3375–3378, 2009. PMID: 19670850.

[47] K. S. Novoselov, D. Jiang, F. Schedin, T. J. Booth, V. V. Khotkevich, S. V. Morozov, and A. K. Geim. Two-dimensional atomic crystals. *Proceedings of the National Academy of Sciences of the United States of America*, 102(30):10451–10453, 2005.

[48] K.S. Novoselov, P. Blake, and M.I. Katsnelson. Graphene: Electronic properties. In K. H. Jrgen Buschow, Robert W. Cahn, Merton C. Flemings, Bernard Ilschner (print), Edward J. Kramer, Subhash Mahajan, , and Patrick Veyssire (updates), editors, *Encyclopedia of Materials: Science and Technology*, pages 1 – 6. Elsevier, Oxford, 2008.

[49] L. Li, S. Reich, and J. Robertson. Defect energies of graphite: Density-functional calculations. *Phys. Rev. B*, 72(18):184109, Nov 2005.

[50] J.-C. Charlier, P. Eklund, J. Zhu, and A. Ferrari. Electron and phonon properties of graphene: Their relationship with carbon nanotubes. In *Carbon Nanotubes*, volume 111 of *Topics in Applied Physics*, pages 673–709. Springer Berlin / Heidelberg, 2008.

[51] P. R. Wallace. The band theory of graphite. *Phys. Rev.*, 71(9):622–634, May 1947.

[52] A. H. Castro Neto, F. Guinea, N. M. R. Peres, K. S. Novoselov, and A. K. Geim. The electronic properties of graphene. *Rev. Mod. Phys.*, 81(1):109–162, Jan 2009.

[53] Eduardo V. Castro, K. S. Novoselov, S. V. Morozov, N. M. R. Peres, J. M. B. Lopes dos Santos, Johan Nilsson, F. Guinea, A. K. Geim, and A. H. astro Neto. Biased bilayer graphene: Semiconductor with a gap tunable by the electric field effect. *Phys. Rev. Lett.*, 99(21):216802, Nov 2007.

[54] Klaus D. Sattler. *Handbook of Nanophysics: Functional Nanomaterials*. CRC Press, first edition, 2010.

[55] Markus Breusing, Claus Ropers, and Thomas Elsaesser. Ultrafast carrier dynamics in graphite. *Phys. Rev. Lett.*, 102(8):086809, Feb 2009.

[56] Clifford R. Pollock. *E. Wolf, Progress in Optics, Capter 4, Ultrafast Optical Pulses*. Elsevier, College Station, Texas, 51 edition, 2008.

[57] K.J.; Kartner F.X.; Kopf D.; Braun B.; Jung I.D.; Fluck R.; Honninger C.; Matuschek N.; Aus der Au J.; Keller, U.; Weingarten. Semiconductor saturable absorber mirrors (sesam's) for femtosecond to nanosecond pulse generation in solid-state lasers. *IEEE Journal of Selected Topics in Quantum Electronics*, 2(3):435–454, 1996.

[58] I.D. Keller U. Kartner, F.X. Jung. Soliton mode-locking with saturable absorbers. *IEEE Journal of Selected Topics in Quantum Electronics*, 2(3):540 – 556, 1996.

[59] U. Keller. Recent developments in compact ultrafast lasers. *Nature*, 424:831–838, 1996.

[60] D. J. Maas, B. Rudin, A.-R. Bellancourt, D. Iwaniuk, S. V. Marchese, T. Südmeyer, and U. Keller. High precision optical characterization of semiconductor saturable absorber mirrors. *Opt. Express*, 16(10):7571–7579, May 2008.

[61] Hermann A. Haus. Theory of mode locking with a fast saturable absorber. *Journal of Applied Physics*, 46(7):3049–3058, 1975.

[62] A. B. Kuzmenko, E. van Heumen, F. Carbone, and D. van der Marel. Universal optical conductance of graphite. *Phys. Rev. Lett.*, 100(11):117401, Mar 2008.

[63] Q. Bao, H. Zhang, Y. Wang, Z. Ni, Y. Yan, Z. X. Shen, K. P. Loh, and D. Y. Tang. Atomic layer graphene as saturable absorber for ultrafast pulsed lasers. *ArXiv e-prints*, October 2009.

[64] Tawfique Hasan, Zhipei Sun, Fengqiu Wang, Francesco Bonaccorso, Ping Heng Tan, Aleksey G. Rozhin, and Andrea C. Ferrari. Nanotubepolymer composites for ultrafast photonics. *Advanced Materials*, 21(38-39):3874–3899, 2009.

[65] V. Scardaci Z. Sun F. Hennrich I. H. White W. I. Milne1 F. Wang, A.

G. Rozhin and A. C. Ferrari. Wideband-tuneable, nanotube mode-locked, fibre laser. *Nat Nano*, 3:3874–3899, 2009.

[66] Daniel Hemmer Brian Leroy Adam Roberts, Collin Reynolds and Arvinder Sandhu. Response of graphene to intense optical irradiation. In *Bulletin of the American Physical Society, Volume 56, Number 1, Graphene Optical Properies*.

[67] H. Zhang, D. Y. Tang, L. M. Zhao, Q. L. Bao, and K. P. Loh. Large energy mode locking of an erbium-doped fiber laser with atomic layer graphene. *Opt. Express*, 17(20):17630–17635, Sep 2009.

[68] C. Casiraghi, A. Hartschuh, E. Lidorikis, H. Qian, H. Harutyunyan, T. Gokus, K. S. Novoselov, and A. C. Ferrari. Rayleigh imaging of graphene and graphene layers. *Nano Letters*, 7(9):2711–2717, 2007.

APPENDIX A

MATLAB CODE FOR DISPERSION COMPENSATION

```
% MATLAB program to calculate the amount of prism
% separation required to compensate for positive GVD.
clc;
clear all;
c=2.998e8;    % Speed of light(m/s)
tp=90;        % Pulse width in (nm)
w1=1e-3;      % Beam radius of laser as it enters
% the prism sequence (m)
lprism=1e-2;  % How much prism in beam (m)
lglass=0e-2;  % Length of glass in beam
lambdacenter=800e-9; % Center wavelength of laser (m)
bandwidth=13e-9;     % For your fs pulse width
lambda=[.5:.01:2.5];    % Wavelength range in microns
prismseparation=10e-2;  % Separation in (m)
a1=1.69022361;          % Sellmeier Coefficients for the
a2=.288870052;          % prism material
a3=1.7045187;           % SF-14 in this case
b1=.0130512113;
b2=.061369188;
b3=149.517689;
% The following section calculates and plots n as a
% function of wavelength for the prism material
nlambda=sqrt(1+((a1*lambdacenter^2*10^12)/
(lambdacenter^2*10^12-b1))+((a2*lambdacenter^2*10^12)
```

```
/(lambdacenter^2*10^12-b2))+((a3*lambdacenter^2*10^12)
/(lambdacenter^2*10^12-b3)));
n=sqrt(1+((a1*lambda.^2*10^12)./(lambda.^2*10^12-b1))+
((a2*lambda.^2*10^12)./(lambda.^2*10^12-b2))+
((a3*lambda.^2*10^12)./(lambda.^2*10^12-b3)));
plot(lambda,n)

% Now calculate the neg disp in the prisms
%syms A1 A2 A3 B1 B2 B3 lambdareal; % Symbolic integration
%nfirstdirsym=diff(sqrt(1+((A1*lambdareal^2)/
%(lambdareal^2-B1))+((A2*lambdareal^2)/(lambdareal^2-B2))
%+((A3*lambdareal^2)/(lambdareal^2-B3))),'lambdareal')
%nseconddirsym=diff(sqrt(1+((A1*lambdareal^2)/
%(lambdareal^2-B1))+((A2*lambdareal^2)/(lambdareal^2-B2))
%+((A3*lambdareal^2)/(lambdareal^2-B3))),2,'lambdareal')
nfirstdir=-((2*a1*lambdacenter)./(b1 - lambdacenter.^2) +
(2*a2*lambdacenter)./(b2 - lambdacenter.^2) +
(2*a3*lambdacenter)./(b3 - lambdacenter.^2) +
(2*a1*lambdacenter.^3)./(b1 - lambdacenter.^2).^2 +
(2*a2*lambdacenter.^3)./(b2 - lambdacenter.^2).^2 +
(2*a3*lambdacenter.^3)./(b3 - lambdacenter.^2).^2)./
(2*(1 - (a2*lambdacenter.^2)./(b2 - lambdacenter.^2) -
(a3*lambdacenter.^2)./(b3 - lambdacenter.^2) -
(a1*lambdacenter.^2)./(b1 - lambdacenter.^2)).^(1/2));

nseconddir=-((2*a1*lambdacenter)./(b1 - lambdacenter.^2) +
```

```
(2*a2*lambdacenter)./(b2 - lambdacenter.^2) +
(2*a3*lambdacenter)./(b3 - lambdacenter.^2) +
(2*a1*lambdacenter.^3)./(b1 - lambdacenter.^2).^2 +
(2*a2*lambdacenter.^3)./(b2 - lambdacenter.^2).^2 +
(2*a3*lambdacenter.^3)./(b3 - lambdacenter.^2).^2).^2./
(4*(1 - (a2*lambdacenter.^2)./(b2 - lambdacenter.^2) -
(a3*lambdacenter.^2)./(b3 - lambdacenter.^2) -
(a1*lambdacenter.^2)./(b1 - lambdacenter.^2)).^(3/2)) -
((2*a1)./(b1 - lambdacenter.^2) + (2*a2)./
(b2 - lambdacenter.^2) + (2*a3)./(b3 - lambdacenter.^2) +
(10*a1*lambdacenter.^2)./(b1 - lambdacenter.^2).^2 +
(8*a1*lambdacenter.^4)./(b1 - lambdacenter.^2).^3 +
(10*a2*lambdacenter.^2)./(b2 - lambdacenter.^2).^2 +
(8*a2*lambdacenter.^4)./(b2 - lambdacenter.^2).^3 +
(10*a3*lambdacenter.^2)./(b3 - lambdacenter.^2).^2 +
(8*a3*lambdacenter.^4)./(b3 - lambdacenter.^2).^3)./
(2*(1 - (a2*lambdacenter.^2)/(b2 - lambdacenter.^2) -
(a3*lambdacenter.^2)./(b3 - lambdacenter.^2) -
(a1*lambdacenter.^2)./(b1 - lambdacenter.^2)).^(1/2));

GVDneg=lambdacenter^3./(2*pi*c^2*prismseparation)*
(2*((nseconddir+(2*nlambda-1/nlambda^3)*(nfirstdir^2))*
2*w1-2*prismseparation*(nfirstdir^2)));

% Now calculate the positive dispersion from the prisms
GDDprisms=lambdacenter^3/(2*pi*c^2)*nseconddir*lprism;
```

```
% Now calculate the glass positive dispersion
a1p=1.03961212;     % Sellmeier Coefficients for glass
a2p=0.231792344;    % Used to find positive GVD  from glass
a3p=1.01046945;     % BK7 glass in this case
b1p=6.00069867e-3;
b2p=2.00179144e-2;
b3p=1.03560653e2;
%syms a1p a2p a3p b1p b2p b3p lambda; % Symbolic integration

nglass=sqrt(1+((a1p*lambda.^2)./(lambda.^2-b1p))+
((a2p*lambda.^2)./(lambda.^2-b2p))+((a3p*lambda.^2)./
(lambda.^2-b3p)));
%diff(nglass,2,'lambda') % Does the symbolic integration
%nglasssseconddirsym=-((2*a1p*lambda)/(b1p - lambda^2) +
%(2*a2p*lambda)/(b2p- lambda^2) + (2*a3p*lambda)/
%(b3p - lambda^2) + (2*a1p*lambda^3)/(b1p - lambda^2)^2 +
% (2*a2p*lambda^3)/(b2p - lambda^2)^2 + (2*a3p*lambda^3)/
%(b3p - lambda^2)^2)/(2*(1 - (a2p*lambda^2)/(b2p - lambda^2) -
%(a3p*lambda^2)/(b3p - lambda^2) - (a1p*lambda^2)/
%(b1p - lambda^2))^(1/2))

nglasssseconddir=- ((2*a1p)/(b1p - lambdacenter^2) +
(2*a2p)/(b2p - lambdacenter^2) + (2*a3p)/(b3p -
lambdacenter^2) + (10*a1p*lambdacenter^2)/
(b1p - lambdacenter^2)^2 + (8*a1p*lambdacenter^4)/
```

```
(b1p - lambdacenter^2)^3 + (10*a2p*lambdacenter^2)/
(b2p - lambdacenter^2)^2 + (8*a2p*lambdacenter^4)/
(b2p - lambdacenter^2)^3 + (10*a3p*lambdacenter^2)/
(b3p - lambdacenter^2)^2 + (8*a3p*lambdacenter^4)/
(b3p - lambdacenter^2)^3)/(2*(1 - (a2p*lambdacenter^2)/
(b2p - lambdacenter^2) - (a3p*lambdacenter^2)/
(b3p - lambdacenter^2) - (a1p*lambdacenter^2)/
(b1p - lambdacenter^2))^(1/2)) - ((2*a1p*lambdacenter)/
(b1p - lambdacenter^2) + (2*a2p*lambdacenter)/
(b2p - lambdacenter^2) + (2*a3p*lambdacenter)/
(b3p - lambdacenter^2) + (2*a1p*lambdacenter^3)/
(b1p - lambdacenter^2)^2 + (2*a2p*lambdacenter^3)/
(b2p - lambdacenter^2)^2 + (2*a3p*lambdacenter^3)/
(b3p - lambdacenter^2)^2)^2/(4*(1 -
(a2p*lambdacenter^2)/(b2p - lambdacenter^2) -
(a3p*lambdacenter^2)/(b3p - lambdacenter^2) -
(a1p*lambdacenter^2)/(b1p - lambdacenter^2))^(3/2));

GDDglass=lambdacenter^3/(2*pi*c^2)*nglasssecondd ir*lglass;
figure(2);  plot(lambda,nglass)

% Now calculate the effect of the given prism separation
GDDtotal=GDDprisms+GDDglass+GVDneg
% Total GDD for given input
% Adjust the parameters (prism separation...)
% Try to get GDD close to zero
```